Infrared Integrated Optics Pockels Cell High-Voltage Sensors

by

ALI REZA MIRABEDINI

B.Sc., Sharif University of Technology, Tehran, Iran

A THESIS SUBMITTED IN PARTIAL FULFILLMENT OF

THE REQUIREMENTS FOR THE DEGREE OF

MASTER OF APPLIED SCIENCE

in

THE FACULTY OF GRADUATE STUDIES

(Department of Electrical Engineering)

We accept this thesis as conforming
to the required standard

THE UNIVERSITY OF BRITISH COLUMBIA

October 1994

©Ali Reza Mirabedini, 1994

In presenting this thesis in partial fulfilment of the requirements for an advanced degree at the University of British Columbia, I agree that the Library shall make it freely available for reference and study. I further agree that permission for extensive copying of this thesis for scholarly purposes may be granted by the head of my department or by his or her representatives. It is understood that copying or publication of this thesis for financial gain shall not be allowed without my written permission.

(Signature)

Department of Electrical Eng.

The University of British Columbia
Vancouver, Canada

Date Oct. 17, 94

Abstract

This thesis presents a study of the theory of operation, fabrication, and characterization of the infrared Integrated Optics Pockels Cell (IOPC) as a high-voltage sensor. The IOPC is primarily a polarization controlling device which employs the linear electro-optic effect (Pockels effect) of lithium niobate to measure an electric field. A complete IOPC-based system consists of an infrared laser, polarization preserving fibers to deliver and receive polarized light to and from the sensor-head, a sensor-head to be placed in the high-voltage environment, and photodetectors to convert optical signals to electrical ones. The sensor head is basically formed by a z-propagating titanium diffused channel waveguide in a y-cut lithium niobate substrate.

The theory of operation of the IOPC is explained and, as the characteristic equation of the sensor, a normalized optical-intensity-out/electric-field-in transfer function is derived. A mathematical description of the $Ti{:}LiNbO_3$ channel waveguide as a function of the fabrication parameters is provided; then, the associated optical field distribution, using numerical methods, is calculated.

Also, an approximate analytical expression for the intrinsic difference between the propagation constants of the TE- and TM-like modes in a z-propagating $Ti{:}LiNbO_3$ channel waveguide is derived. To justify our method, the derived expression is applied to a simple waveguide case for which analytical solutions are possible.

The experimental part of work consists of the fabrication of the sensor-head and construction of a completely integrated sensor. The fabrication procedures and integration steps taken to realize a fully connectorized IOPC sensor are explained in detail.

In order that IOPC should be considered as a plausible alternative to conventional potential transformers for high-voltage measurements, its performance should be at least as good as the current technology. In this regard, various tests were conducted on the fabricated IOPCs to measure device characteristics and evaluate their performance under various conditions. It is concluded that the sensor is capable of meeting the standards suggested for AC voltage metering and high-voltage switching-impulse monitoring.

Contents

List of Figures

List of Tables

Acknowledgments

My deepest gratitude goes to my parents, brother, and sister for their generous support, encouragement, and understanding.

I would like to thank my supervisor Dr. N. Jaeger for proposing this project and his continuous support throughout the course of this work.

I am also indebted to our research engineers H. Kato, D. Hui, and L. Huang for their valuable help with device fabrication. My appreciation extends to my colleagues in the solid state group, especially F. Rahmatian and B. Tsou for many enlightening discussions. I wish to specially thank my friend, Andrew Hare, for his help in writing this thesis. I am also grateful to all my friends for their invaluable friendship and support through the past years.

Chapter 1: Introduction

The story began in 1893 when F. Pockels introduced the mathematical description of the electro-optic effect and described his experiments to prove the existence of the linear electro-optic effect which was named the "Pockels effect" after him (a translation of the 1906 edition of the German text can be found in reference [1] pp. 121–137). Since then, various devices based on the Pockels effect or other electro- or magneto-optic effects have been suggested, but it was the invention of the laser by T. H. Maiman in 1960 [2] that stimulated the recent surge of study and application of these effects.

Through the 60's and early 70's a variety of novel electric- and magnetic-field sensing devices for high-voltage applications were introduced [3–5]. The rise in size and price of the conventional potential transformers (PT) and current transformers (CT), brought on by higher line voltages, motivated research into optical techniques as cheap and robust alternatives for high-voltage measurements. However, the early devices proposed suffered seriously from the disadvantage of using free-space optical links and consequently from spurious beam interruption.

The development of the first low-loss optical fibers, by Corning Glass Works in 1970 and the maturity of this technology by the end of the decade, made possible the currently available optical fiber sensors. Compared with conventional PT's and CT's, optical fiber sensors possess the following advantageous features: 1. since the measured data are conveyed in the form of optical signals, the measurements are immune to electromagnetic interference, 2. as E-field meters, they can be made to be relatively non-intrusive, 3. also, optical

fiber links provide good isolation between the high-voltage environment and the control room, 4. most optical sensors are passive systems and do not need electronics at the measurement site, 5. optical sensors are much smaller in size and are easy to install, 6. finally, optical sensors promise to be cheaper than instrument transformers in terms of the costs of installation and maintenance. In this regard, various materials were investigated for their electro- and magneto-optic properties. Among them are $LiNbO_3$, $LiTaO_3$, KDP (KH_2PO_4), and BGO ($Bi_4Ge_3O_{12}$) for voltage sensors employing the linear electro-optic effect (Pockels effect) [6–9] and BSO ($Bi_{12}SiO_{20}$), α-quartz, and borosilicate crown glass for current sensors employing the magneto-optic effect (Faraday effect) [10,11,9].

The reports in the late 80's and 90's mainly focus on the accuracy and stability of the optical sensors and their capability to meet industrial standards. Kanoi et al. [9] have reported a BGO Pockels cell type voltage sensor having a ratio error within ±0.4% and a temperature stability of ±1.0% over the temperature range of –20 to 60 °C. Sawa et al. [6] have announced that their $LiNbO_3$ Pockels sensor using a capacitive divider is capable of meeting Japan Electrotechnical Commission standard JEC1201 for electric-power instrument transformers. The report by Kobayashi et al. [12] on a BGO Pockels sensor including the results of 20 months of field testing confirms that the optical sensor being tested was not only able to meet the JEC1201 standard, but also showed a very stable and reliable performance throughout the test period.

In contrast with all the devices mentioned above which are developed around the electro-optic effects in bulk crystals, in the integrated version of the Pockels cell introduced in 1991 by N. Jaeger [13], the sensor-head is formed by a z-propagating optical channel waveguide fabricated in a y-cut $LiNbO_3$ substrate. Conventional Pockels sensors incorporating bulk

crystals can easily be damaged because of loss of alignment (for example, due to mechanical vibrations); however, in the introduced integrated optics Pockels cell (IOPC), since the fibers are bonded directly to the substrate, this problem is avoided. Comparatively, the integrated version has a simpler structure; the IOPC employs its intrinsic phase difference between the propagating modes to set the polarization of the output to a proper state and therefore does not need the quarter-wave plate usually used in the conventional cells. In addition, the IOPC does not need any alignment in the high-voltage environment and is easy to install.

Chapter 2 includes a description of the IOPC and its theory of operation, the derivation of the characteristic equations, and an analytical representation and some numerical modeling of $Ti{:}LiNbO_3$ channel waveguides. In chapter 3 the practical concerns regarding the fabrication process of the sensor-head and constructing a completely integrated system are discussed. Numerous tests were conducted to measure device characteristics and evaluate IOPC performance under various conditions; the results are presented in chapter 4. In chapter 5, one of the major characteristics of the IOPC, namely, the intrinsic phase, is analyzed and an approximate analytical expression for it is derived. Finally, chapter 6 provides a summary of the work and some suggestions for further improvements.

Chapter 2: Theory

§ 2.1 Introduction

In this chapter the operating principles, simulation methods and design considerations of the Integrated Optics Pockels Cell (IOPC) as a high-voltage sensor are developed and explained. A complete IOPC-based system, Fig. 2.1, consists of a diode laser, as the optical source, polarization maintaining optical fibres to deliver and receive polarized light to and from the sensor-head, a sensor-head to be placed in the high-voltage environment, and photodetectors to convert the optical signals to electrical ones. The sensor-head is basically a titanium-diffused channel waveguide in a lithium niobate substrate that measures the electric field in which it is immersed. The sensor-head is a passive device and may be set to a proper working point by changing its length. Therefore, no electronic bias control circuitry is needed in the high-voltage environment.

The basic concepts and operating principles of the IOPC are described in the next section, 2.2. Section 2.3 covers a number of 2–D mode solvers to calculate the optical field distributions in $Ti{:}LiNbO_3$ channel waveguides.

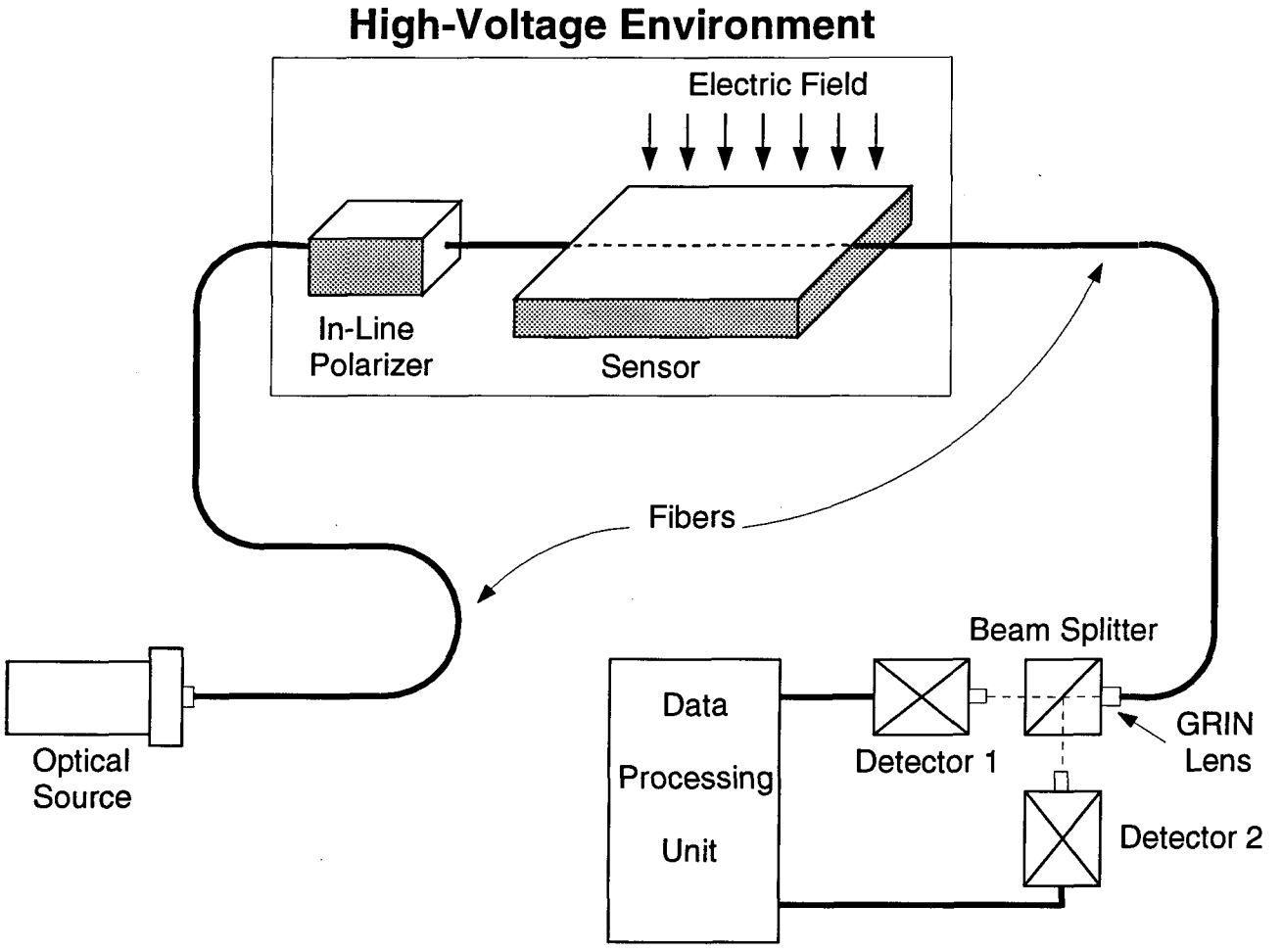

Figure 2.1. A typical configuration of an IOPC as a high-voltage sensor.

§ 2.2 Device Description

A Pockels cell voltage sensor is primarily a polarization controller which exploits the linear electro-optic effect (Pockels effect) of some material to measure an electric field. The theory of operation of the IOPC is similar to that of conventional Pockels cell amplitude modulators using bulk electro-optic crystals, which can be found in the literature [14,1,15]. In brief: application of an electric field along a specific direction to an electro-optic medium

changes the birefringence in the plane normal to the direction of light propagation; the electrically-induced change in the birefringence is used to produce a phase difference between the two orthogonal eigenmodes propagating in the medium which, in turn, leads to a change in the polarization state of the output; the passage of the output through an analyzer converts the change in the polarization state to a corresponding variation in the signal amplitude and thus, results in an amplitude modulation. The amplitude-modulated light can be transmitted through the optical fibre without losing its information content and finally, the information, namely, the value of the applied electric field, can be extracted by using an optoelectronic conversion unit.

In the integrated optics version of the Pockels cell the sensor-head is formed by a z-propagating optical channel waveguide, fabricated in a y-cut lithium niobate substrate, see Fig. 2.2. In this text, the spacial coordinate axes, i.e., x, y, and z, are named according to the crystallographic axes of the lithium niobate crystal. The optical channel waveguide is made by diffusing a titanium strip, parallel to the z-axis, into the lithium niobate substrate. The indiffusion of titanium ions produces a small incremental increase in the refractive index of lithium niobate and, hence, forms the graded refractive index profile required for light confinement. By adjusting the fabrication parameters, sizes of the waveguide are achieved which support the propagation of only the fundamental orthogonal eigenmodes, namely, fundamental TE- and TM- like modes. Here, by TE- and TM-like modes we mean the modes with electric fields substantially polarized parallel to the x and y axes, respectively.

Lithium niobate belongs to the point group 3m and has the following electro-optic

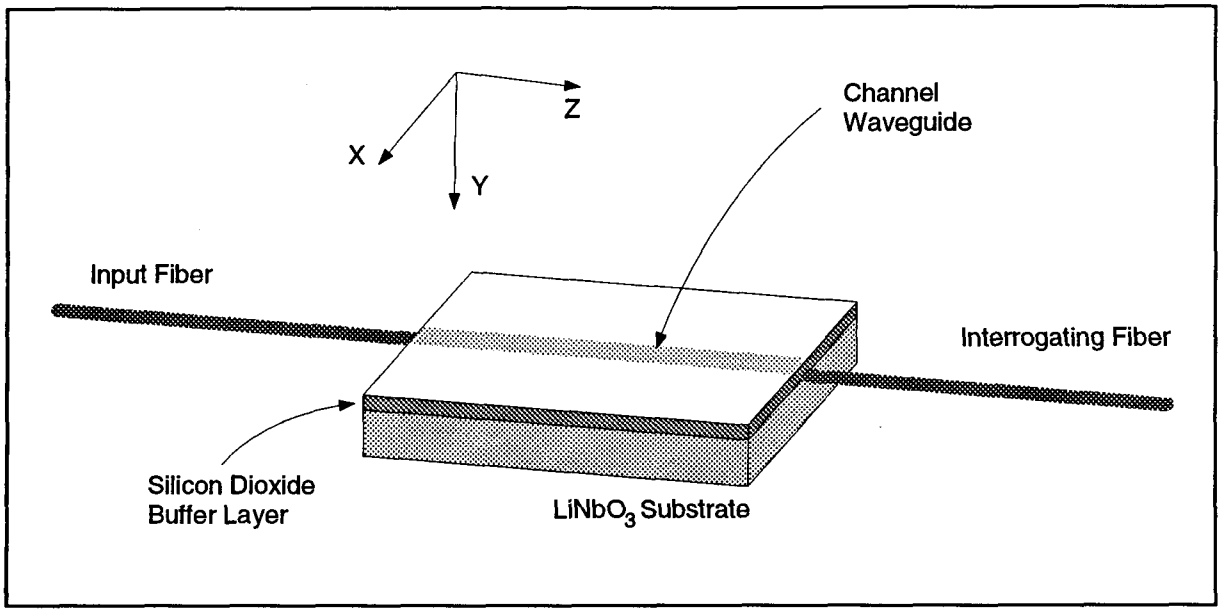

Figure 2.2. An isometric illustration of an IOPC sensor-head.

coefficient matrix [16],

$$\begin{bmatrix} 0 & r_{12} & r_{13} \\ 0 & r_{22} & r_{23} \\ 0 & 0 & r_{33} \\ 0 & r_{42} & 0 \\ r_{51} & 0 & 0 \\ r_{61} & 0 & 0 \end{bmatrix}, \tag{2.1}$$

where $r_{13}=r_{23}$, $r_{42}=r_{51}$, and $r_{22}=-r_{12}=-r_{61}$. In the absence of an external electric field, the bulk refractive indices in the x and y directions, n_x and n_y respectively, are equal to the ordinary refractive index, n_o, while the refractive index in the z direction, n_z, is the extraordinary refractive index, n_e. Application of an electric field parallel to the y axis, E_y, changes the refractive indices n_x and n_y through the electro-optic coefficients r_{12} and r_{22} ($= -r_{12}$), respectively. The amount of change is given by

$$\Delta n_x = \frac{n_o^3 r_{22} E_y}{2} \quad \text{and} \quad \Delta n_y = -\frac{n_o^3 r_{22} E_y}{2}. \tag{2.2.a, b}$$

Therefore, the electrically induced birefringence "seen" by light, propagating along the z axis, is

$$n_x - n_y = n_o^3 r_{22} E_y. \tag{2.3}$$

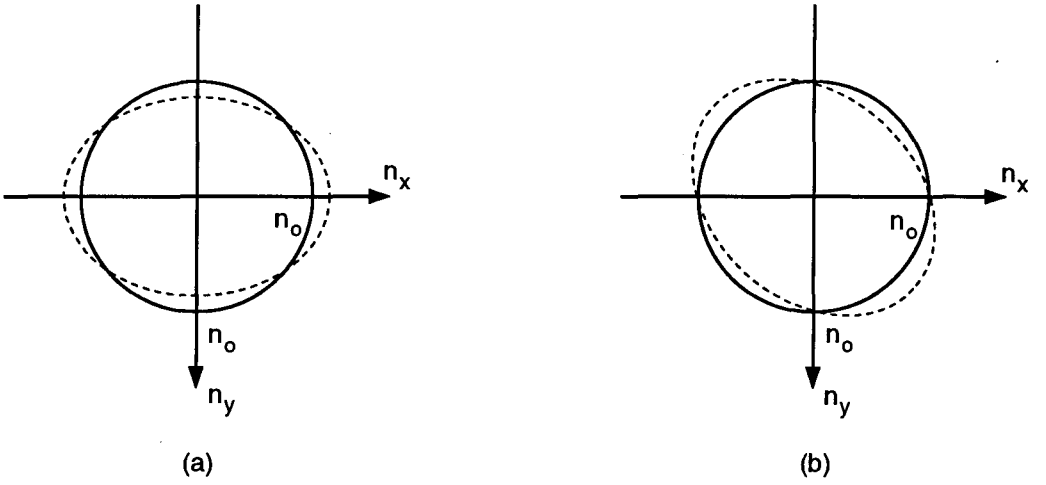

Figure 2.3. The intersection of the *x*-*y* plane with the lithium niobate index ellipsoid, in the absence of an external electric field (solid lines) and in the presence of an external electric field (doted lines) a) parallel to the *y* axis, b) parallel to the *x* axis.

Fig. 2.3 shows the intersection of the *x*-*y* plane with the index ellipsoid in the presence of an electric field applied parallel to the *y* axis, Fig. 2.3(a), and *x* axis ($\Delta n_{xy} = -\frac{n_o^3 r_{61} E_x}{2}$), Fig. 2.3 (b).

Since the performance of the IOPC depends on the polarization state of the input light, a polarization maintaining fibre was used to launch the light into the optical channel waveguide at a certain polarization. A semiconductor laser (LAS–300–1300–6, LaserMax Inc., NY) provides the polarized light with a polarization ratio of 200:1 at a free-space wavelength of λ_o = 1.3 μm. The light from the laser is coupled to one of the two principal axes of a PM (polarization maintaining) fibre. The polarized light, before coupling to the waveguide, passes through an in-line polarizer with an isolation factor of –25.4 dB (Model: 917P, Canadian Instrumentation and Research Ltd., Ont. Canada), to sufficiently increase the polarization ratio of the input light and suppress the effect of intermodal coupling in the PM fibre. The principal axes of the PM fibre are oriented at 45° with respect to the *x* and *y* axes, see Fig. 2.4. Therefore, under ideal circumstances, the total optical field coupled to the waveguide

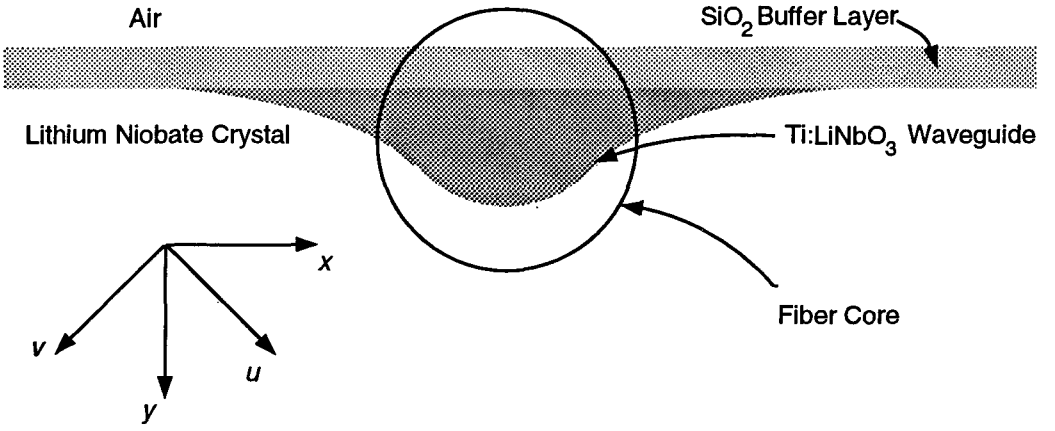

Figure 2.4. Orientation of the optical fibre axes with respect to the crystallographic axes of lithium niobate.

may be decomposed to two equal components along the x and y axes. These components are the fundamental TE- and TM-like modes of the *Ti:LiNbO3* channel waveguides. Hence, at $z = 0$ we have

$$E_x = \frac{E_i}{\sqrt{2}} \sin(\omega_o t) \tag{2.4a}$$

$$E_y = \frac{E_i}{\sqrt{2}} \sin(\omega_o t) \tag{2.4b}$$

where E_i and ω_o are, respectively, amplitude and angular frequency of the input optical field.

In a bulk crystal, since $n_x = n_y = n_o$, the two eigenmodes propagate with the same phase velocities. Hence, the polarization state of the output beam is the same as that of the input beam. But in a z-propagating titanium diffused channel waveguide, primarily due to the different boundary conditions for the TE- and TM-like modes at the substrate-superstrate interface, the two eigenmodes travel with slightly different phase velocities. In chapter 5 an

analytical method has been developed to estimate the intrinsic (here we use "intrinsic" as opposed to "voltage-induced") difference between the propagation constants of the TE- and TM-like modes, $\Delta\beta = \beta_{\mathrm{TE}} - \beta_{\mathrm{TM}}$. Because of the difference between the phase velocities of the eigenmodes, the passage of light through the waveguide produces an intrinsic phase difference between the two modes, ϕ_i, which is proportional to the length of device, L; $\phi_i = \Delta\beta \times L$. Therefore, it is possible to set the polarization of the output beam to a desirable state by adjusting the length of the device. In this text, ϕ_i is also called as the "bias" or "working point" of the device.

In the presence of an electric field applied parallel to the y-axis, the electrically induced birefringence, equ. 2.3, produces another contribution to the phase difference between the two modes , ϕ_e, given by

$$\phi_e = k_o\left(n_o^3 r_{22} E_y\right) L, \tag{2.5}$$

where $k_o = 2\pi/\lambda_o$. ϕ_e may be rewritten in the following form,

$$\phi_e = \pi \frac{E_y}{E_\pi}, \tag{2.6}$$

where $E_\pi = \frac{\lambda_o}{2n_o^3 r_{22} L}$ which is defined as the electric field needed to produce a π radians phase difference between the two eigenmodes and is called "the half-wave electric field".

The total phase difference between the two modes at the output, $z = L$, is

$$\phi_t = \phi_e + \phi_i. \tag{2.7}$$

Assuming the phase of the TM-like mode is zero at $z = L$ when $t = 0$, the electric fields of the two eigenmodes at the output are

$$\begin{aligned} E_x &= \frac{E_o'}{\sqrt{2}} \sin\left(\omega_o t + \phi_t\right), \\ E_y &= \frac{E_o''}{\sqrt{2}} \sin\left(\omega_o t\right). \end{aligned} \tag{2.8}$$

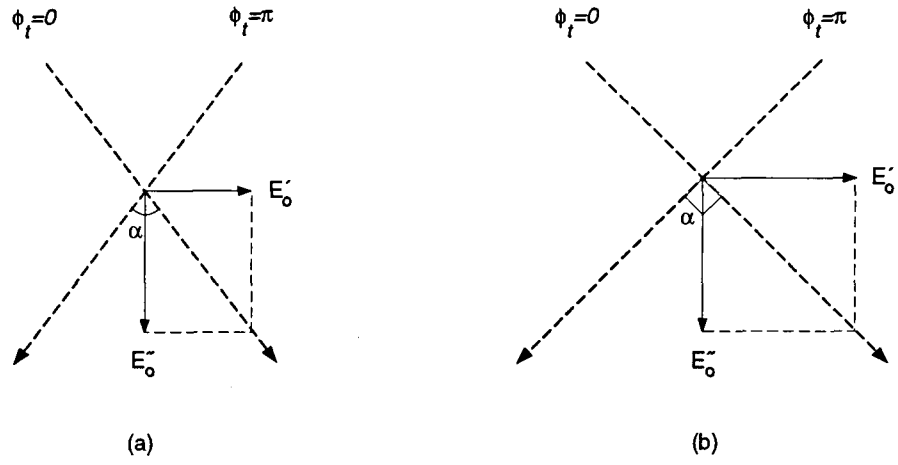

Figure 2.5. The axes of linear polarization $\phi_t = 0$ and π, a) when $E'_o \neq E''_o$, so $\alpha \neq 90°$, b) when $E'_o = E''_o$, so $\alpha = 90°$.

Generally speaking E'_o and E''_o are not equal. This is because the waveguide structure exhibits different absorptions for the two modes. Since the best device performance may be obtained when the two axes of linear polarization of the output beam (when $\phi_t = 0$ or π) are perpendicular to each other, the power of the TE- and TM-like modes should be equal, see Fig. 2.5. This can be achieved by rotating the input fibre so as to couple more power to the eigenmode with greater absorption loss, so that both modes appear at the output with equal powers, i.e., $E'_o = E''_o = E_o$.

Now if we align the principal axes of the interrogating fibre at 45° to the x and y axes, the electric field of the light coupled to each axis of the interrogating fibre is

$$E_u = \left(E_o \cos\frac{\phi_t}{2}\right) \sin\left(\omega_o t + \frac{\phi_t}{2}\right) \tag{2.9}$$

where the axis u is parallel to the axis of linear polarization $\phi_t = 0$, and

$$E_v = \left(E_o \sin\frac{\phi_t}{2}\right) \cos\left(\omega_o t + \frac{\phi_t}{2} + \pi\right) \tag{2.10}$$

where the axis v is parallel to the axis of linear polarization $\phi_t = \pi$.

The optical fields coupled to the principal axes of the output fibre are separated when the light passes through a polarizing beam splitter. Then, the optical power of each component is measured by an optoelectronic conversion unit. The measured optical power for the u and v axes are

$$P_{u,v} = P_o \frac{1 \pm \cos \phi_t}{2} = P_o \frac{1 \pm \cos\left(\pi \frac{E_y}{E_\pi} + \phi_i\right)}{2}, \tag{2.11}$$

where P_o is the total output power, and, $+$ and $-$ signs are, respectively, corresponding to the readings parallel to u and v axes. Since the total output power may change with time (because of gradual variations in the laser output power or temporary alignment disorders caused by mechanical vibrations), it is important that the measurement procedure have no dependence on P_o. This can be achieved by instantaneously dividing the value measured by each detector by the sum of the readings of both detectors, i.e.,

$$S_{u,v} = \frac{P_{u,v}}{P_u + P_v} = \frac{1 \pm \cos\left(\pi \frac{E_y}{E_\pi} + \phi_i\right)}{2}, \tag{2.12}$$

where $S_{u,v}$ is the normalized optical power, and again, the $+$ and $-$ signs correspond to the readings parallel to u and v axes, respectively. Ideally, $S_{u,v}$ can take on values between 0 and 1; when all the optical power is coupled to the u axis, i.e., $\phi_t = 0$, $S_u = 1$ and $S_v = 0$, and when all the optical power is coupled to the v axis, i.e., $\phi_t = \pi$, $S_u = 0$ and $S_v = 1$. Practically, because of alignment imperfections, equ. 2.12 finds the following form,

$$S_{u,v} = \frac{P_{u,v}}{P_u + P_v} = \frac{1 \pm \alpha \cos\left(\pi \frac{E_y}{E_\pi} + \phi_i\right)}{2}, \tag{2.13}$$

where α has a value close to one.

§ 2.3 Ti:$LiNbO_3$ Channel Waveguide Modelling

• 2.3.1 General Considerations

The numerical methods introduced in this section provide us with information about three important features of optical field distributions in waveguide structures; firstly, the number of modes that will propagate in the waveguide, secondly, the optical field profile of each mode, including optical mode sizes, and thirdly, the propagation constants of the modes, i.e., the effective refractive indices associated with the modes. The above knowledge about the optical field distribution in a particular waveguide structure helps the designer to properly adjust the fabrication parameters to gain desirable results. For instance, fabrication of a single-mode *Ti:LiNbO₃* channel waveguide which supports the propagation of only the fundamental TE- and TM-like modes (and not the higher order ones) is essential to the performance of the IOPC (see section 4.3); also for reducing the waveguide-to-fibre coupling loss, due to the optical profile mismatch, it is necessary to have a knowledge of the profile and sizes of the propagating mode [17]; furthermore, in waveguide structures, such as directional couplers, the main characteristic of the device, namely, the coupling length, is a function of the propagation constants of the even and odd modes [18].

For modelling purposes, the first step is to describe mathematically the refractive index profile induced in the lithium niobate substrate, due to the indiffusion of titanium ions, as a function of the fabrication parameters.

The *Ti:LiNbO₃* channel waveguide is constructed by diffusion of a long, narrow strip of titanium, deposited parallel to the z axis, into a y-cut lithium niobate substrate. The distribution of diffused titanium ions inside the lithium niobate is a function of the nature

of titanium indiffusion mechanism and diffusion conditions such as diffusion time and temperature. Assuming that the diffusion time is long enough to exhaust the source material (a finite source case) the two dimensional anisotropic diffusion from a line source forms a Gaussian type concentration profile both in the depth and width (surface) directions [19]. Since a strip source may be considered as a number of adjacent line sources, and thanks to the separable nature of the Gaussian profile with respect to the x and y, the concentration of titanium ions, $C(x,y)$, diffused from the strip source, shown in Fig. 2.6, is

$$C(x,y) = Ce^{-\left(\frac{y}{d_y}\right)^2} \int_{-w/2}^{w/2} e^{-\left(\frac{x-x'}{d_x}\right)^2} dx', \tag{2.14}$$

or [20,21]

$$C(x,y) = \frac{\tau}{2\sqrt{\pi D_y t}} e^{-\left(\frac{y}{2\sqrt{D_y t}}\right)^2} \left[erf\left(\frac{w/2+x}{2\sqrt{D_x t}}\right) + erf\left(\frac{w/2-x}{2\sqrt{D_x t}}\right)\right], \tag{2.15}$$

where

$$D_x = D_{ox} exp\left(-\frac{Q}{k_B T}\right) \text{ and } D_y = D_{oy} exp\left(-\frac{Q}{k_B T}\right),$$

τ and w are, respectively, the prediffusion titanium strip thickness and width, t is the diffusion time, D_{ox} and D_{oy} are, respectively, the diffusion constants in the x and y directions, Q is the activation energy, k_B is Boltzmann's constant, and T is the diffusion temperature in Kelvin. In equ. 2.15, $C(x,y)$ is the diffused titanium concentration as a fraction of the titanium metal density, in other words,

$$\int_0^{+\infty} \int_{-\infty}^{+\infty} C(x,y)\, dx\, dy = \tau w. \tag{2.16}$$

For the simulation purposes we have used the following values for the fabrication parameters: $D_x = D_y = 1.1\times10^{-4}$ μm^2/sec at T = 1050°C for congruent $LiNbO_3$ [22], t = 6.5 hours, and τ = 700 nm. Since the titanium strip is deposited by metal evaporation, the density of the

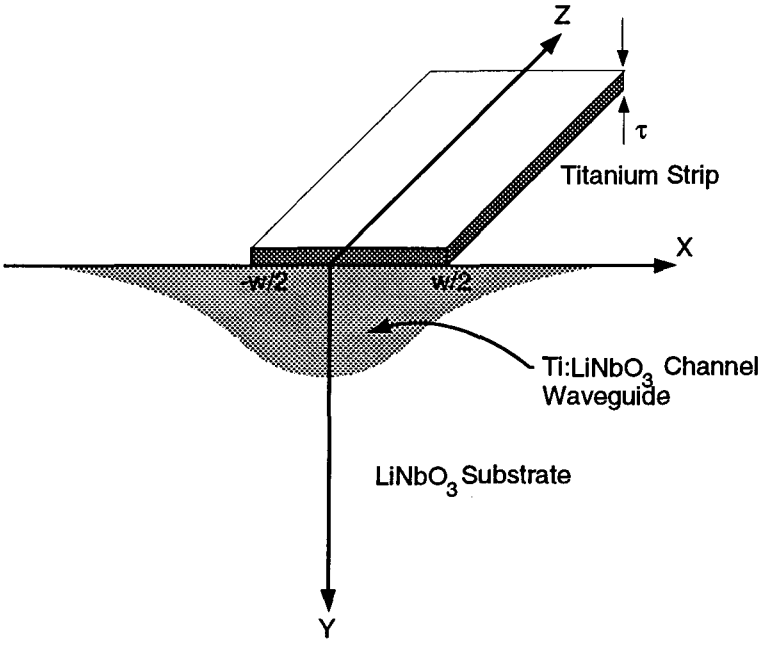

Figure 2.6. A typical *Ti:LiNbO$_3$* channel waveguide.

deposited layer is less than the density of titanium metal [20]; for this reason a correction factor of 0.7, obtained from in-house experimental work, is applied to the initial value of τ.

While the extraordinary refractive index change, Δn_e, is linearly related to the titanium concentration, i.e., $\Delta n_e(x,y) = \alpha_e C(x,y)$, this is not the case for the titanium induced ordinary index change, Δn_o [23–25]. In fact a fourth order polynomial fit to the data reported by Minakata et al. [23] is used as the calibration curve between the titanium concentration, $C(x,y)$, and Δn_o [26],

$$\Delta n_o(x,y) = \sum_i \alpha_i C^i(x,y) \qquad i = 1,2,...,4 \tag{2.17}$$

where α_0 = -1.65×10^{-5}, α_1 = 1.05, α_2 = -81.6, α_3 = 3.88×10^3, and α_4 = -6.64×10^4.

It is notable, since there is a wide variation in the published data for the diffusion coefficients, D_x and D_y, and incremental refractive indices, Δn_e and Δn_o, [27], the above choice of references is based on the work done in chapter 5 to match the computed values for $\Delta\beta = \beta_{TE}-\beta_{TM}$ to the measured ones.

The next step in our modelling is to find the proper wave equations governing the optical field distribution in the waveguide structure. Assuming a length invariant channel waveguide ($\frac{\partial n}{\partial z} = 0$) and a propagation function like $e^{-j\beta z}$ in the axial direction, the vector wave equations reduce to [28]

$$\nabla_t^2 \overline{E}_t + (k_o^2 n^2(x,y) - \beta^2)\overline{E}_t = -\nabla_t(\nabla_t ln(n^2(x,y)).\overline{E}_t), \tag{2.18}$$

and

$$\nabla_t^2 \overline{H}_t + (k_o^2 n^2(x,y) - \beta^2)\overline{H}_t = (\nabla_t \times \overline{H}_t) \times \nabla_t ln(n^2(x,y)), \tag{2.19}$$

where k_o is the free space wave number, *n(x,y)* is the refractive index distribution, $\overline{E}_t$ and $\overline{H}_t$ are, respectively, the transverse components of the electric and magnetic fields, ∇_t and ∇_t^2 are, respectively, the gradient and Laplacian operators in the transverse plane, and β is the propagation constant in the z direction. Considering the waveguide structure shown in Fig. 2.6, for the TE-like mode (i.e., when the electric field is primarily polarized parallel to the x axis) the vector wave equ. 2.18 becomes

$$\frac{\partial^2 E_x}{\partial x^2} + \frac{\partial^2 E_x}{\partial y^2} + \left\{ \frac{\partial^2 ln\, n^2}{\partial x^2} + \frac{\partial ln E_x}{\partial x}\frac{\partial ln\, n^2}{\partial x} + k_o^2 n^2 - \beta_{TE}^2 \right\} E_x = 0, \tag{2.20}$$

and for the TM-like mode equ. 2.18 becomes

$$\frac{\partial^2 E_y}{\partial x^2} + \frac{\partial^2 E_y}{\partial y^2} + \left\{ \frac{\partial^2 ln\, n^2}{\partial y} + \frac{\partial ln E_y}{\partial y}\frac{\partial ln\, n^2}{\partial y} + k_o^2 n^2 - \beta_{TM}^2 \right\} E_y = 0, \tag{2.21}$$

where n is $n_o(x,y) = n_o + \Delta n_o(x,y)$ and the subscript on E indicates the polarization direction of the main component of the electric field.

In numerical modelling of weakly guiding structures with slowly varying inhomogeneity, like typical *Ti:LiNbO3* channel waveguides, it is a common approximation to ignore the terms containing the derivatives of the refractive index profile [29,30] which reduces equ. 2.18

to the scalar wave equation,

$$\nabla_t^2 \overline{E}_t + \left(k_o^2 n^2(x,y) - \beta^2\right)\overline{E}_t = 0. \tag{2.22}$$

In appendix A, it is shown that contributions of the extra terms in equations 2.20 and 2.21 to the variational expressions ofβ_{TE}^2 and β_{TM}^2 are on the order of 10^{-5} rad$^2/\mu$m^2 and hence are negligible.

In the next two subsections we use the Effective Index Method (EIM) and the Finite Difference Method (FDM) to solve the equ. 2.22. Since, in that equation, both the electric field distribution, *E(x,y)*, and the propagation constant, β, are unknown, the above methods become an eigenvalue problem whose eigenfunctions and eigenvalues are the possible solutions for *E(x,y)* and β, respectively. Reference [30] was used as a major source for the general descriptions of the above methods.

• 2.3.2 Effective Index Method (EIM)

The effective index method is based on the idea that the light distribution in the transverse plane is almost a separable function of x and y. Physically, the above assumption means that we can consider our channel waveguide as a combination of numerous adjacent slab waveguides, Fig. 2.7. This approximation by replacing a 3–d structure by a number of 2–d ones brings a great simplicity to our problem. This concept, although based on an approximation, is applicable to many practical configurations such as planar and rectangular [31–33], circular [34,35], and rib waveguides [36,37].

Fig. 2.7 shows a channel waveguide with an arbitrary refractive index profile, *n(x,y)*, which is invariant in the z-direction. Regarding our discussion in section 2.2, an optical mode propagating along the z direction is given by,

$$\Psi(x,y,z) = \Phi(x,y)exp(-j\beta z) \tag{2.23}$$

where β is propagation constant and Ψ is electric field. Using scalar wave approximation, $\Phi(x,y)$ should satisfy the following equation,

$$\nabla_{xy}^2\Phi + \left[k_o^2 n^2(x,y) - \beta^2\right]\Phi = 0, \tag{2.24}$$

where k_o is the wave number, $k_o = 2\pi/\lambda_o$, and λ_o is the free space wave length. We assume that we can write Φ as a product of two functions,

$$\Phi(x,y) = F(x,y)G(x), \tag{2.25}$$

where $F(x,y)$ is a slowly varying function with x,

$$\frac{\partial F(x,y)}{\partial x} \approx 0. \tag{2.26}$$

substituting equ. 2.25 into 2.24, one gets,

$$\begin{aligned} F(x,y)\frac{d^2G}{dx^2} + 2\frac{\partial F(x,y)}{\partial x}\frac{dG(x)}{dx} + \\ + G(x)\left[\frac{\partial^2}{\partial x^2}F(x,y) + \frac{\partial^2}{\partial y^2}F(x,y)\right] + \left(n^2k_o^2 - \beta^2\right)F(x,y)G(x) = 0. \end{aligned} \tag{2.27}$$

Considering the approximation expressed by equ. 2.26, we obtain,

$$\frac{1}{G}\frac{d^2G}{dx^2} + \frac{1}{F}\frac{\partial^2 F}{\partial y^2} + \left(n^2k_o^2 - \beta^2\right) = 0. \tag{2.28}$$

If we rewrite equ. 2.28 in the following form,

$$\frac{1}{G}\frac{d^2G}{dx^2} - \beta^2 = -\frac{1}{F}\frac{\partial^2 F}{\partial y^2} - n^2k_o^2, \tag{2.29}$$

the right hand side of equ. 2.29 is only a function of x, which means that we can define an arbitrary function of x, like $k_o^2 n_{eff}^2(x)$, to split the equation as follows,

$$\frac{1}{F}\frac{\partial^2 F}{\partial y^2} + n^2k_o^2 = k_o^2 n_{eff}^2(x), \tag{2.30}$$

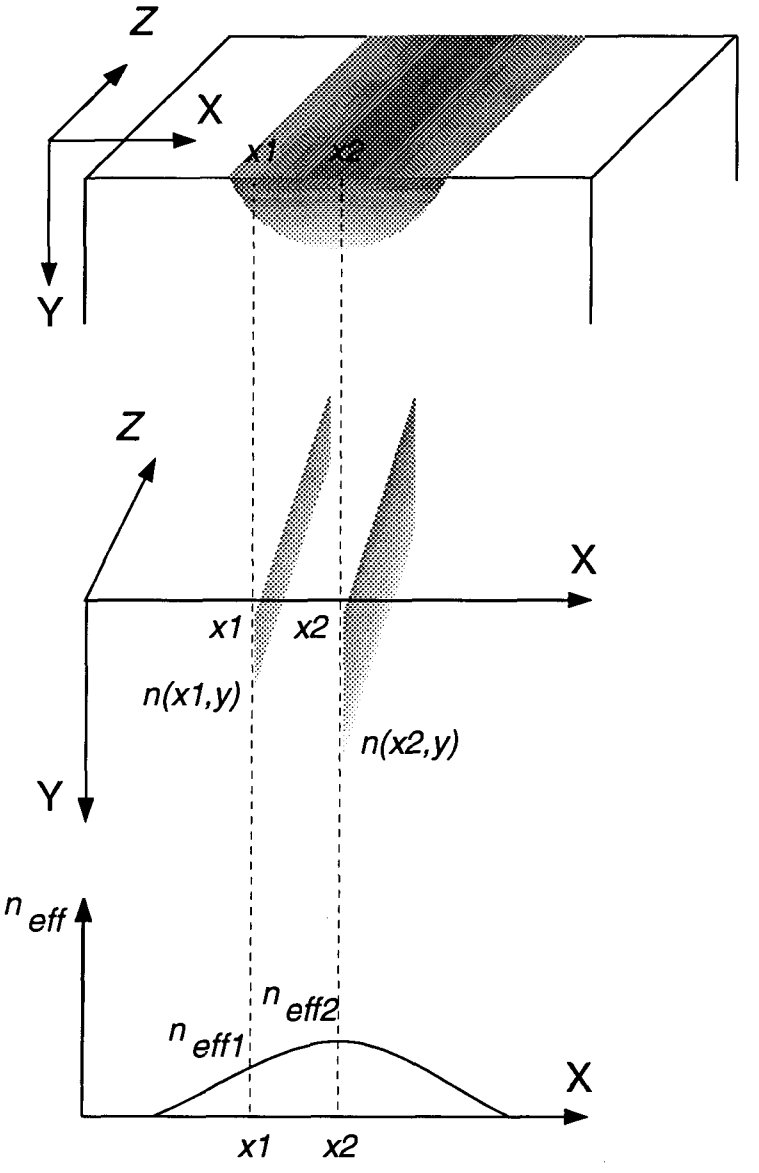

Figure 2.7. A simple illustration of Effective Index Method.

and

$$\frac{1}{G}\frac{d^2G}{dx^2} - \beta^2 = -k_o^2 n_{eff}^2(x). \tag{2.31}$$

Through solving equ. 2.30, we can obtain both the field, *F(x,y)*, and the effective refractive index profile, $n_{eff}(x)$. Substituting the calculated index profile in equ. 2.31 provides us with the field distribution *G(x)* and the propagation constant of the mode (associated with Φ), i.e., β. According to equ. 2.25, the product of *G(x)* and *F(x,y)* yields

$\Phi(x,y)$, the modal field of the three-dimensional waveguide of Fig. 2.7

As a numerical approach to find $n_{eff}(x)$ from equ. 2.30, we consider x as a parameter (for example $x = x_k$), therefore equ. 2.30 takes the following form,

$$\frac{\partial^2 F_k(y)}{\partial y^2} + k^2\left(n_k^2(y) - n_{eff(k)}^2\right)F_k(y) = 0 \tag{2.32}$$

where the index k comes from point $x = x_k$. F_k and $n_{eff(k)}$ are respectively the electric field profile and effective index of a mode in the k-th slab waveguide, $n_k(y)$. Through calculating F_k and $n_{eff(k)}$ for all the slabs, one gets $F(x,y)$ and $n_{eff}(x)$.Fig. 2.7 shows this procedure for k = 1 and 2.

Various numerical methods may be used to solve equ. 2.32, which is the 1–D form of wave equation, such as 1–d finite difference method or WKB method [38]. Here, we use MATLAB as the programming language to implement the finite difference method.

The first step is to write equ. 2.32 in the form of a difference equation. We assume that the function $F_k(y)$ is discretised in N_y points along the y axis, $y = y_i$, $i = 1...N_y$. We also assume that $F_k(y)$ is zero on the boundary points, i.e., $F_k(y_0) = F_k\left(y_{N_y+1}\right) = 0$. In this case the solution of Equation 2.32 leads to an eigenvalue problem as follows,

$$\{[A] - \beta^2[U]\}[X] = 0 \tag{2.33}$$

where $[X] = [F_k(y_i)]$, $i = 1...N_y$, $[U]$ is a unit matrix and $[A]$ is a real $N_y \times N_y$ matrix.

Matrix [A] has the following form,

$$\begin{bmatrix} -2c+d_1 & c & 0 & & \cdots & 0 & 0 \\ c & -2c+d_2 & c & 0 & & & 0 \\ 0 & c & -2c+d_3 & c & \ddots & & \vdots \\ & 0 & \ddots & \ddots & \ddots & 0 & \\ \vdots & & \ddots & c & -2c+d_{N_y-2} & c & 0 \\ 0 & & & 0 & c & -2c+d_{N_y-1} & c \\ 0 & 0 & \cdots & & 0 & c & -2c+d_{N_y} \end{bmatrix} \tag{2.34}$$

where $d_i = n_k^2(y_i)$ and $c = 1/\Delta^2 k_o^2, \quad \Delta = y_{i+1} - y_i$.

The effective index method was applied to the Gaussian refractive index profile shown in Fig. 2.8. For a 300×300 grid and Δ = 0.1μm, figures 2.8 and 2.9 show the calculated effective index profile in the x direction and optical field distribution in the *x-y* plane, respectively.

The errors of the effective index method includes both that of the assumption 2.26 and the finite difference approach used to solve 2.32. Compared with the finite-difference method explained in the next section, EIM needs a higher grid resolution and, in general, the propagation constants obtained through this method are overestimated [30]. Specially, for weakly guiding structures, like typical *Ti:LiNbO$_3$* channel waveguides for which the maximum refractive index change is less than 0.01, EIM showed a poor performance compared to the finite difference method, in terms of amount of calculations and computation time. Also, the calculated optical field distribution does not match the expected one and the tails appeared in Fig. 2.9 arise from the errors of EIM. Because of these drawbacks, we mainly relied on the finite difference method, explained in the next section, to calculate the propagation constant and modal sizes of the optical field distribution in *Ti:LiNbO$_3$* channel waveguides.

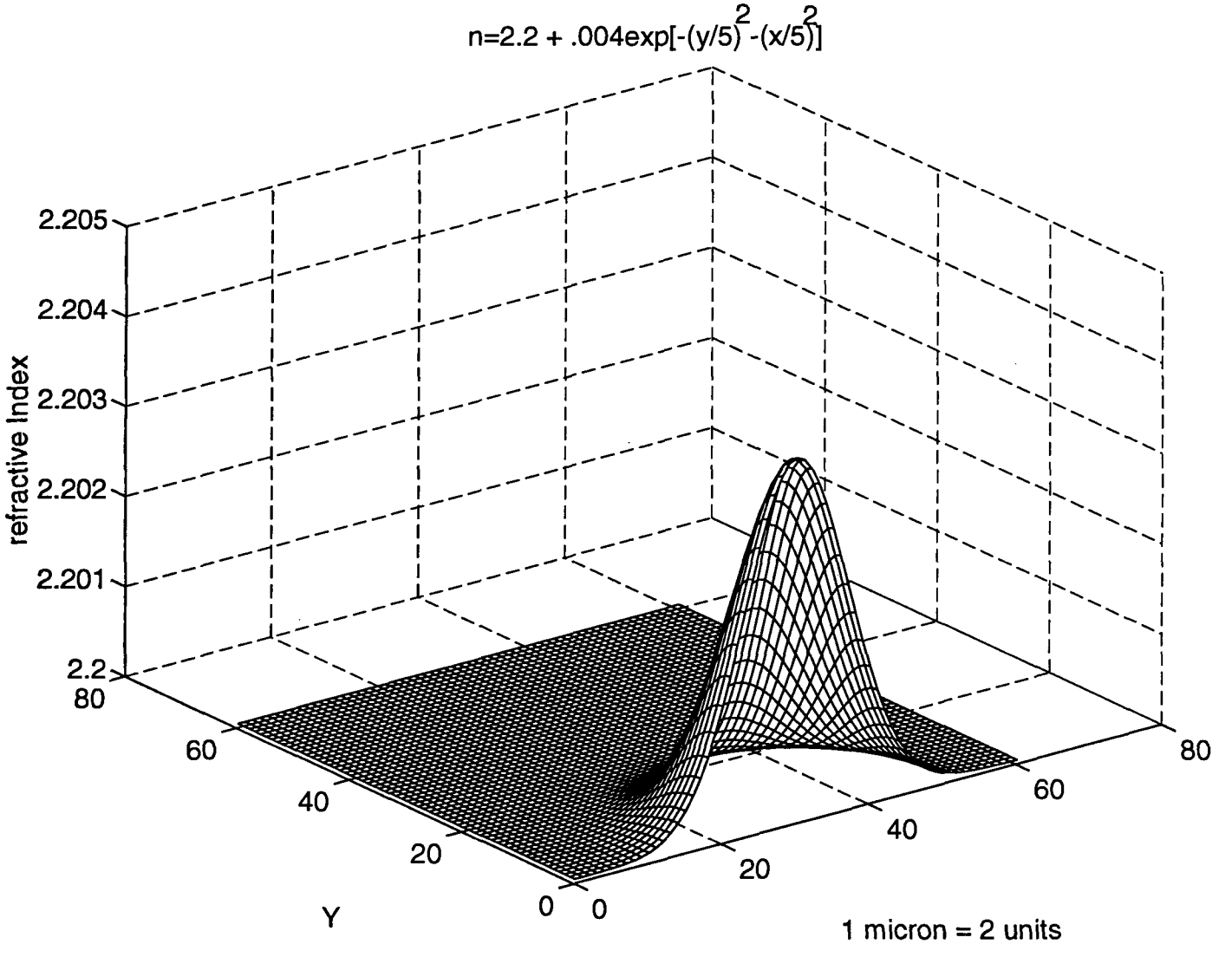

Figure 2.8. The Gaussian refractive index profile used in our calculations.

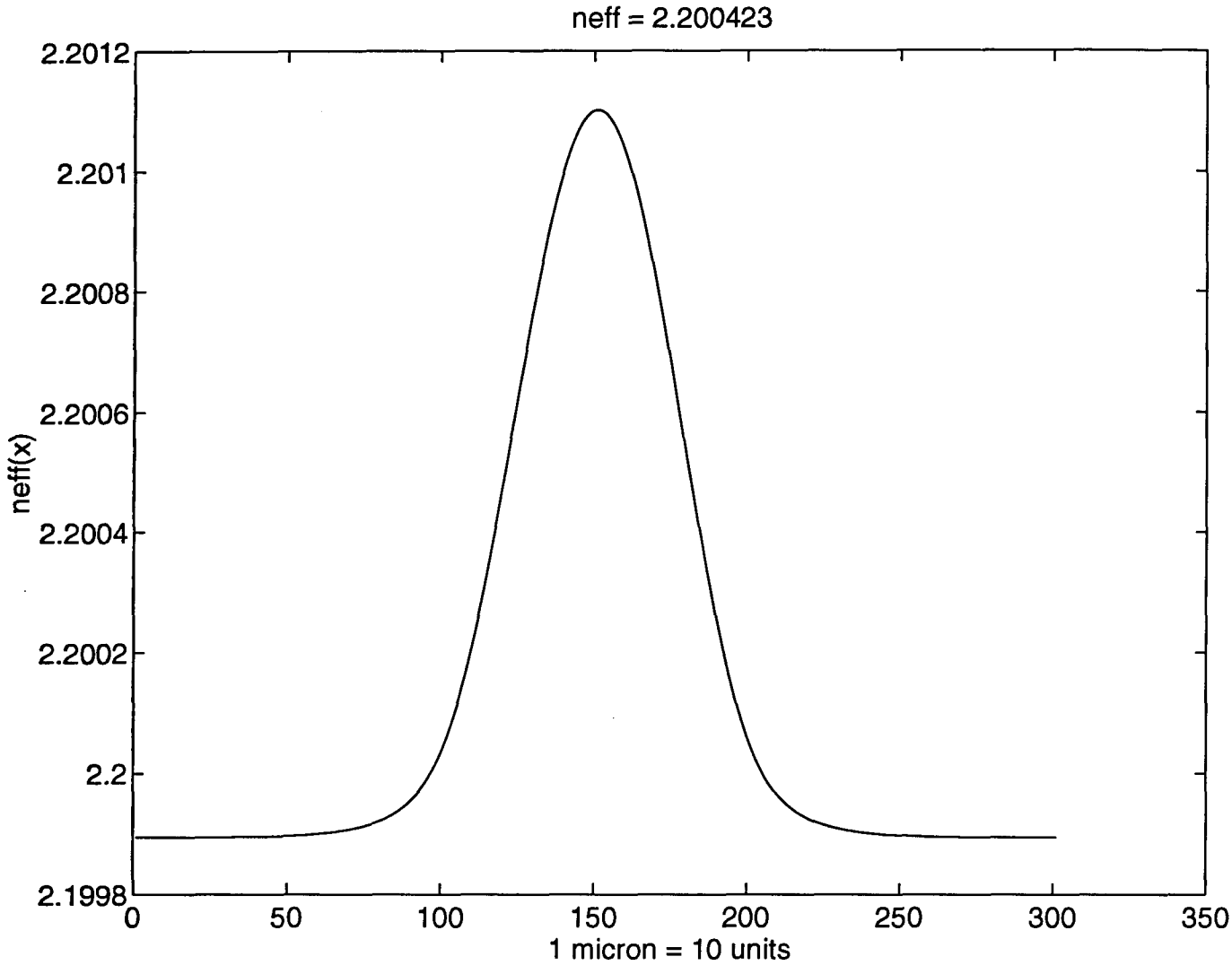

Figure 2.9. The effective refractive index profile in the x-direction for the Gaussian profile, shown in Fig. 2.8, obtained through EIM.

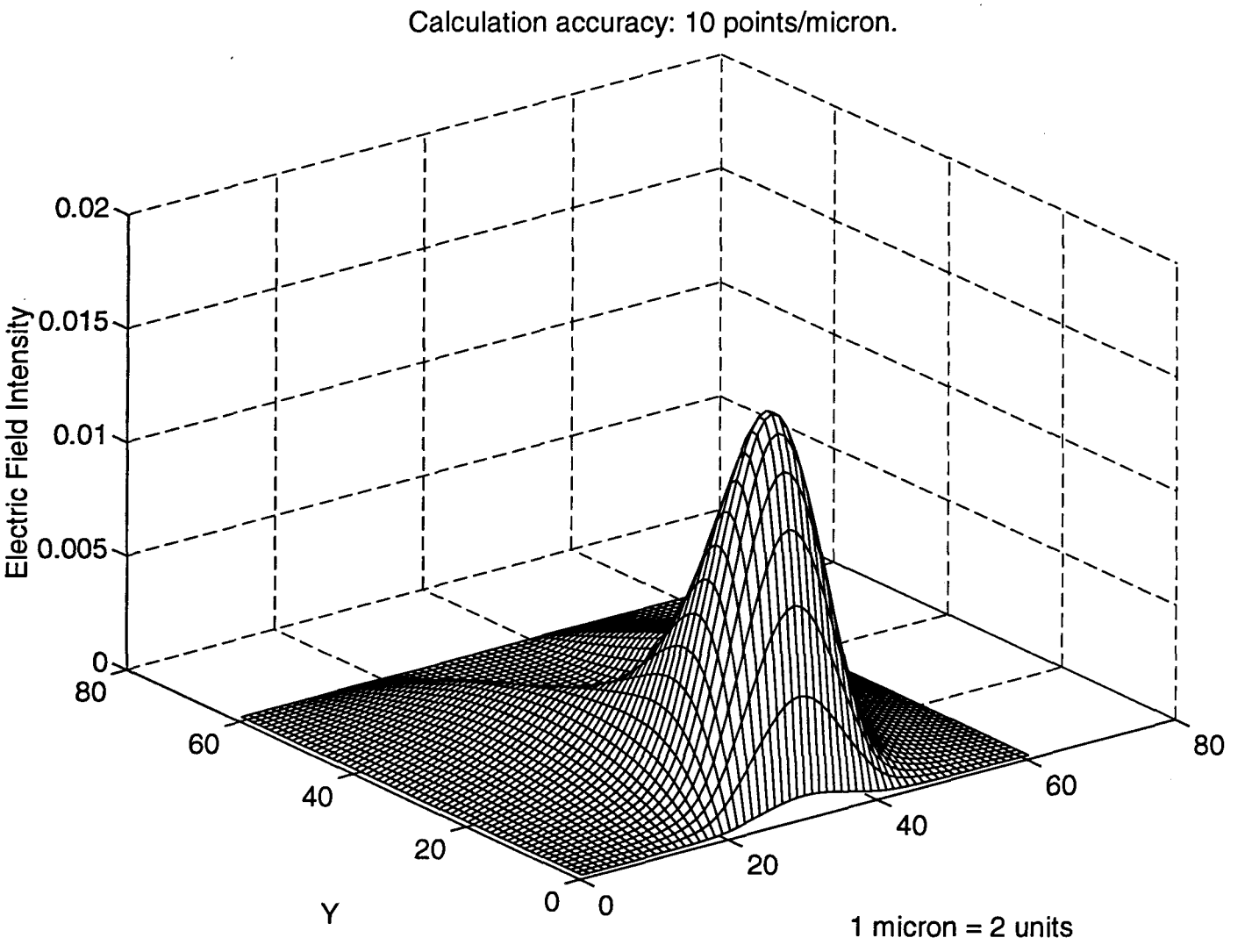

Figure 2.10. The optical field distribution for the Gaussian refractive index profile, shown in Fig 2.8, obtained by EIM.

• 2.3.3 Finite-Difference Method (FDM)

Similar to the EIM we consider a lossless length-invariant channel waveguide running parallel to the z axis having a refractive index distribution *n(x,y)*, in the transverse *x-y* plane. An optical mode propagating along the z axis satisfies the scalar wave equation,

$$\nabla_{xy}^2\Phi + \left[k_o^2 n^2(x,y) - \beta^2\right]\Phi = 0, \tag{2.35}$$

where $\Phi(x,y)$ is the optical field profile, β is the propagation constant of the mode, and k_o, as usual, is the free-space wave number.

The problem is to find optical field distribution of the mode in the *x-y* plane, $\Phi(x,y)$, and its corresponding propagation constants, β. The first step to implement the Finite-Difference approach is the discretisation of $n(x,y)$. We consider a rectangular box encompassing the guiding area and assume that $\Phi(x,y) = 0$ on its boundaries, Fig. 2.11(a). Using a rectangular non-uniform grid, the refractive index, $n(x,y)$, inside the box is divided into elementary cells; within each cell the index is assumed to be constant, Fig. 2.11(b).

The second step is to convert the differential wave equation 2.35, into a finite difference equation (FDE). Using the configuration shown in Fig. 2.11(c), which consists of 4 cells with different n_i's (i = 1,2,3,4), the FDE corresponding to equ. 2.35 will be in the form of [39],

$$\frac{2}{w(e+w)}\Phi_W + \frac{2}{s(n+s)}\Phi_S - \left[\frac{2}{w(e+w)} + \frac{2}{e(e+w)} + \frac{2}{s(n+s)} + \frac{2}{n(n+s)}\right]\Phi_P + \frac{2}{e(e+w)}\Phi_E + \frac{2}{n(n+s)}\Phi_N + k_o^2\frac{wn\times n_1^2 + ws\times n_2^2 + es\times n_3^2 + en\times n_4^2}{(e+w)(n+s)}\Phi_P - \beta^2\Phi_P = 0. \tag{2.36}$$

The above equation shows the relation between the values of electric field at point P and its adjacent points, W,E,N,S, and holds for all the nodes on the grid. For a uniform grid, n = s = w = e = Δ, the above equation reduces to

$$\frac{\Phi_W}{\Delta^2} + \frac{\Phi_S}{\Delta^2} + \left(\frac{\left(n_1^2+n_2^2+n_3^2+n_4^2\right)k_o^2}{4} - \frac{4}{\Delta^2}\right)\Phi_P + \frac{\Phi_E}{\Delta^2} + \frac{\Phi_N}{\Delta^2} - \beta^2\Phi_P = 0. \tag{2.37}$$

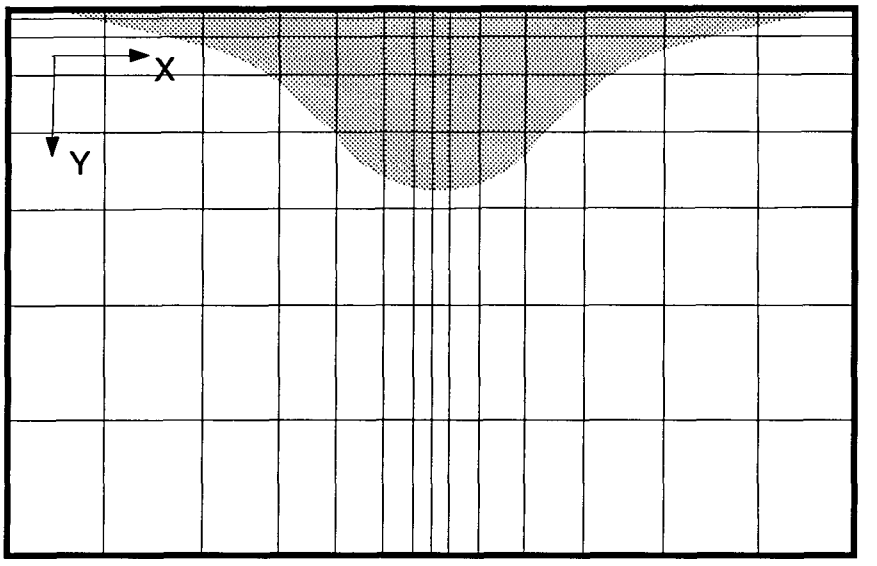

(a)

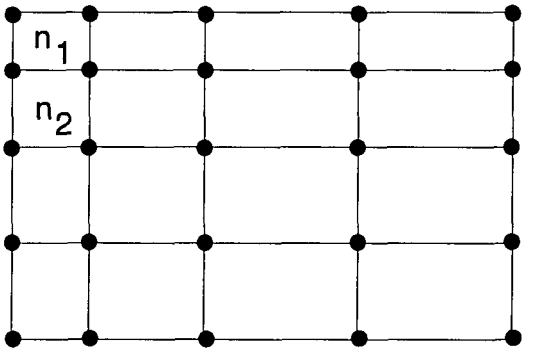

(b)

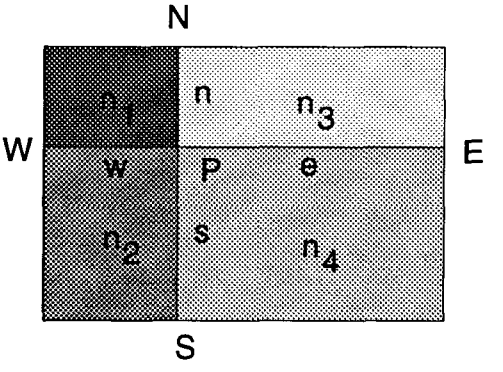

(c)

Figure 2.11. An illustration of finite difference method.

Assuming a grid with N_x and N_y points along the x and y axes, respectively, and $N_{total} = N_x \times N_y$, equ. 2.36 can be written in the matrix form of

$$\{[A] - \beta^2[U]\}[X] = 0, \tag{2.38}$$

where $[X] = [\Phi_k]$ $k = 1...N_{total}$, *[U]* is a unit matrix, and *[A]* is a sparse real $N_{total} \times N_{total}$ matrix. Each eigenvector and eigenvalue of the above equation is an optical field distribution, $\Phi(x,y)$, and its corresponding propagation constant, β^2, respectively.

To find a proper uniform grid for our calculations, at first, the program was run for simple grids having large spacing; the resolution of the grid was gradually increased until the calculated value for n_{eff} converged to at least four significant digits. For *Ti:LiNbO3* channel waveguides having a prediffusion strip width ranging from 6 to 9.5 μm, fabricated under the diffusion conditions specified in subsection 2.3.1, a uniform grid with $N_x = 41$, $N_y = 21$, and 0.5 μm spacing satisfies the above criteria. Figures 2.12 and 2.13, respectively, show the calculated refractive index profile and optical field distribution of a *Ti:LiNbO3* channel waveguide having a 7 μm prediffusion strip width. For the above mentioned waveguides, tables 2.1 (a,b,c) respectively, list the calculated values of 1/e mode sizes, in the width and depth directions, and effective refractive index, n_{eff}, computed through both finite difference and variational methods [26]. The maximum difference between the values calculated by the two methods is 15% for the modal width size and 3% for the modal depth size (as a percentage of FDM value). Since the variational method provides us with a lower bound to the β^2, the calculated values of β^2, by FDM, are, by nature, always higher than those of calculated by variational method.

Table 2.1 Calculated 1/e modal sizes and the propagation constant for various titanium strip widths by FDM and Variational Method (VM).

A. 1/e modal width size (μm).

strip width	6.0 (μm)	6.5 (μm)	7.0 (μm)	7.5 (μm)	8.0 (μm)	8.5 (μm)	9.0 (μm)	9.5 (μm)
FDM	4.88	4.95	5.04	5.13	5.24	5.36	5.49	5.63
VM	5.76	5.80	5.86	5.94	6.04	6.14	6.26	6.38

B. 1/e modal depth size (μm).

strip width	6.0 (μm)	6.5 (μm)	7.0 (μm)	7.5 (μm)	8.0 (μm)	8.5 (μm)	9.0 (μm)	9.5 (μm)
FDM	3.43	3.41	3.38	3.36	3.35	3.33	3.32	3.31
VM	3.55	3.51	3.48	3.45	3.42	3.41	3.38	3.37

C. Propagation constant, β, (μm).

strip width	6.0 (μm)	6.5 (μm)	7.0 (μm)	7.5 (μm)	8.0 (μm)	8.5 (μm)	9.0 (μm)	9.5 (μm)
FDM	2.2030	2.2032	2.2034	2.2035	2.2037	2.2038	2.2039	2.2040
VM	2.2019	2.2020	2.2022	2.2024	2.2025	2.2026	2.2028	2.2029

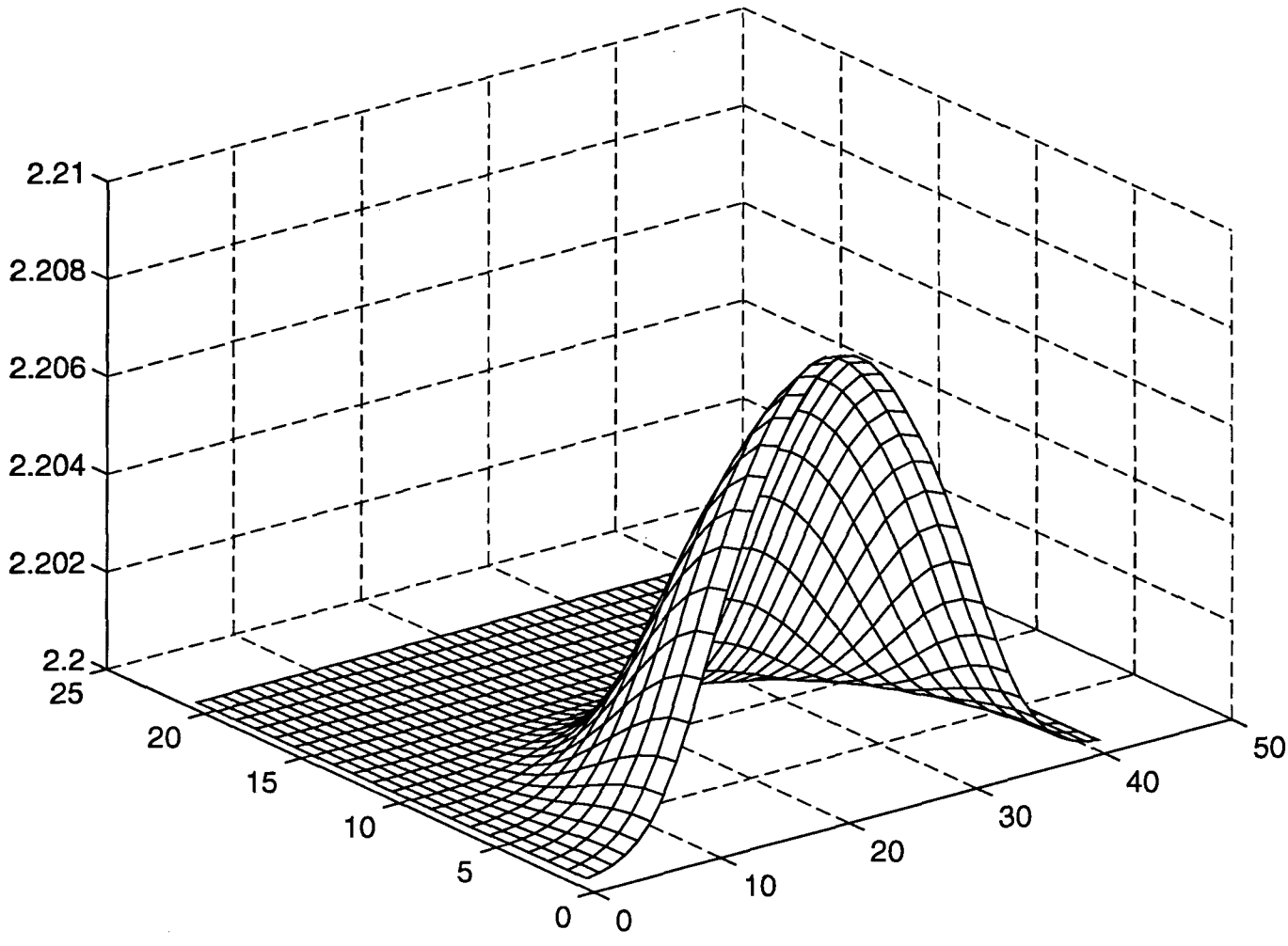

Figure 2.12. Calculated refractive index profile for a *Ti:LiNbO$_3$* channel waveguide having a 7 μm prediffusion strip width fabricated under diffusion condition given in section 2.3.1.

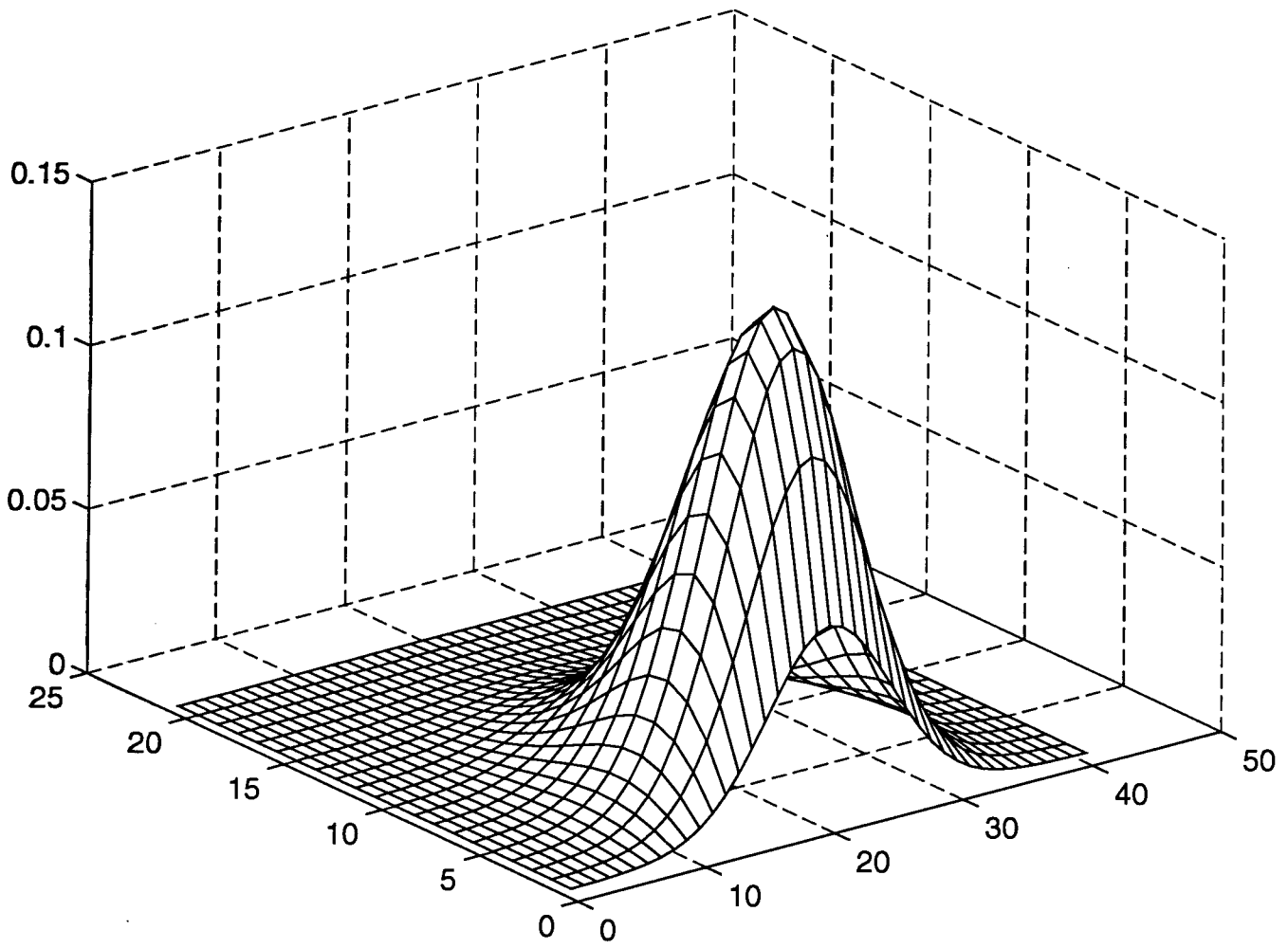

Figure 2.13. The calculated optical field distribution for the refractive index profile shown in Fig. 2.12, obtained by FDM.

Chapter 3: Device Fabrication

§ 3.1 Introduction

Based on the operational theory of the IOPC, described in chapter 2, this chapter lays out the fabrication procedures and integration steps carried out to realize a fully connectorized IOPC sensor.

Lithium niobate is an artificially-made dielectric material which is usually grown in single crystal by the Czochrallsky method. The physical and optical properties of lithium niobate were investigated in detail at Bell laboratories through the sixties [40–44]. Lithium niobate, because of its large electro-optical and acousto-optical coefficients and good transmission characteristics, is suitable for many purposes such as switching, modulation, and sensor applications [18]. Today, a commercially-prepared wafer of lithium niobate grown through the Czochrallsky method can be purchased at a price of a few hundred dollars. Table 3.1 lists a number of specifications of the lithium niobate wafer supplied by Crystal Technology, Inc. (Palo Alto, CA 94303).

Several methods have been developed for the fabrication of optical waveguides in lithium niobate substrate. As the first method, the "outdiffusion technique", was introduced in 1973 by Kaminow and Carruthers [45]. In this technique the substrate is heated to around 1000°C, resulting in lithium outdiffusion from the surface that leads to an increase in the extraordinary refractive index. The waveguides fabricated by this method are able to confine light polarized parallel to the z axis; this method has restricted applications because of the difficulty in producing the lateral light confinement needed in channel waveguides. Another method

Table 3.1. Physical and optical properties of lithium niobate (provided by Crystal Technology Inc.).

Size	y-cut 3.0″diameter × 0.020″ (y)				
Curie temperature	1142.3 ± 0.3°C				
Refractive indices	$@\lambda_o$ = 1150.0 nm n_o = 2.2225, n_e = 2.1519				
Dielectric constants	@25°C unclamped: ϵ_{11} = 84.6, clamped: ϵ_{11}=44.3				
Electro-optic coefficients (pm/V @633 nm):					
		r_{13}	r_{22}	r_{33}	r_{51}	r_z
	unclamped:	10	7	33	33	18
	clamped:	9	3	31	28	19
Piezoelectric strain coefficients (@25°C × 10^{-12} C/N):					
	d_{15} = 69.2		d_{22} = 20.8		
	d_{31} = -0.85		d_{33} = 6.0		

introduced in 1982 by Jackel [46] was the "proton exchange" technique. In this method the Li ions at the surface of the crystal are replaced by hydrogen ions by immersing the substrate in Benzoic acid at temperatures between 200 and 240°C. This process results in an increase in the extraordinary refractive index and a decrease in the ordinary index; therefore this method is useful for applications in which the light is polarized only parallel to the z axis.

The method which has generally received the most attention is "indiffusion method". In it, transition metals such as Ni, V, and Ti are diffused into the $LiNbO_3$ substrate. This method was introduced in 1974 by Schmidt and Kaminow [47]. The fabrication of optical waveguides by this method is based on the fact that the indiffusion of titanium ions into $LiNbO_3$ leads to an increase in both ordinary and extraordinary indices. Since the deposited titanium for indiffusion may be patterned into any desired configuration, fabrication of channel waveguides can easily be carried out.

The fabrication steps necessary to implement the titanium indiffusion technique are explained in detail in section 3.2. Section 3.3 includes a description of system integration

consisting of practical considerations such as fibre to waveguide butt-coupling, fibre connectorization, laser-to-fibre coupling, and so on.

§ 3.2 Fabrication Process of Ti:$LiNbO_3$ Channel Waveguides

The diffusion of titanium ions into lithium niobate substrates leads to an increase in both ordinary and extraordinary refractive indices, and thus provides the required light confinement (regardless of the direction of the polarization of the travelling light) necessary to form an optical channel waveguide in the substrates.

The fabrication process may be outlined as follows: an optically polished $LiNbO_3$ wafer obtained from Crystal Technology is cut to four quadrants; a 700–800-°A-thick titanium film is deposited by metal evaporation. Through lithography and plasma etching the titanium film is patterned to the desired stripe configuration; the indiffusion of titanium strips is carried out at 1050°C for 6.5 hours. In order to protect the fabricated waveguides from possible surface damage, a layer of silicon dioxide, around 3000°A thick, is sputtered on top of the samples as a buffer layer.

The fabrication parameters should be chosen in such a way that the waveguides produced support the propagation of only the fundamental TE- and TM- like modes at λ_o = 1.3 μm. Using the values reported in the literature as an estimate for our initial guess, the numerical modal analyses explained in the previous chapter were used to verify the appropriateness of these adopted values. Table 3.2 lists the fabrication parameters reported in references [20] and [48] compared with the values used in our process. The results of numerical programming for a titanium prediffusion thickness of 700°A listed in tables 2.1 (a b) show that the optical

Table 3.2 Reported fabrication parameters compared with the values used in our process.

Refrences	Titanium Prediffusion Thickness	Prediffusion Strip Width	Indiffusion Time	Indiffusion Temperature
Feit et al. [20]	950°A	6.3 μm	6 hours	1050°C
Korotky et al. [48]	740-850-1110°A	1.5-10 μm (0.5 μm steps)	6 hours	1110°C
Our Values	700 and 770°A	3-10 μm (0.5 μm steps)	6.5 hours	1050°C

mode sizes in the waveguides are comparable to the one in the polarization maintaining fibre (mode field diameter = 8.0 ± 0.5 μm), and hence, the coupling loss between the fibre and waveguide at both ends may be kept to a tolerable level.

The fabrication steps taken to implement the above process are as follows:

a. Aluminum deposition by thermal evaporation, as a protective layer for cutting.

b. Cutting the wafer into four quadrants using a wire saw.

c. Removing the aluminum coating.

d. Titanium deposition using thermal evaporation.

e. Photo-resist deposition, patterning (exposure), and development.

f. Plasma etching.

g. Removing the photo-resist.

h. Titanium indiffusion.

i. Silicon dioxide deposition by sputtering.

j. Cutting the quadrants to proper sizes.

k. Repeating steps a,b, and j for an acoustic grade lithium niobate wafer.

l. Gluing the acoustic grade samples to the optical grade ones.

m. Polishing waveguide ends.

(For the purpose of simplicity, in the above list a few small intermediate steps such as cleaning, mask preparation, etc., are not mentioned.)

Based on the fabrication steps listed above, the following is a more detailed description of the process. In order to use the area of the 3″ $LiNbO_3$ wafer efficiently (the size of the working area on the mask is about 15 mm in width and 33 mm in length), the wafer was cut into four quadrants using a wire saw (model: 850, South Bay Technology, CA). To avoid possible surface damage caused by the abrasive slurry used, and also to reduce the damage to the edges of samples, the surface of the wafer was covered with a coating of aluminum (~ 3000°A) which was deposited by thermal evaporation. After cutting the wafer, the coating was removed.

As explained in section 3.1, based on previous reports and simulation results, two different values for titanium prediffusion thickness of 700 and 770°A were chosen. The titanium film was deposited by the thermal evaporation using a CHA metal deposition system (CHA Industries, Menlo Park, CA).

In order to pattern the titanium film to the desired configuration, a very thin film of positive photo-resist (Shipley S1400–27), was spread over the samples. Photo-resist deposition was carried out by applying a few drops of photo-resist to the samples and then spinning them at 4000 rpm for 35 seconds. To fix the photo-resist, it was pre-baked at 70°C for 20 minutes.

After photo-resist deposition, the samples were aligned with the waveguide mask in such a way that the waveguide strips ran parallel to the z crystallographic axis of the $LiNbO_3$ substrate. Then, the samples were exposed to UV light (λ_o = 320 nm) for 20 seconds using a Karl Suss MJB3 mask aligner (Karl Suss America Inc., Vermont).

A chromium on glass mask, made by E-beam lithography, was used for patterning. The waveguide mask consisted of 10 clusters, where each cluster contained 33–mm-long strips having various widths ranging from 3 to 10 μm, increasing in 0.5 μm steps. The center-to-center distance between adjacent waveguides was 100 μm. Therefore, the working area of the mask was 33 mm in length and 15 mm in width.

The exposed photo-resist was developed in a solution of Shipley MF-319 for 100 seconds. Then the samples were rinsed in DI water to remove residues and placed in a 110°C oven for 15 minutes, to fix the pattern.

Samples were put in the plasma etching machine (model: PK-12, Plasma Therm Inc., NJ) to remove the titanium from the areas not covered by the photo-resist. A flow of CF_4 at a rate of 142 sccm/min at 80°C and in a chamber pressure of 500 mtorr for a period of 20 minutes was used for this purpose. After removing the excess titanium, the photo-resist etchant solution was used to remove the remaining photo-resist. The samples were then rinsed in isopropanol solution and blown dry using compressed nitrogen.

The Tencor Alpha-Step 200 profilometer (Mountain view, CA) was used to measure the thickness of titanium strips. Figure 3.1 shows a typical reading on a sample with titanium prediffusion thickness of 700°A.

In order to diffuse the titanium strips into the lithium niobate substrate, and thus form the desired optical channel waveguides, the samples were put into the Thermco Products' (Orange, CA) diffusion furnace. The indiffusion was carried out at 1050°C for 6.5 hours.

Since the fabricated waveguides are surface devices, in order to provide a low-loss optical buffer layer for light confinment and also to protect the waveguides from possible surface damage, a layer of silicon dioxide about 3000°A thick was sputtered on the samples. The

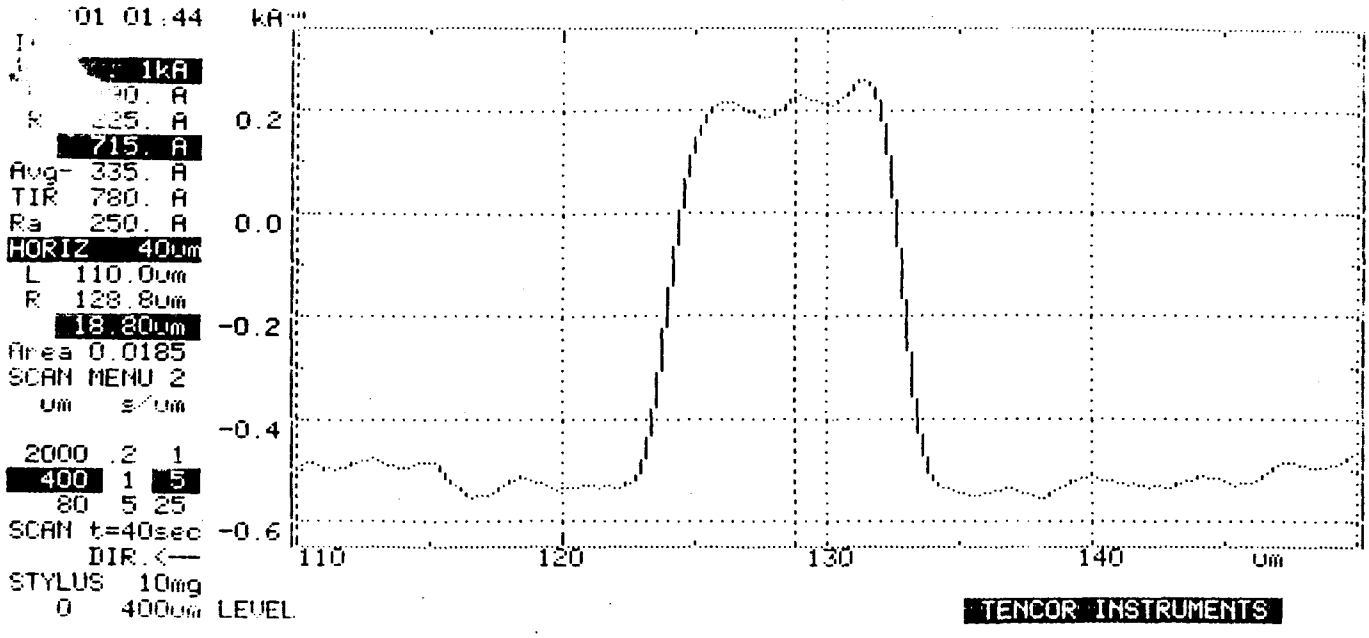

Figure 3.1. A typical reading of titanium prediffusion thickness carried out by Alpha-Step 200 profilometer.

sputtering was carried out by Perkin-Elmer's sputtering machine (model: 3140, Norwalk, CT).

To ease laboratory tests, thin sheets of aluminum about 3000°A thick ware evaporated on the back sides of the samples as electrodes. Then samples were cut to rectangular pieces, about 30 mm long and 18 mm wide, using the wire saw.

In order to facilitate the fibre-waveguide attachment, another piece of lithium niobate was mounted on the top of each sample as the cover piece. Also, since in the final configuration the sensor-head will be mounted on a metal block by gluing the cover piece to the metal surface, the cover piece works as an intermediate layer to reduce the stress applied to the samples. Since the cover piece contains no optical device, an acoustic grade $LiNbO_3$ wafer (which is also less expensive) was used for this purpose. One side of the wafer was covered

by a thin film of aluminum later to be used as an electrode. Then the acoustic grade wafer was cut to exactly the same size as the optical samples. Corresponding pieces were glued to each other to form a complete IOPC sensor-head.

As the final step, the ends of the waveguides (i.e., the edges of the sensor-head normal to the z axis) were polished using a Buehler Ecomet polishing machine (Lake Bluff, IL). At first, samples were polished on a rough 600 grit paper at 1 pound pressure for 10 minutes; then they were ground on a 800 grit paper at 1 pound pressure for 5 minutes. The waveguide ends were examined under the microscope and the later grinding step was repeated until the surface was sufficiently smooth; then, samples were finely polished with a 1 micron alumina slurry on a polishing cloth for 3 minutes which was followed by another 3 minutes of polishing using 0.3 micron alumina slurry, as the last touch.

§ 3.3 IOPC System Integration

This section provides an overview to the system integration procedure including the details of the various alignments and necessary connectorizations. Figure 3.2 shows a schematic view of a fully connectorized system.

System integration begins with coupling the laser light into one of the two polarization axes of the polarization-maintaining (PM) single-mode fibre; in order to increase the polarization ratio of the light before launching it into the waveguide, it passes through an in-line polarizer; then, the input fibre is finely adjusted and glued to the selected waveguide (see chapter 4 for the procedure of finding a proper waveguide). The alignment is done in such a way that the maximum optical power is coupled to the waveguide at the correct polarization

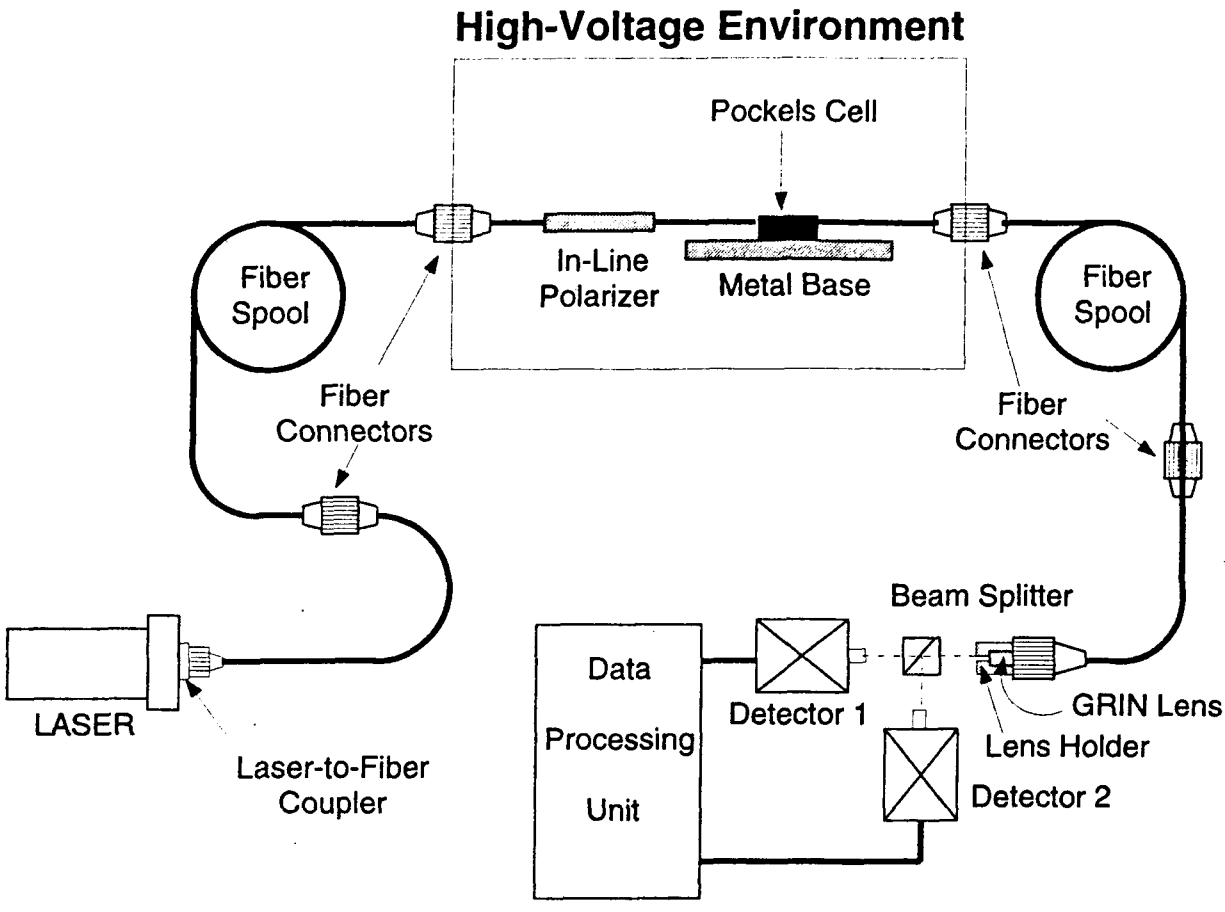

Figure 3.2. A schematic view of a fully connectorized IOPC sensor.

angle (essentially at 45° with respect to x and y crystallographic axes); in a similar way, the output fibre is aligned and glued to the other end of the waveguide. Finally, the output passes through a beam splitter and is decomposed into two components which are detected and measured by two optoelectronic conversion units.

The polarized light, having a polarization ratio of 200:1, was provided using a semiconductor laser (model: LAS-300–1300–6, LaserMax Inc., NY) at λ_o = 1.3 μm and the laser output power was about 6 mW. The PM fibre was obtained from 3M company (West Haven, CT 06516); fig. 3.3 shows a cross section of the fibre. The elliptical element applies an asymmetric stress on the fibre core which, in turn, results in a stress-induced birefringence.

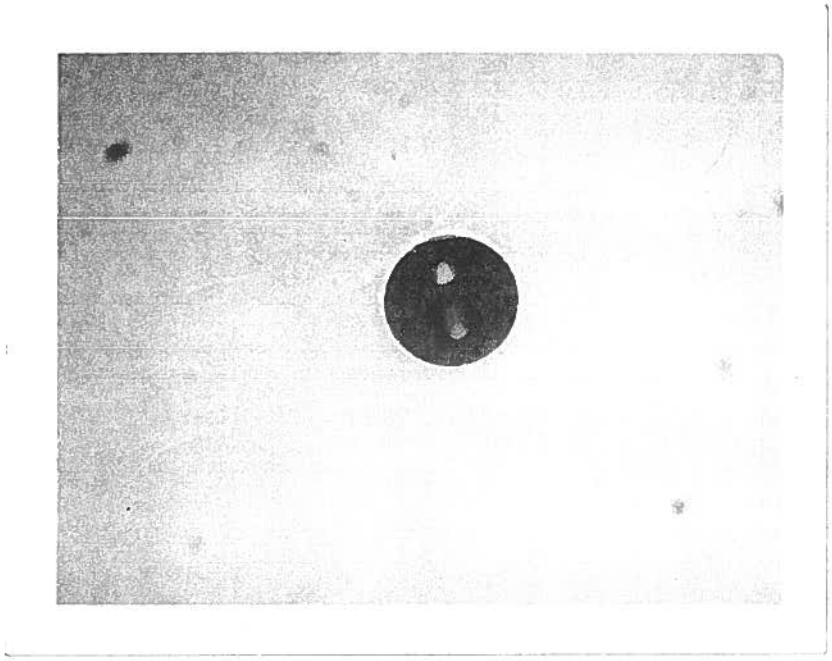

Figure 3.3. The cross section of a PM fibre purchased from 3M company.

For the purchased fibre, the modal field diameter was 8.0 ± 0.5 μm and the fibre and coating diameters were 125 and 250 μm, respectively.

One of the main steps in system integration, repeated for several times, was fibre connectorization. An Oz Optics' (Oz Optics LTD. Ont. K0A 1L0, Canada) connector and adaptor set was used for this purpose. To remove the fibre coating, the fibre end was soaked in trichloroethylene for a few minutes to soften the coating after which it was easily wiped off. The fibres were cleaved using a Deutsch fibre cleaver (Deutsch Optical Waveguide Systems, Banning, CA). Then, the surface of the bare fibre was covered with a low stress glue and it was passed through the ferrules of the polarization preserving connectors. To avoid light scattering from the fibre end, the end face should be sufficiently smooth. After fibre connectorization, the fibre end was polished using Buehler's fibremet optical fibre polishing

machine and then, the end face was examined under the microscope. The polishing procedure consisted of polishing on a rough polishing disk for 3 minutes and using a soft disk for 3–10 minutes, until all chips are removed. Finally, the fibre end was cleaned in DI water and alcohol.

For fibre-to-fibre coupling, the ends of connectorized fibres were contacted together using an Oz Optics' PMPC-03 adaptor. To reduce the coupling loss at the contact interface, an optical silicone gel with a refractive index close to that of the optical fibres' was applied to the ferrules' ends. Figure 3.4 shows two connectorized fibre connected through the PMPC-03 adaptor.

To launch the laser light into the fibre, an Oz Optics' HPUC-23–1300–P-1 laser-to-fibre coupler was used. The coupler consisted of the following parts: a focusing lens for end-firing, an adjustable stage to finely place the fibre core at the focal point of the lens, and a female connector compatible with our polarization preserving connector. Figure 3.5 shows the assembled set of: the laser, the laser to fibre coupler, and the connectorized fibre. The output power at the other end of fibre was about 1.2 mW, which, in comparison with the laser's optical power (about 6 mW), showed a 7 dB loss.

The in-line polarizer (model: 917P, Canadian Instrumentation and research LTD., Ont. Canada) was connectorized at one end and connected to the input fibre spool. Then, the other end was butt-coupled to the proper waveguide. In order to attach the fibre to the lithium niobate crystal, the sensor head was mounted on a metal block; the polished end of the input fibre was clamped on a micro-positioner stage and moved close to the edge of the crystal. Then, the fibre end was precisely aligned with the selected waveguide until the maximum optical power was coupled to the waveguide. In the mean time, the micro-positioner stage

was rotated so that the optical powers in the TE- and TM-like modes at the output were equal. Next, the fibre was moved carefully toward the waveguide and glued to the crystal by a UV-curing low-shrinkage Norland optical adhesive (model: NOA61, Norland Products Inc. New Brunswick, NJ). The glue was cured by exposing it to UV light for 5 minutes every one hour. In a similar way, the interrogating fibre was aligned and attached to the output of the waveguide. Figure 3.6 shows the assembled sensor-head mounted on the metal block.

The light exiting the interrogating fibre's end was collimated using a graded-index rod lens (GRIN lens, Newport Instruments, Canada Corporation, Mississauga, Ont.). The collimated light passed through a beam splitter cube and was decomposed into two normal components, corresponding to the TE- and TM-like modes, which were measured by two photodetectors (model: 2011 IR, New Focus Inc. CA). The optical power received by each detector was about 100 μW which was sufficient for accurate measurements (see section 4.2). The total loss associated with the setup was about 15 dB. Figure 3.7 shows a close-up view of the position of the beam splitter cube with respect to photodetectors.

The electrical output of the detectors are received by the data processing unit which measured the normalized power by dividing the output of each detector by the sum of the readings. Figure 3.8 shows a complete IOPC sensor successfully set up in our laser laboratory.

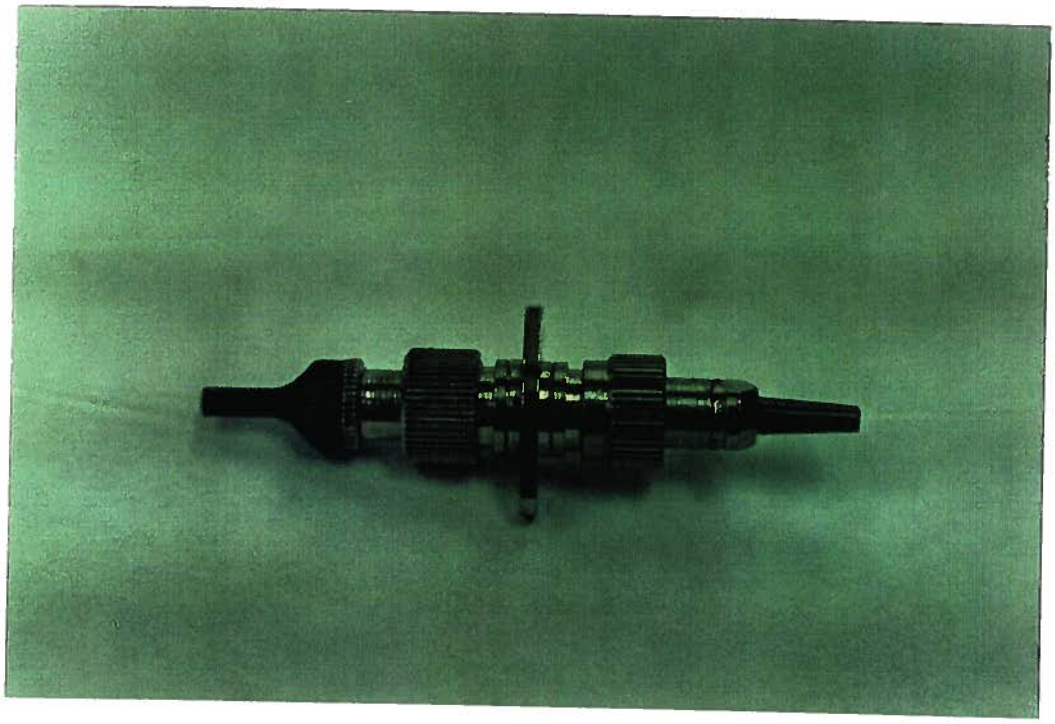

Figure 3.4. A fibre-to-fibre connection using the PMPC-03 adaptor.

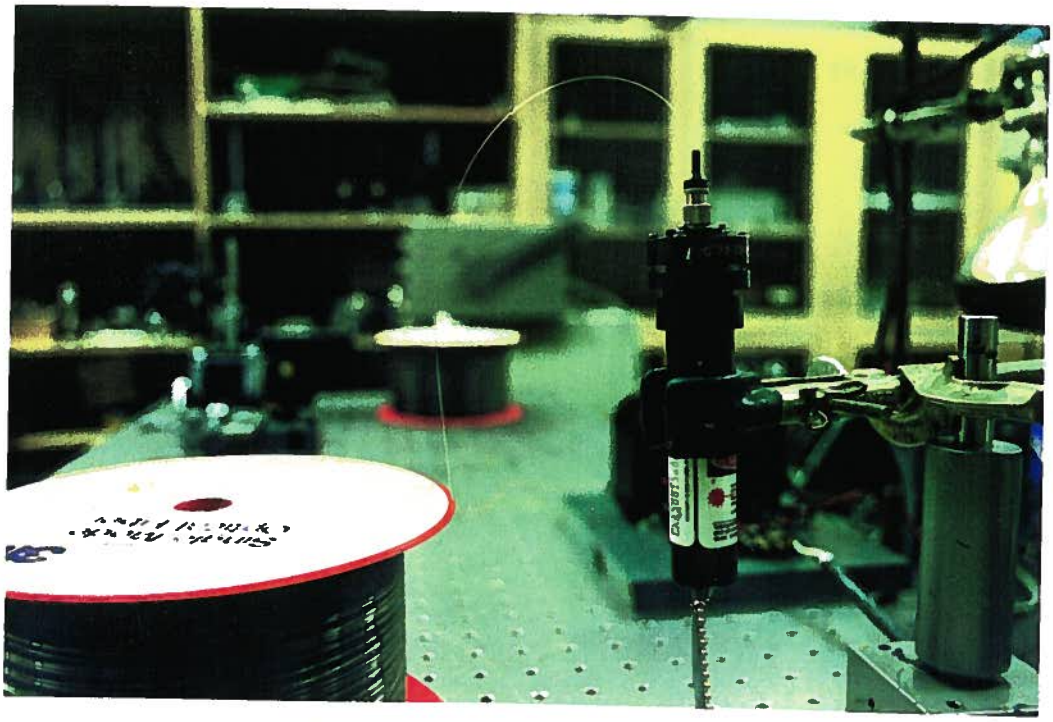

Figure 3.5. A laser-to-fibre-coupling assembly using the HPUC coupler.

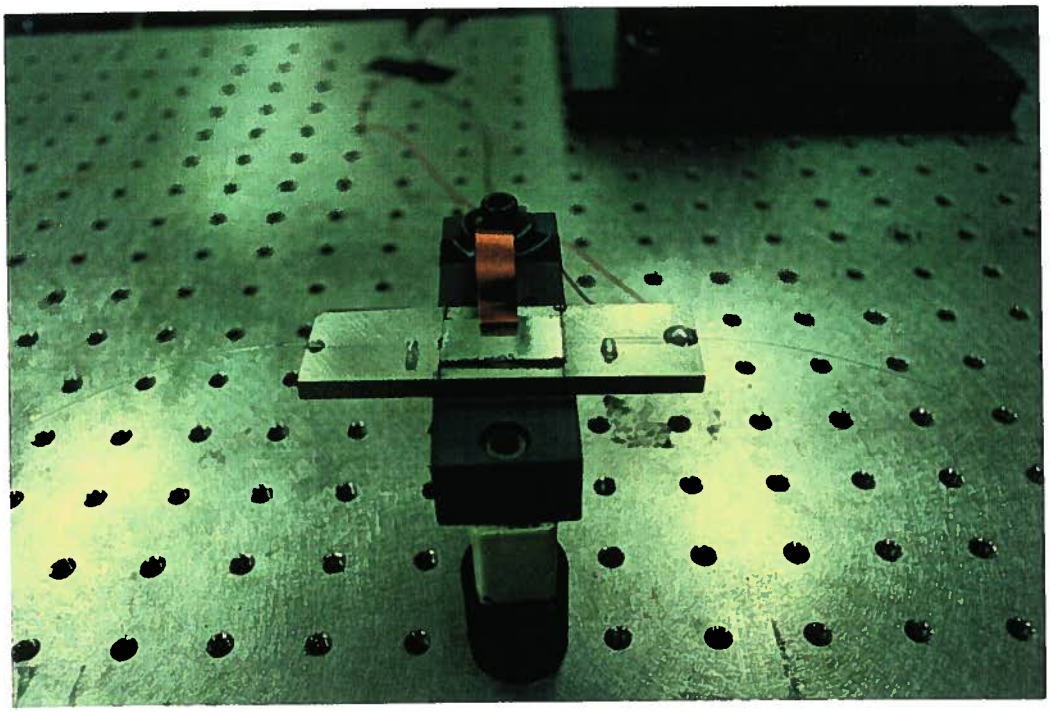

Figure 3.6. The assembled sensor-head mounted on the metal block.

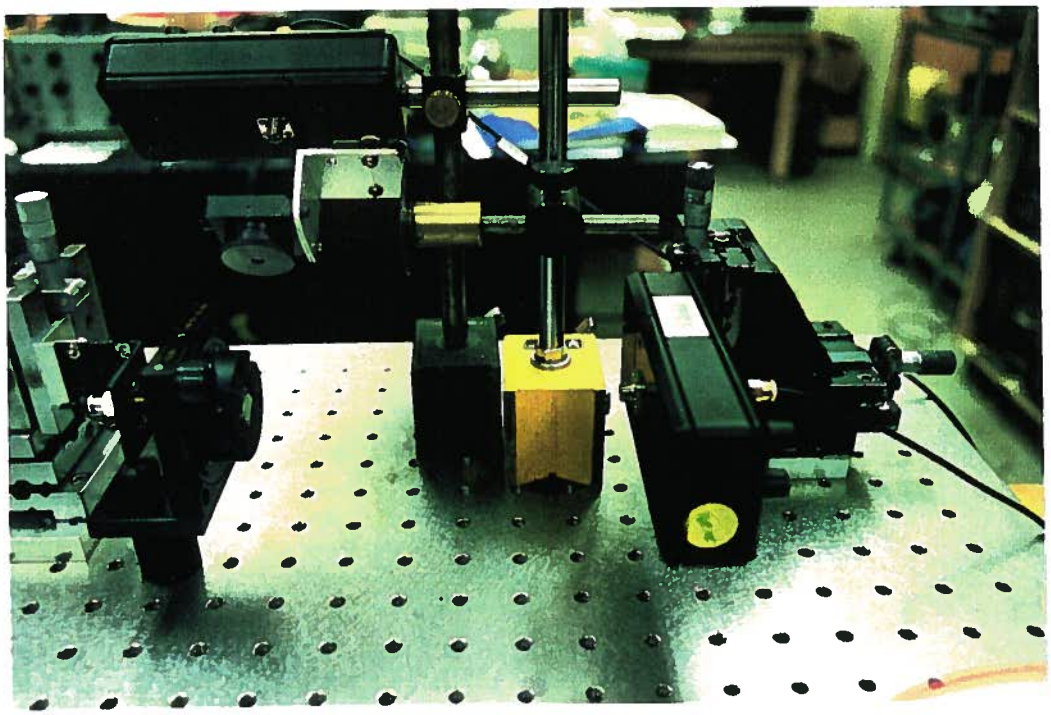

Figure 3.7. A view of the polarizer cube position with respect to the detectors.

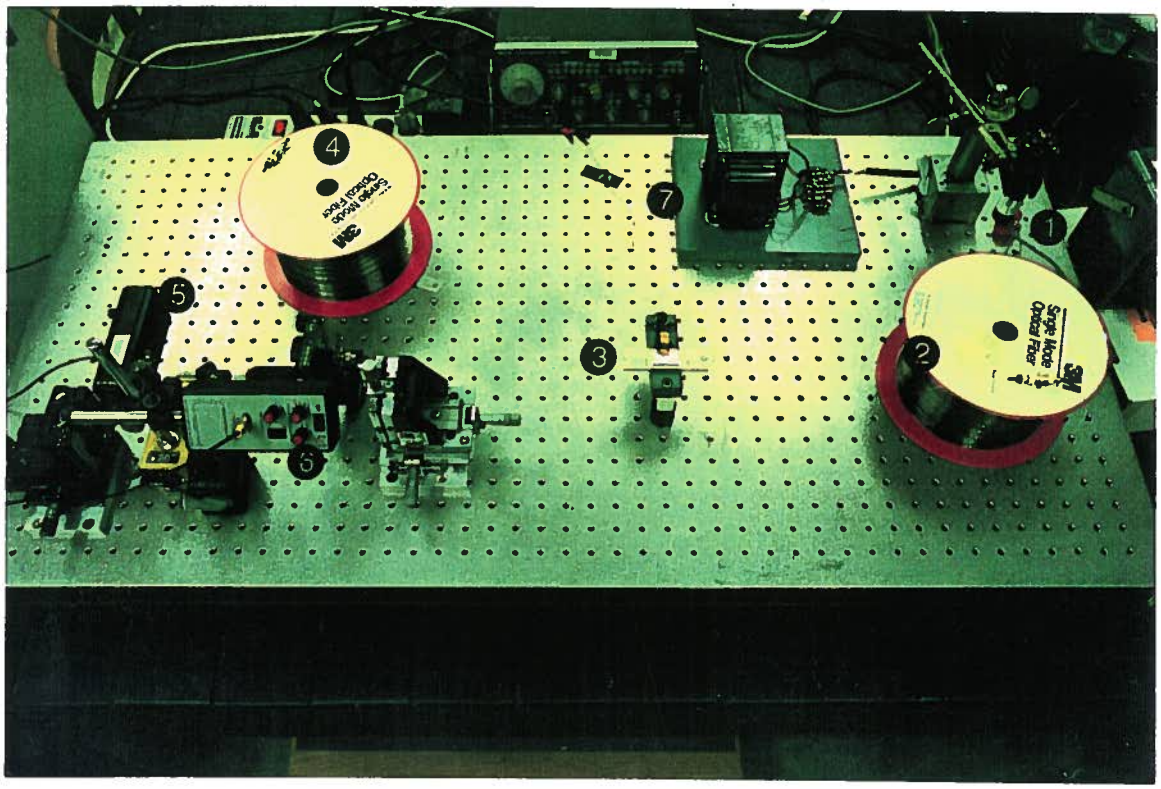

Figure 3.8. A view of a fully-connectorized IOPC sensor set up in the laser laboratory: 1. laser, 2. and 4. fibre spools, 3. sensor-head, 5. and 6. photodetectors, 7. high-voltage transformer.

Chapter 4: Measured Results

§ 4.1 Introduction

Various tests were conducted, on the fabricated IOPCs, to measure device characteristics and evaluate their performance under various conditions. The experiments performed fall into two different categories. The first type were ones done to measure the device specifications and their dependence on fabrication and physical parameters; e.g., the measurement of intrinsic phase (bias) and its dependence on waveguide length and prediffusion strip width, the half-wave electric field, and the on/off (extinction) ratio. The second type included experiments conducted to study the accuracy and to specify the proper working range of the device; e.g., the tests of the accuracy and linearity of readings and their temperature dependence, the effect of piezoelectric resonances on the bandwidths, and time-domain impulse responses.

§ 4.2 Device Characterization

After the fabrication of the sensor-head (by sensor-head we mean the substrate plus the cover piece, i.e., an optical-grade piece of lithium niobate containing Ti:$LiNbO_3$ channel waveguides as the substrate and the acoustic grade lithium niobate chip glued to the substrate), the first step was to scan all the devices in order to pinpoint the best waveguides, in terms of device intrinsic phase, on/off ratio, and output optical power. A lens setup, described below, was used to scan the various waveguides and to measure the above characteristics. A

25× objective lens focused the laser beam onto the end of the waveguide and another 10× objective lens collimated the light at the output of the waveguide. The sample was placed on a micro-positioner so that the various waveguides could be accessed easily, by simply moving the device. A New Focus 2011 IR photodetector (New Focus Inc. CA 94089, USA) converted the optical signal to an electrical one which, in turn, was measured using an HP 54600 digital oscilloscope. The measured signal was transferred to a personal computer where it was processed to extract the necessary information.

The relationship between the applied electric field and the normalized output intensity is given by 2.13,

$$S = \frac{1 \pm \alpha \cos\left(\pi \frac{E_y}{E_\pi} + \phi_i\right)}{2}, \tag{4.1}$$

where E_y is the applied electric field in the y direction, E_π is the half-wave electric field, ϕ_i is the intrinsic phase, and α is an empirical constant close to 1. In order to apply a proper electric field in the y direction to the sensor, two thin metal films were evaporated onto both sides of the device (on y plates). Since, for these devices the experimental value of the half-wave electric field is around 500 V/mm; assuming that the dielectric constants of the cover piece and substrate are the same and that the total thickness of the device, d, is close to 1 mm, the half-wave voltage that needs to be applied to the electrodes is about 500 V, which can easily be provided by a transformer in the lab.

Figure 4.1 shows a typical transfer function of the electrical-field-in/optical-intensity-out. The intrinsic phase of the device may be obtained from

$$\phi_i = 180^\circ \times \frac{V_a}{V_\pi} \tag{4.2}$$

where V_π is the half-wave voltage, $V_\pi = E_\pi \times d$ and V_a, is the absolute value of the voltage necessary to have a maximum optical intensity at the output. For the transfer function shown

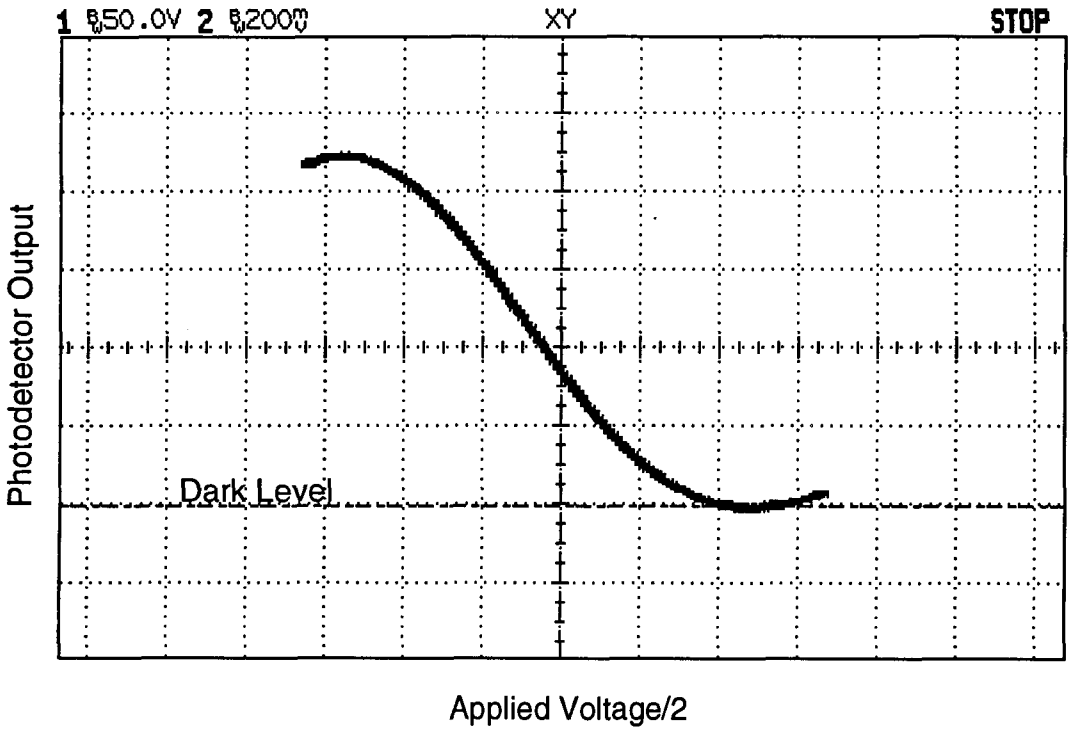

Figure 4.1. A typical IOPC transfer function.

in 4.1 ϕ_i is equal to 100.8°. The ideal value for ϕ_i is 90° for which the normalized output intensity takes the following form

$$S = \frac{1 \mp \alpha \sin\left(\pi \frac{E_y}{E_\pi}\right)}{2}. \tag{4.3}$$

A bias close to 90° has two advantages. First, the working point will be located near a region of transfer function which has the steepest slope and therefore the sensitivity of the output signal to the applied voltage is maximum. Second, if the term $\pi E_y/E_\pi$ is less than 8°, the linear approximation of the sine function, i.e. $\sin(x) \approx x$, produces less than 0.3% error; this range of linear approximation is quite appropriate for most applications, e.g., for E_π=500 V/mm and a dielectric constant of 84.6 for lithium niobate (provided by Crystal Technology, Inc. California, USA), electric field intensities less than 1.88 MV/m (in free

space) fall into that linear range. In the next two sections we discuss two possible ways to achieve a desired bias by changing the prediffusion titanium strip width and/or adjusting the length of the device.

The extinction ratio (or on/off ratio) is defined as the ratio of the maximum value of the modulated output intensity to the minimum value, i.e.,

$$R = \frac{1+\alpha}{1-\alpha}. \tag{4.4}$$

When α=1, R goes to infinity; but as discussed in chapter 2, because of alignment imperfections and the polarization ratio of the input light, α has a value less than one and therefore R in practice is of the order of 10^2–10^3, e.g., the measured extinction ratio for the transfer function shown in figure 4.1 is 136 (or 136:1).

The half-wave electric field, as defined in chapter 2, is

$$E_\pi = \frac{\lambda_o}{2n_o^3 r_{22} L}. \tag{4.5}$$

For a device 29.1 mm long (L) and 0.86 mm thick (d), the calculated value of V_π is 378V (for r_{22}=5.4 pm/V at λ_o=1.15 μm [16]), while the measured value of V_π is around 500 V. A possible reason for this discrepancy is that the value of r_{22} for a clamped sample is much lower than the one for an unclamped device (unclamped sample: r_{22}=7 pm/V, clamped sample: r_{22}=3 pm/V at λ_o=0.633 μm, supplied by the manufacturer), therefore glueing the sample to the cover piece may reduce r_{22}. Also, the value of r_{22} at a longer wavelength, such as 1.3 μm, is less than that at 1.15 μm. The measured values for V_π suggest a value of 4.1 pm/V for r_{22} in our case; the half-wave voltage of the device shown in figure 4.1 is 522 volts.

In order to have accurate readings, a MATLAB program was used to obtain a least square fit of the measured data, for each waveguide, to

$$I = I_{dc} + A\cos\left(\pi\frac{V_y}{V_\pi} + \phi_i\right) \tag{4.6}$$

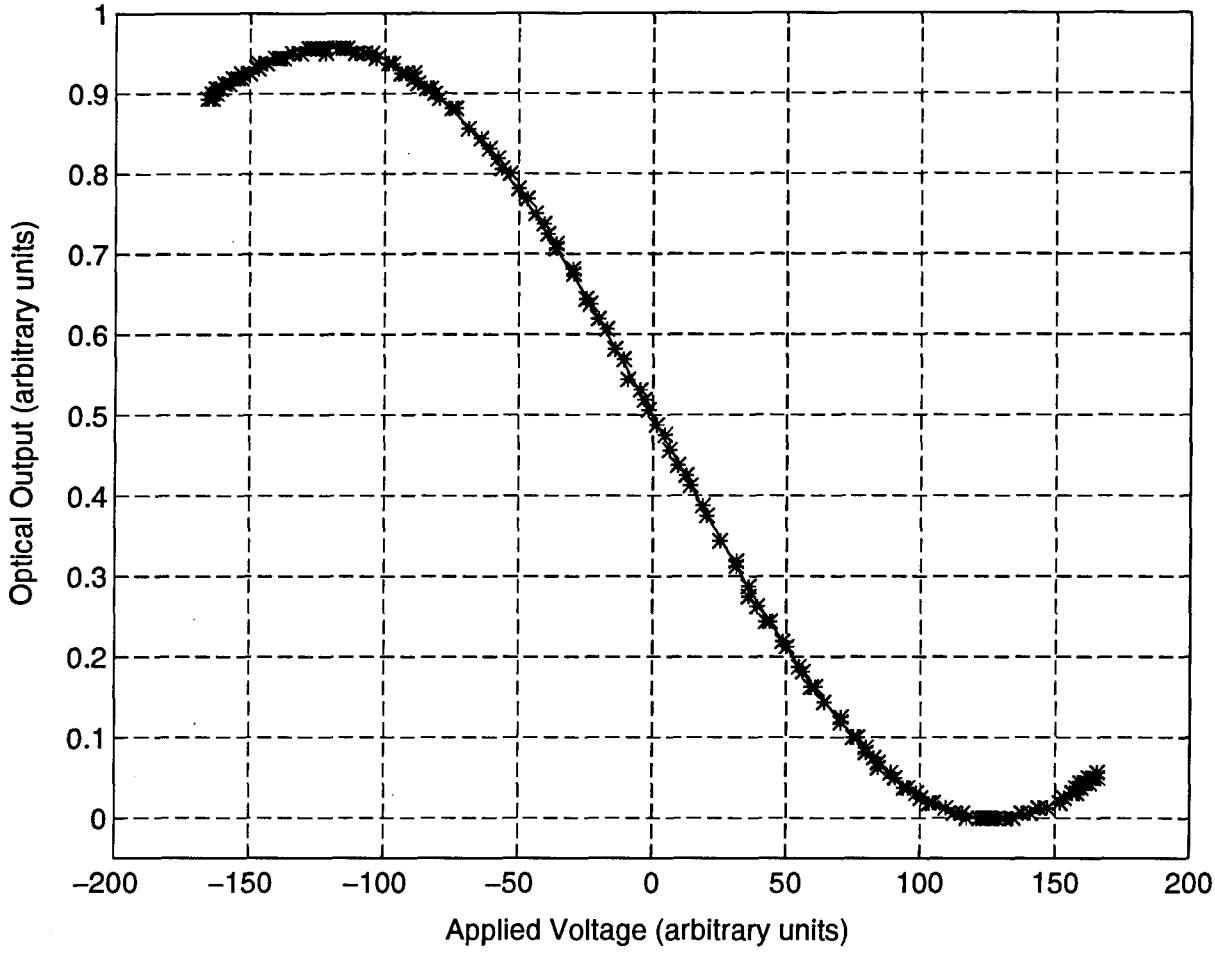

Figure 4.2. Sampled data and the fitted sinusoid (equ. 4.6).

where V_π is the half-wave voltage, ϕ_i is the intrinsic phase of the device, and the fitting parameters A and I_{dc} are the amplitude and dc value of the signal, respectively. The extinction ratio can then be calculated from $R=(A+I_{dc})/(A-I_{dc})$. Figure 4.2 shows measured data for a typical device, indicated by asterisks, and the fitted curve, shown by the solid line.

In addition to a bias close to 90° and a good extinction ratio, it is important that the optical intensity received by the photodetectors be higher than a certain level. Based on the information provided by New Focus Inc. an optical input power of 50 μW can be measured

Table 4.1. Device parameters for a number of fabricated waveguides.

Cluster No.	Device length (mm)	Strip Width (μm)	Titanium Thickness	Bias (degrees)	V_π (volts)	On/Off Ratio
3	29.1	9	770	349	487	235
5	29.1	7	770	81	479	340
6	29.1	8.5	770	275	483	276
6	29.1	7	770	85	487	281
3	28.5	9	700	155	502	243
3	28.5	8.5	700	97	498	304

with a signal-to-noise ratio of 30 dB. For a completely integrated system the amount of optical power received by each detector is around 100 μW, which is quite sufficient for an accurate measurement using our photodetectors.

Table 4.1 lists the intrinsic phase, extinction ratio, and half-wave voltage for various waveguides with different prediffusion strip widths. Figure 4.3 shows a typical transfer function for an IOPC, as seen on oscilloscope screen, and figures 4.4–7 show the output of detectors 1 and 2 in the large-signal and small-signal regimes.

§ 4.3 Device Prediffusion Strip Width

As explained in chapter 3, the mask used for device fabrication produces a number of waveguides having titanium strip widths ranging from 3 to 10 μm, increasing in 0.5 μm steps.

The titanium prediffusion strip width directly affects the width of the fabricated waveguide (see section 2.3) and therefore determines both the number of guided modes and their modal sizes. If the diffused waveguide is too narrow, for the wavelength λ_o=1.3 μm, no guided mode will propagate in the waveguide, and, on the other hand, if the waveguide is

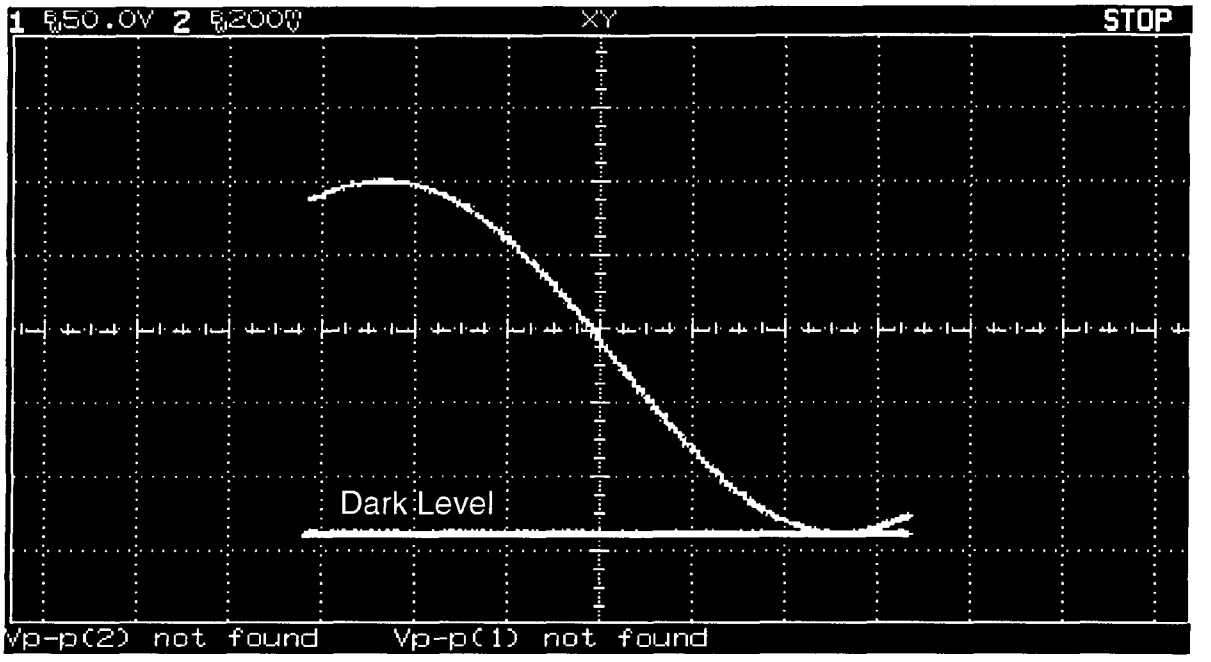

Figure 4.3. A typical transfer function along the *u* axis (see Fig. 2.4).

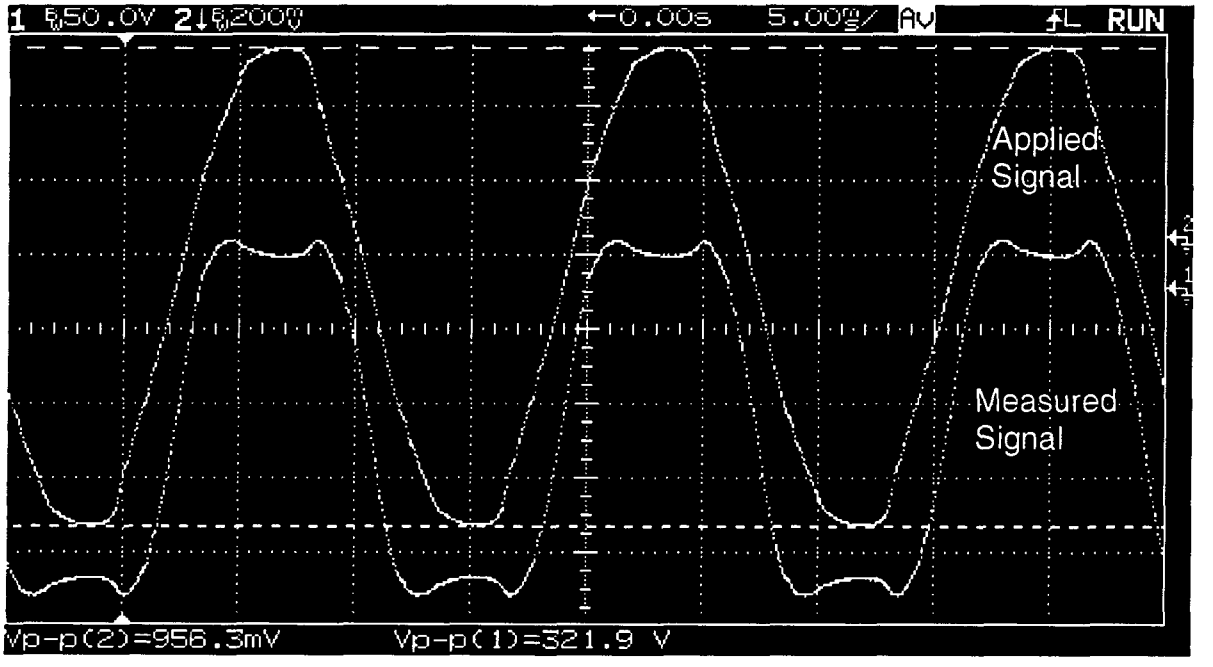

Figure 4.4. Output of detector 2 along the *v* axis, in the large-signal regime.

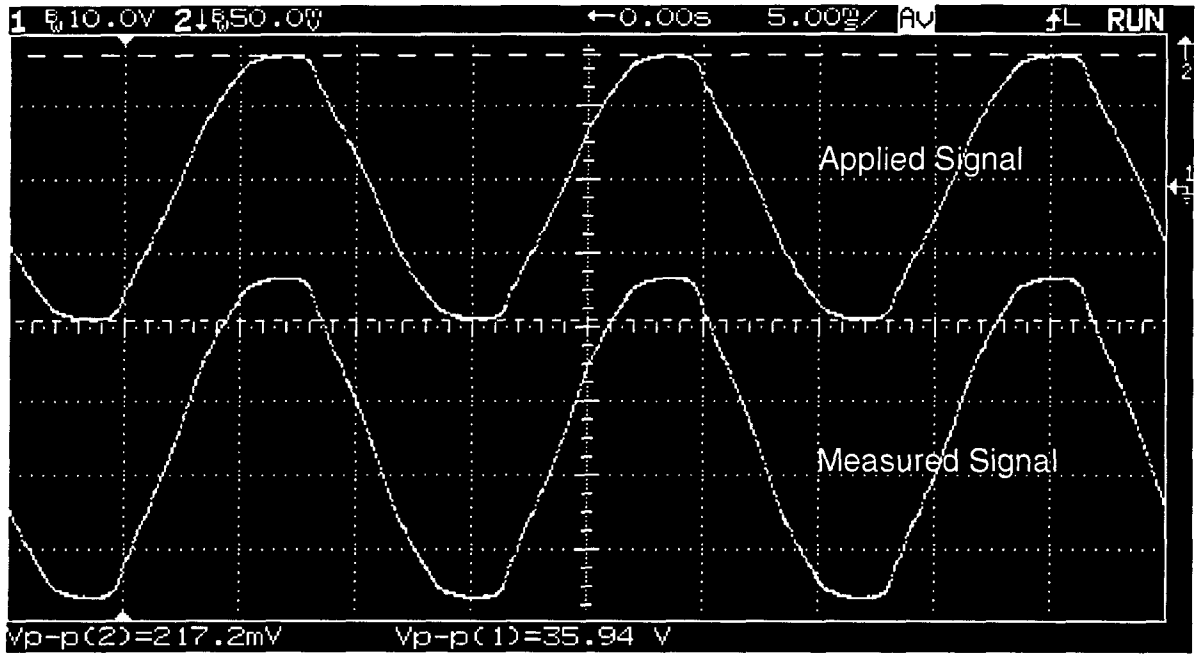

Figure 4.5. Output of detector 2 along the *v* axis, in the small-signal regime.

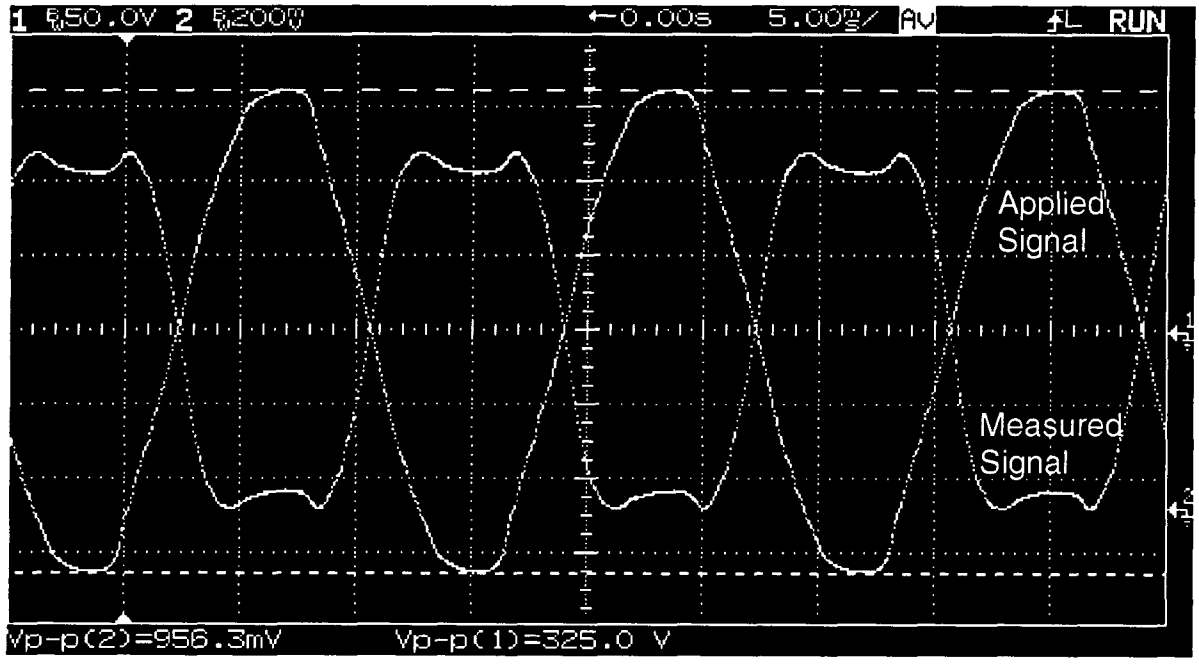

Figure 4.6. Output of detector 1 along the *u* axis, in the large-signal regime.

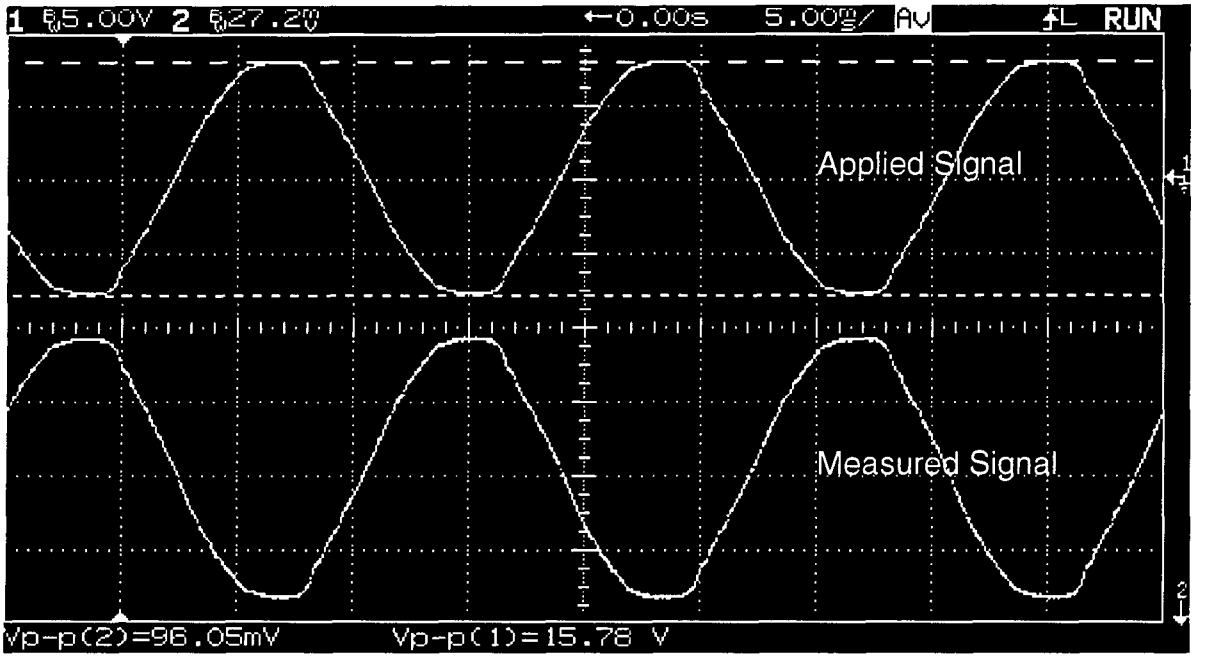

Figure 4.7. Output of detector 1 along the *u* axis, in the small-signal regime.

too wide it guides both fundamental modes as well as higher order ones, i.e., the device is multi-mode. Since the mode profiles and the propagation constants of the higher order modes are different from those of the fundamental modes, a multi-mode device does not have a good extinction ratio and, also, its bias depends on the optical power coupled to each guided mode. Therefore, in order to have the fabricated device behave predictably we avoid using multi-mode devices.

The prediffusion strip width also affects the modal sizes. A narrow waveguide can not confine the light to the guiding region very well and, therefore, produces relatively large mode sizes both in the width and depth directions. If we increase the width of the waveguide the light is better confined to the guiding area and, therefore, both mode sizes decrease. If we further increase the width of the waveguide the modal width size increases again and the structure, relatively quickly, becomes a multi-mode waveguide. Since large modal sizes

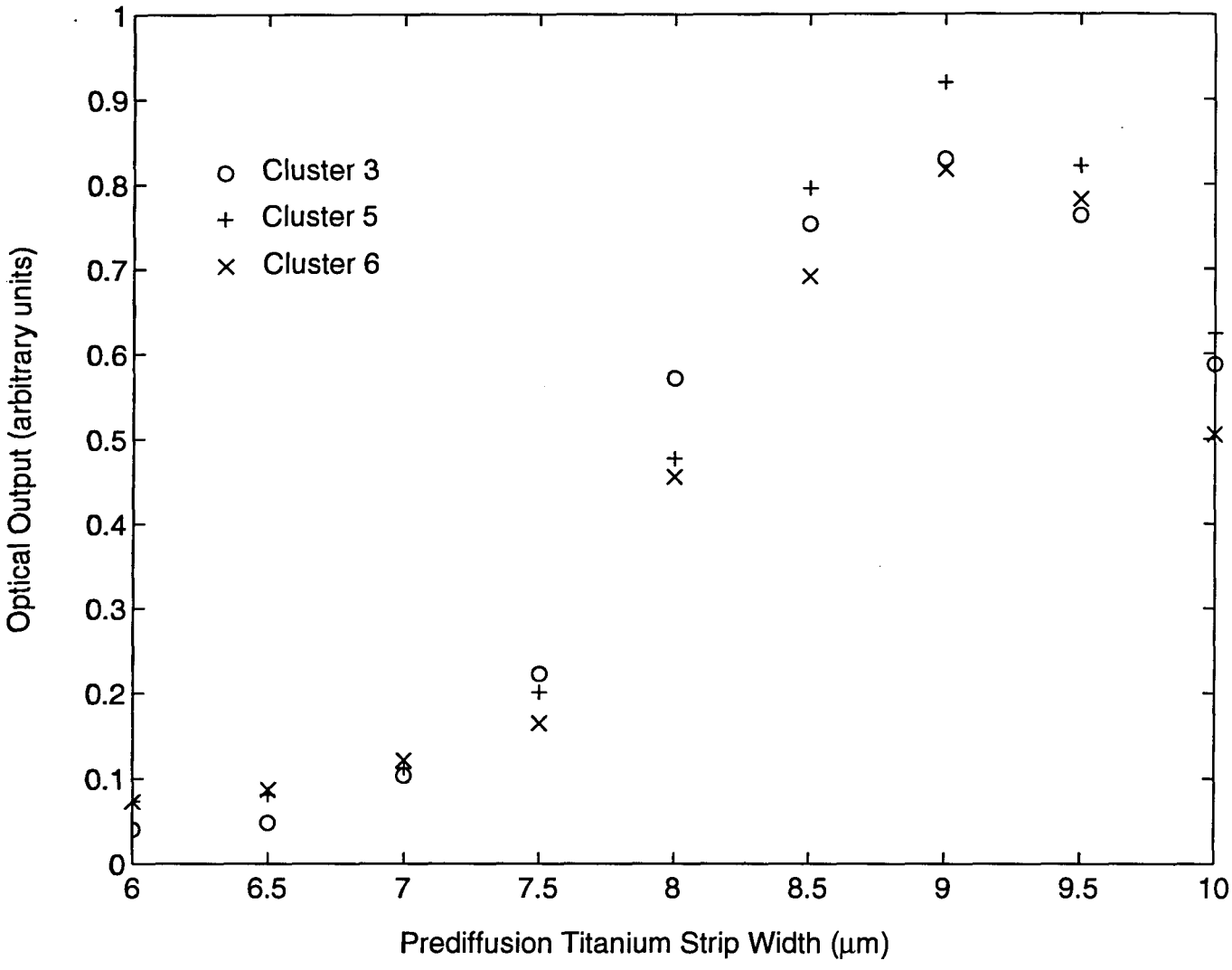

Figure 4.8. The optical output power as a function prediffusion strip width.

cannot be coupled to the fibre or focused very well onto the sensing area of the detector, we expect to have a decrease in our intensity measurements for poorly guiding waveguides (waveguides that do not confine the light very well) and multi-mode ones. Figure 4.8 shows, that for the fabrication conditions given in chapter 3 and prediffusion titanium thickness of 770 °A, fabricated waveguides having prediffusion titanium strip widths less than 8 μm may be categorized as poorly guiding waveguides and waveguides having a 10 μm or greater strip width as being multi-mode.

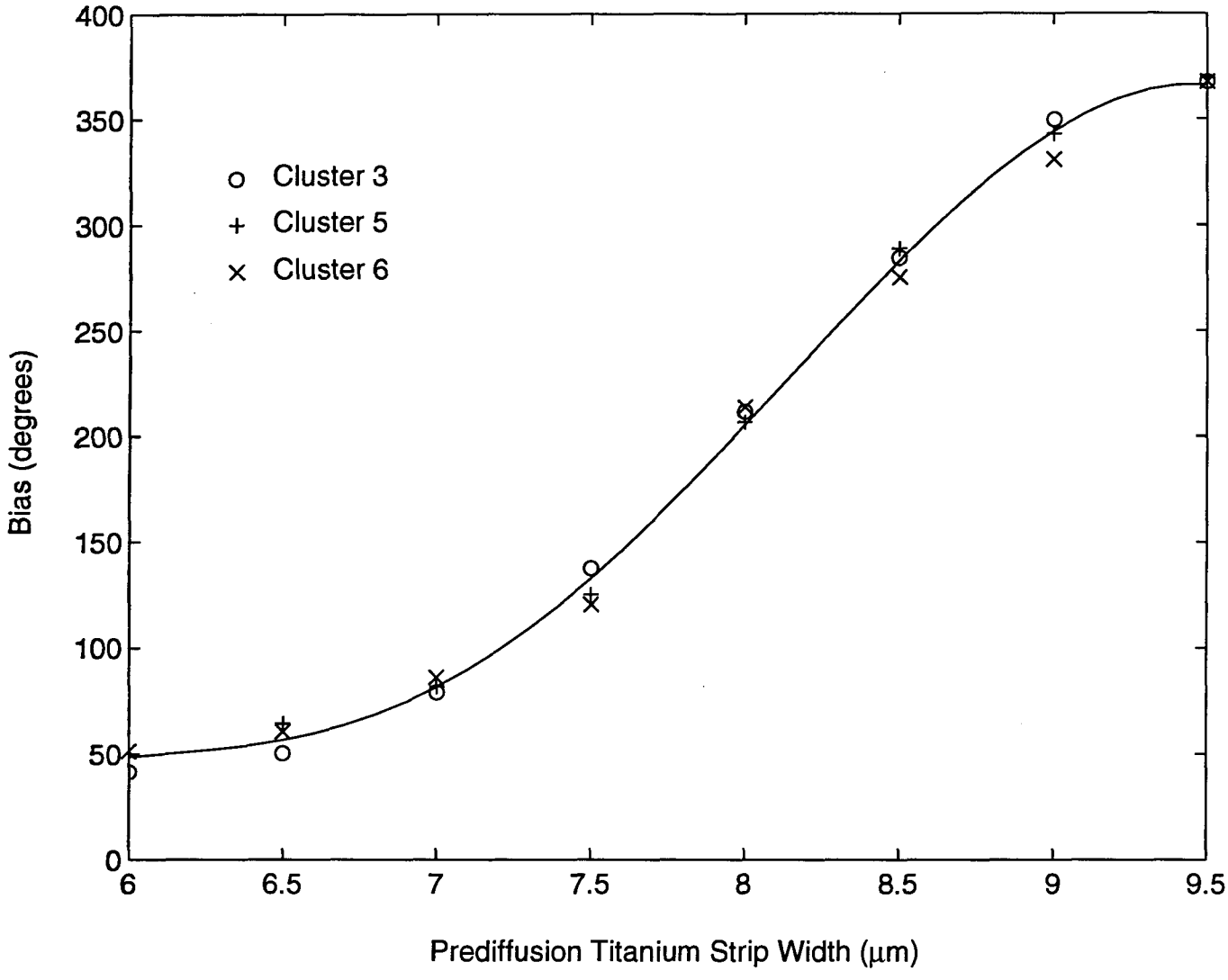

Figure 4.9. The biases of fabricated waveguides as a function prediffusion strip width.

The other effect of prediffusion strip width is on the bias of the device. As we will show in the next chapter the intrinsic phase of the device is proportional to the third power of the modal depth size which, in turn, is a function of prediffusion strip width. Fig. 4.9 shows the intrinsic phase of various single-mode waveguides (29.1 mm long) located in different clusters on a single piece of lithium niobate as a function of their prediffusion strip widths.

The dependence of bias on prediffusion strip width may be used as an advantage with regard to the mass production of IOPCs; several waveguides having prediffusion strip widths ranging from 8 to 9 μm at 0.1 μm steps, may be constructed on a piece of lithium niobate. If the device is cut to a particular length, because of the distribution of intrinsic phases, there is a good chance of finding a waveguide having a bias very close to 90°, which may be accurately adjusted by further polishing.

§ 4.4 The Effect of the Waveguide Length on the Intrinsic Phase

As explained above, one way to achieve a desired bias is to adjust the length of waveguides. In chapter 2, the fact that the slight difference between the propagation constants of TE- and TM-like modes, $\Delta\beta=\beta_{TE}-\beta_{TM}$, produces a phase shift, ϕ_i, between the propagating modes which is linearly dependent on the device length, $\phi_i=\Delta\beta\times L$, was discussed.

To assess the validity of the linearity assumption and also to measure $\Delta\beta$, a sample 29.1 mm long was cut back to form shorter devices, for which the biases were also measured. Figure 4.10 shows the measured biases at different lengths for four devices having various strip widths, ranging from 8.0 to 9.5 μm. The measured data points show less than a few percent deviation from the least-square fitted lines, which is accurate enough to justify the linearity assumption.

Another important factor, which may be extracted from Fig. 4.10, is the minimum length of the device necessary to produce an intrinsic phase difference of $\pi/2$, $L_{\pi/2}$. Since the slopes of the fitted lines in Fig 4.10 are $\Delta\beta$'s for waveguides having different strip widths, $L_{\pi/2}$

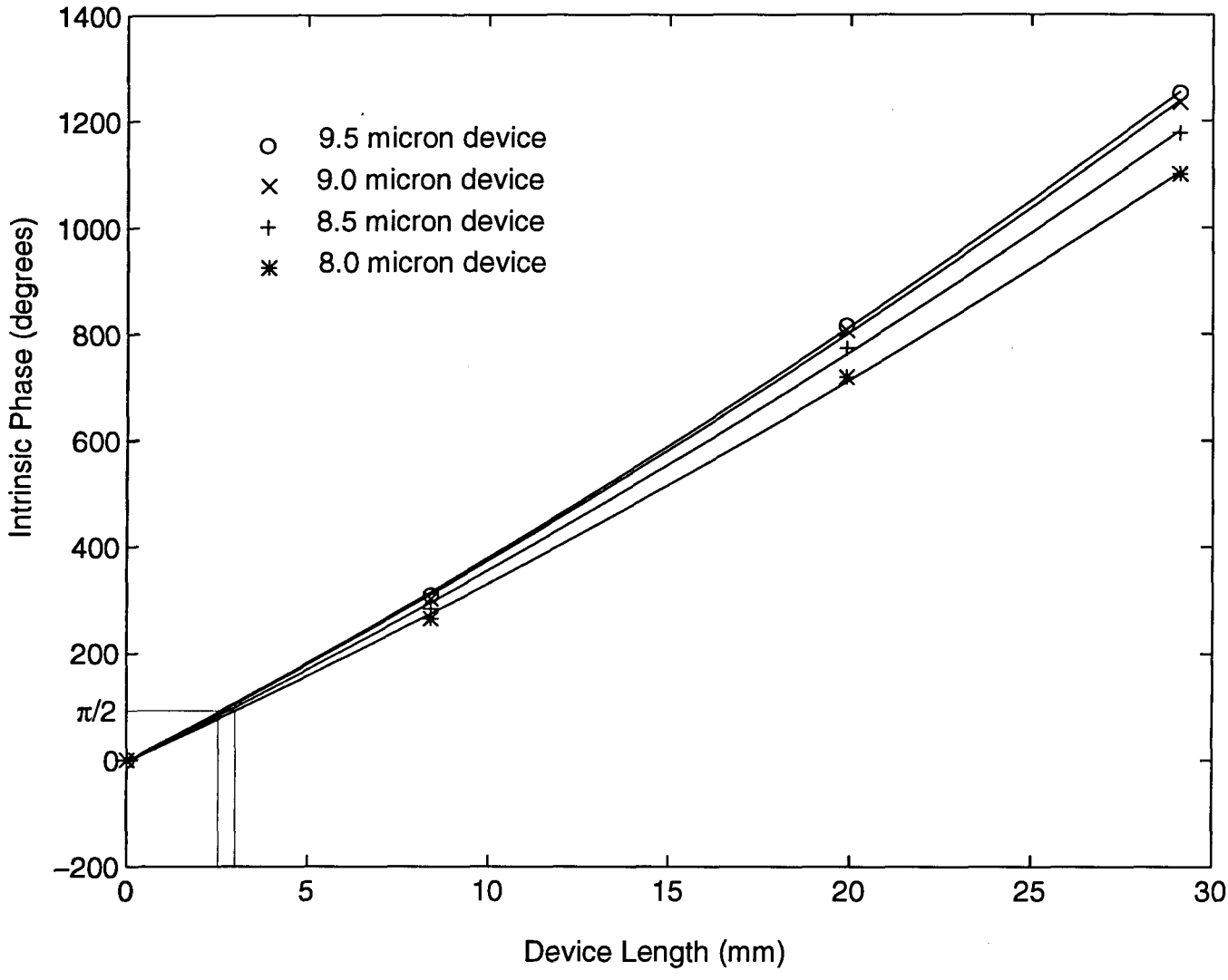

Figure 4.10. The biases of fabricated waveguides as functions of device length.

can easily be calculated for each waveguide from $L_{\pi/2}=\pi/2\Delta\beta$. Figure 4.10 shows that for the fabrication conditions given in chapter 3 and a titanium prediffusion thickness of 770 °A the typical value for $L_{\pi/2}$ is around 2.5 to 3 mm. In the next chapter we introduce an analytical method for calculating $\Delta\beta$ and compare our calculated values to the experimental results extracted from plots like Fig. 4.10.

§ 4.5 Voltage Measurement and Noise

In order that the IOPC should be considered as a plausible alternative to conventional potential transformers, for high-voltage measurements, its performance should be at least as good as that of the current technology. The set of requirements for optical sensors gathered by Erickson [49] were used as our goals throughout the experiments. These requirements may be summarized as follows: for metering purposes over a frequency range of 40Hz to 4KHz an error of less than 0.3% is tolerated for a dynamic range of 1 pu (per unit), for protection a bandwidth of 0.1 Hz to 30 KHz along with an accuracy of 2 to 6% for a dynamic range of 2.2 pu is required, and for fault location an accuracy of 6 to 8% for frequencies above 30 KHz and a dynamic range of 2.4 pu.

A fully integrated system was used for voltage measurements. The final set up had the following specifications: bias = 89°, V_π = 498 volts, on/off ratio = 663:1, device length = 28.5 mm, and optical power received by each detector = 92 μW.

At first, in order to test the effect of the normalization process on optical power fluctuations, the following experiment was performed. After selecting a waveguide, the laser light was coupled to the waveguide through the input fibre which was glued to the device; the output fibre, using a micro positioner, was precisely aligned with the waveguide, but it was not glued into position. Mechanical vibrations, applied to the optical bench, could easily disturb the alignment between the output fibre and waveguide, and produce significant variations in the amount of light coupled to the fibre. The upper trace in Figure 4.11 shows the amount of optical power received by one of the photodetectors, and the lower trace shows the normalized reading from the same detector, which is independent of optical power

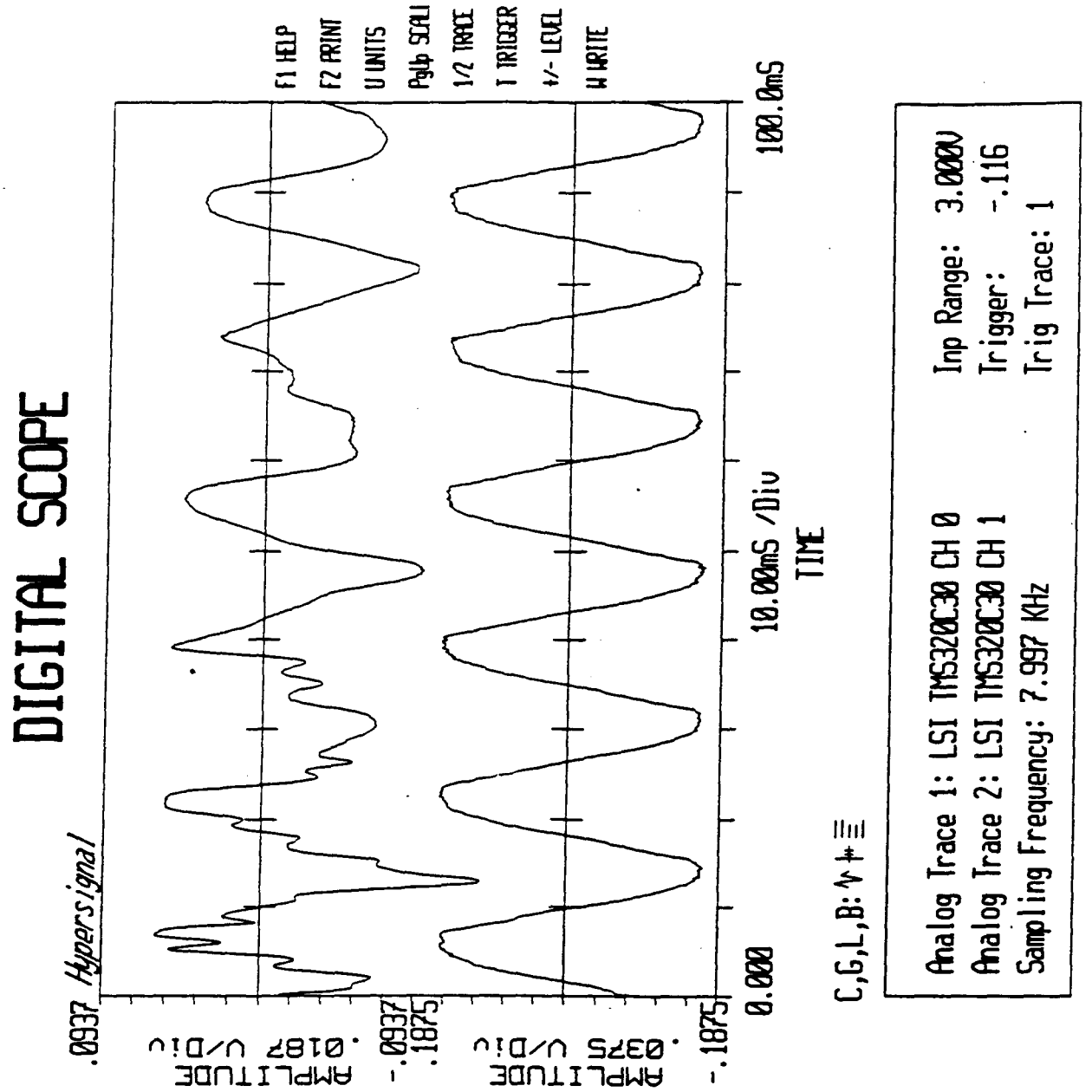

Figure 4.11. The effect of the normalization process in cancelling optical power variations: photodetector output, upper trace; normalized output, lower trace.

variations and accurately follows the applied electric field. The normalization process was capable of recovering the original signal even for power variations of more than 1000:1.

Figure 4.12 shows the RMS values measured by the sensor versus the RMS values of the applied signal. The solid line is a least square fit to the data points. The RMS deviation of the data points from the straight line is 0.95%. This deviation is mainly produced by the device nonlinearity and noise. By limiting the range of measurements to 18 volts, in order to reduce the errors introduced by the linearity assumption, the RMS deviation decreases to a value of 0.22% which meets the Erickson's standard of 0.3% error. Throughout the experiment, in order to reduce the effect of noise on the accuracy of our measurements, a bandpass filter with a bandwidth of 40 Hz to 4 KHz was used.

Figure 4.13 shows the instantaneous voltage measurement for a periodic signal. During the measurements, the output of the photodetector was band-passed filtered from 40 Hz to 4 KHz. In instantaneous voltage measurement the quantization error produced by the digital oscilloscope has a significant effect on the accuracy of the measurements. Through digital filtering of the sampled data points, it is possible to reduce the effect of quantization error considerably. A low pass filter having a cut-off frequency close to 5 KHz was implemented on a computer by averaging over a window of 9 samples; the window was slid over the whole range of sampled data points. Figures 4.13 (a) and (b) show the results of measurements before and after digital filtering, respectively. For figure 4.13 (a) the RMS deviation of the measured voltages from the straight line was 0.98% (compared to the maximum value), while, after digital filtering, this value dropped to 0.5%, which is close to the required value of 0.3%.

There are three different sources which contribute to the overall noise: the laser noise, the photodetector noise, and the noise produced by the device itself. Since the optical power

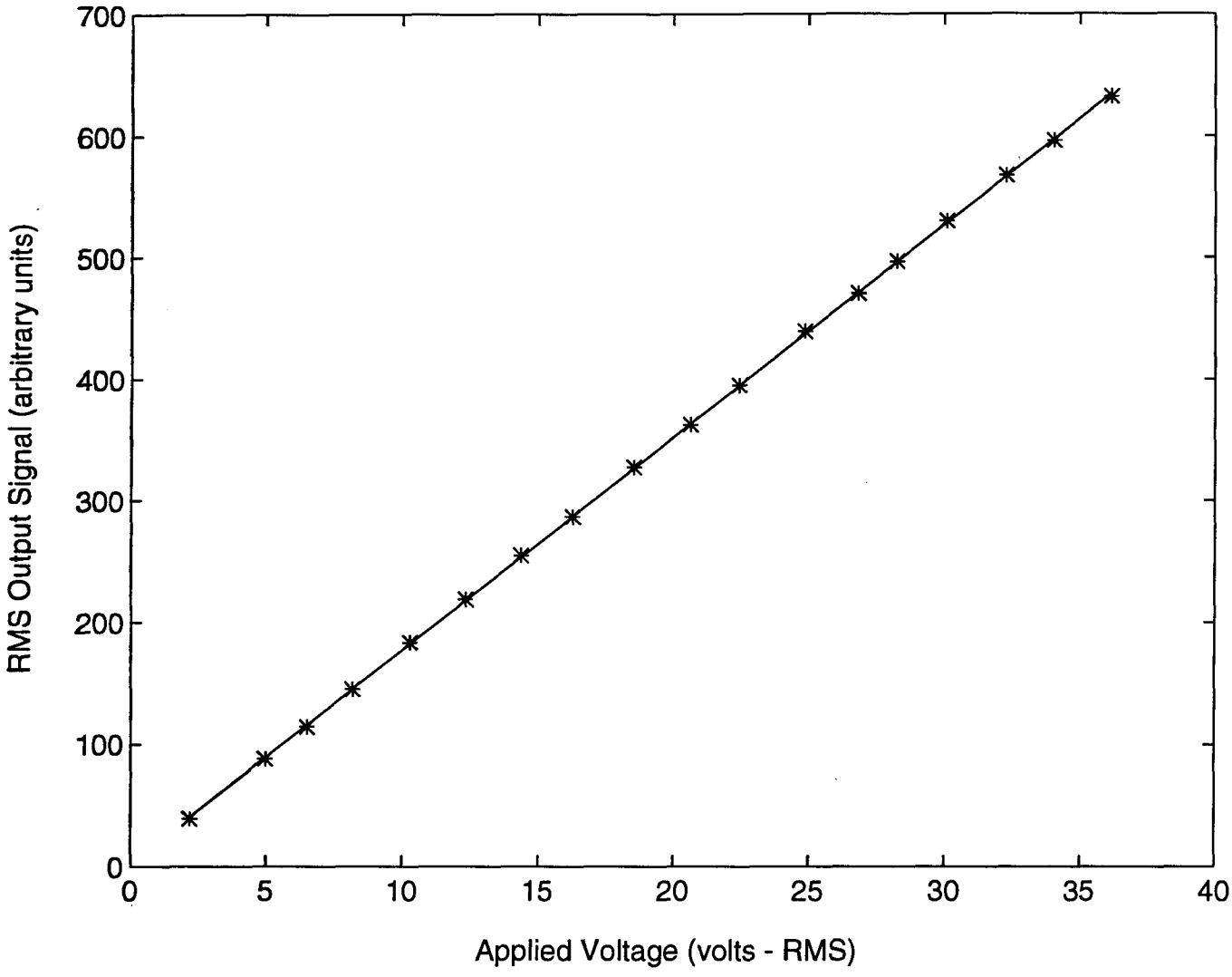

Figure 4.12. A sensor's RMS output as a function of the RMS value of the applied signal.

received by the detectors is more than 50 μW, the signal to noise ratio of the measurements is at least better than 30 dB, which means that the error introduced by the photodetector noise is less than 0.1%. The device noise is mainly produced by the photorefractive effect (known as "optical damage") in lithium niobate [50]. The extent of the optical damage is a function of wavelength and optical power of the light. For a wavelength of 0.633 μm the

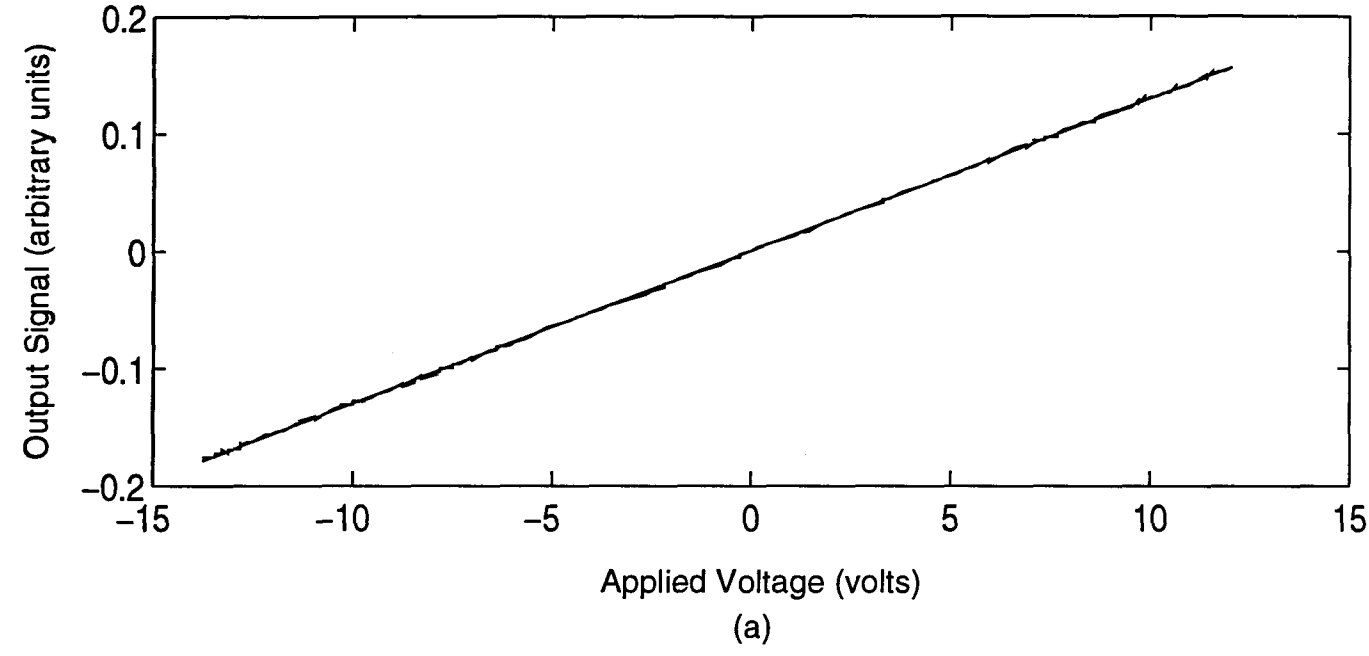

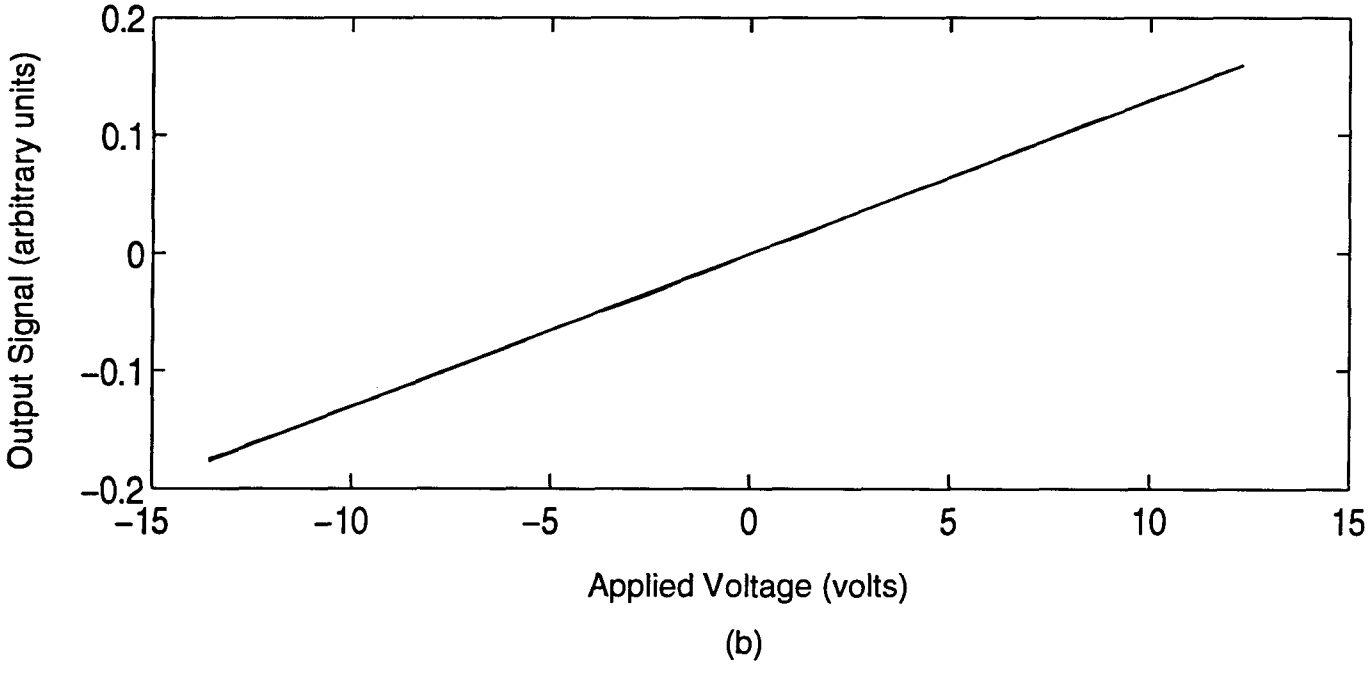

Figure 4.13. Instantaneous voltage measurement a) before digital filtering b) after digital filtering.

optical power should be limited to a few μW, while at λ_o=1.3 μm the optical power may be increased up to 20 mW [51]. Since, for our devices, the optical power coupled to the waveguides hardly exceeds 1 mW, the effect of optical damage on device performance is insignificant. Also, since the noise produced through the above sources is distributed over a wide frequency range, it can be reduced considerably by appropriate filtering.

§ 4.6 Temperature Dependence

One of the major considerations, with regard to IOPC performance, is preserving the accuracy of the measurements over a wide range of temperatures.

Temperature fluctuations, through changing the refractive index of lithium niobate along the different axes of the crystal, cause the bias of the IOPC to drift. For a z-propagating device this amount of bias displacement is expected to be quite limited because the refractive index of the crystal along both x and y axes is the ordinary refractive index, which it is reasonable to assume has the same temperature behavior in both directions.

In order to study the temperature dependence of the bias, the device was mounted on an electrical heating stage; the temperature of the stage was increased in steps of about 15 °C up to 70 °C; every step was carried out in 30 minutes so that the device had enough time to reach a stable mechanical and thermal state. Figures 4.14 (a,b,c) show the measured bias, for various waveguides having different strip widths, versus the temperature. The asterisks indicate the measured bias and the solid lines are the least square fits to the data points. The steepest slope was 0.2°/°C; since the device was 28.5 mm long, the greatest change of bias per unit temperature per unit length was 0.007°/°C/mm. Obviously this amount of

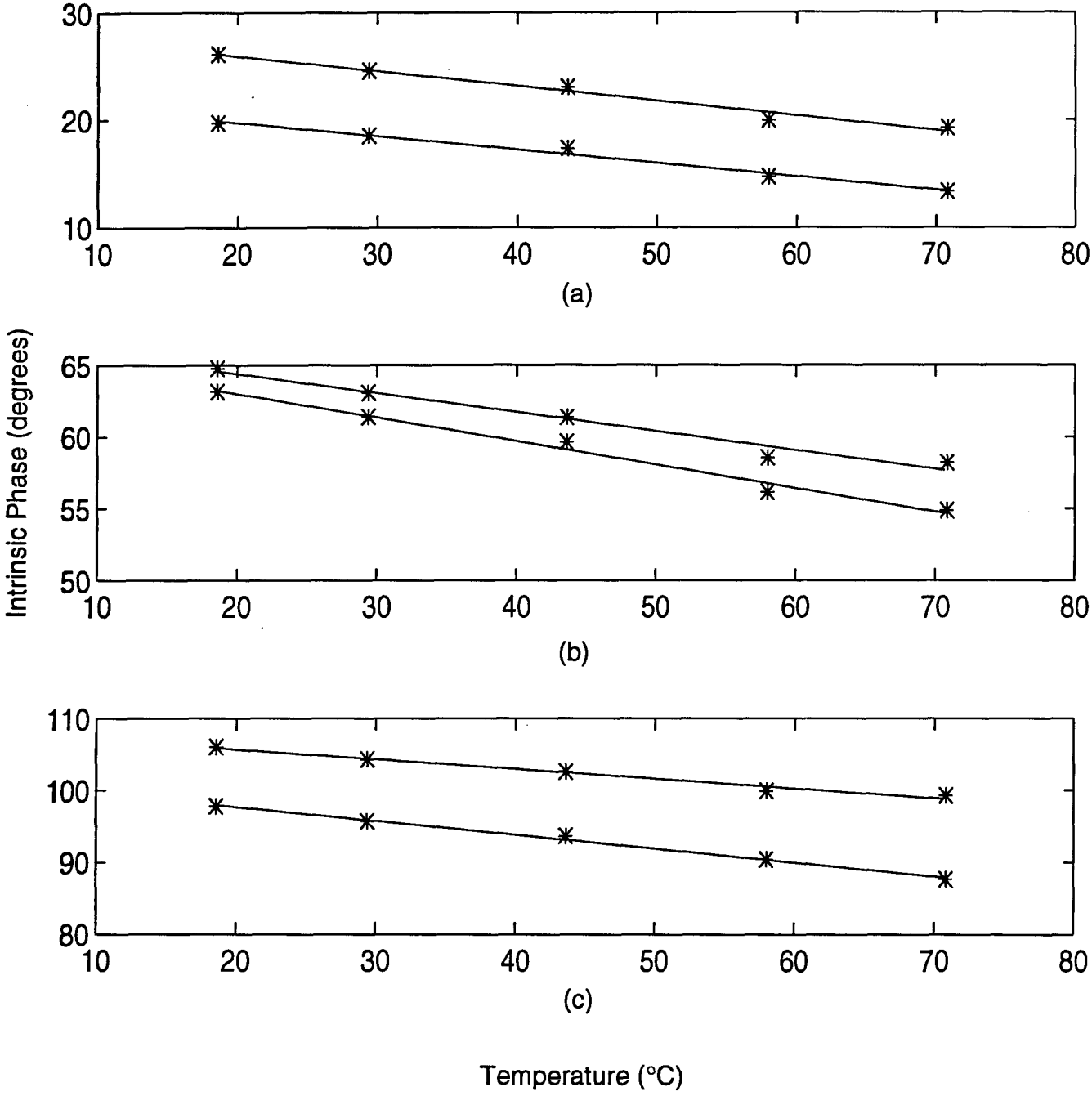

Figure 4.14. Temperature dependence of the bias for a) 8.5–micron devices b) 9–micron devices c) 9.5–micron devices.

bias change can be accounted for by data processing methods. By rewriting equation 4.1

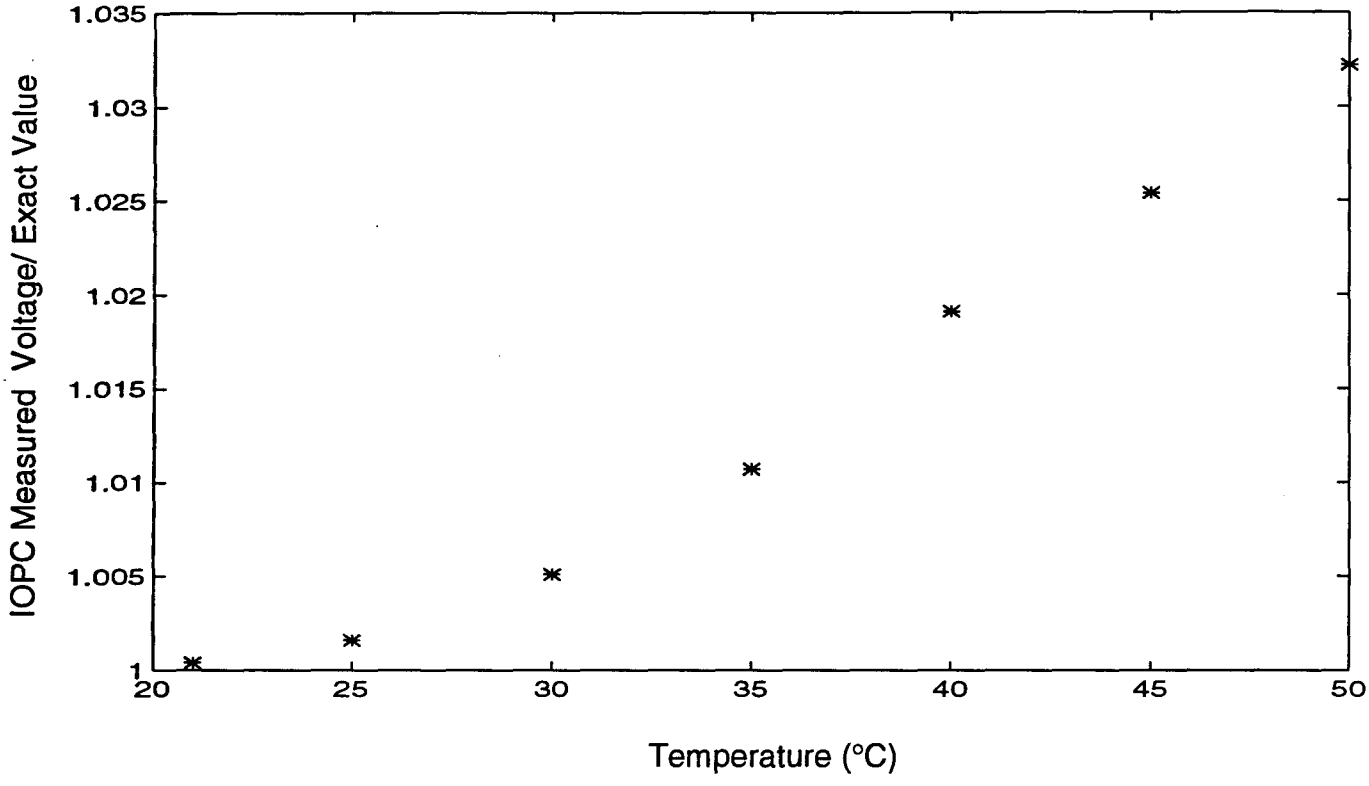

Figure 4.15. Normalized measured voltage versus temperature.

in the following form

$$\phi_i + \pi \frac{E_y}{E_\pi} = Arccos\left(\frac{2S-1}{\alpha}\right), \tag{4.7}$$

and since E_y has a periodic nature, ϕ_i appears as the dc (or very low frequency) component of the quantity $Arccos\left(\frac{2S-1}{\alpha}\right)$, which can be easily separated and measured regardless of its dependence on temperature.

Figure 4.15 shows the results of the temperature tests, where the measured voltages are divided by their exact values. The values of α and E_π are measured at 25 °C and then used for other temperatures. A maximum error of 3.2% occurred at 50 °C. The assumption that E_π is a constant over the whole temperature range (i.e., assuming that $n_o^3 r_{22}$ is independent of temperature) should be considered as the most probable source of the error. A simple

way to compensate for the above assumption is, as a calibration process, to measure E_π and ϕ_i at various temperatures and store the ϕ_i-E_π pairs in a computer; then the measurement of ϕ_i could provides us with the appropriate value of E_π for a particular temperature.

§ 4.7 Piezoelectric Resonances

Lithium niobate is a piezoelectric crystal which belongs to the point group 3m, having the piezoelectric coefficient matrix [16]

$$d_{ij} = \begin{bmatrix} 0 & 0 & 0 & 0 & d_{15} & d_{16} \\ d_{21} & d_{22} & 0 & d_{24} & 0 & 0 \\ d_{31} & d_{32} & d_{33} & 0 & 0 & 0 \end{bmatrix}, \tag{4.8}$$

where $d_{15} = d_{24}$, $d_{16} = -2d_{22}$, $d_{21} = -d_{22}$, and $d_{31} = d_{32}$. Since the applied electric field is in the y direction, it produces longitudinal strains along the x and y directions and shear strain in the y-z plane through the piezoelectric coefficients d_{21}, d_{22}, and d_{24}, respectively. If the frequency of the applied electric field matches one of the permitted acoustic resonance frequencies, the crystal will resonate. The frequency of such a resonance is calculated as $f_n = \frac{nv_s}{2d}$, where d may be any one of the 3 dimensions of the crystal (i.e., the width, length, or thickness), f_n is the nth permitted resonance frequency, and v_s is the speed of sound in lithium niobate.

Figures 4.16 and 4.17 show the inverse of piezoelectric resonance frequencies, $\frac{1}{f_n}$, as functions of the crystals' width and length, respectively. The solid lines are least square fits to the measured data points. The speed of sound in lithium niobate, in the x direction, can be calculated from the slope of the solid line in Fig. 4.16. The value obtained is 6499 m/s which is close enough to the reported value of 6572 m/s [22], for the x direction.

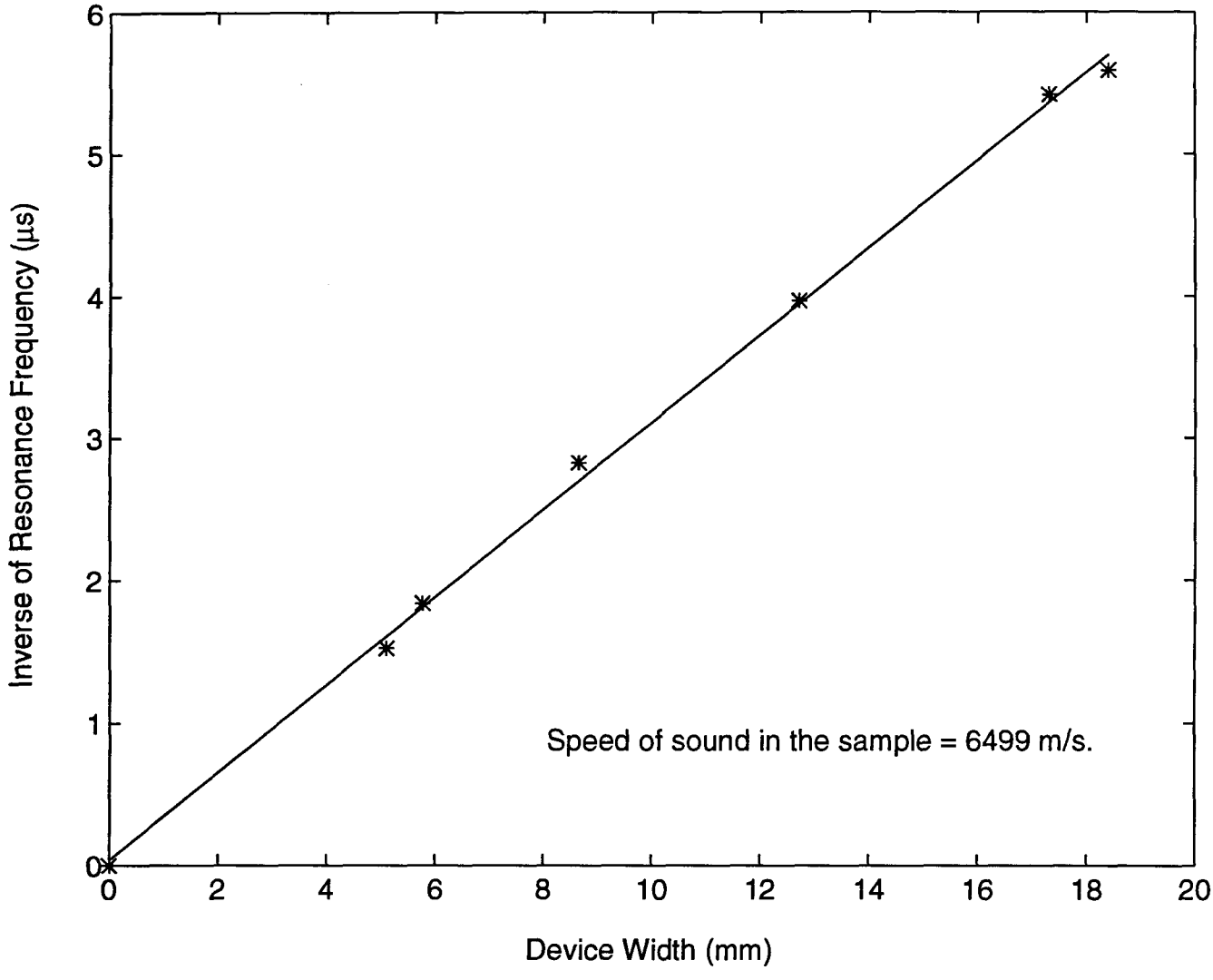

Figure 4.16. Inverse of piezoelectric resonance frequency as a function of device width.

Since the piezoelectric resonances affect the amount of light coupled into the waveguide and also, disturb the polarization state of the light passing through the electooptic medium, they practically limit the useful bandwidth of the sensor. The resonance frequencies are inversely proportional to the dimensions of the device; therefore, it is possible to shift longitudinal resonance frequencies along the x and y directions to higher frequencies by

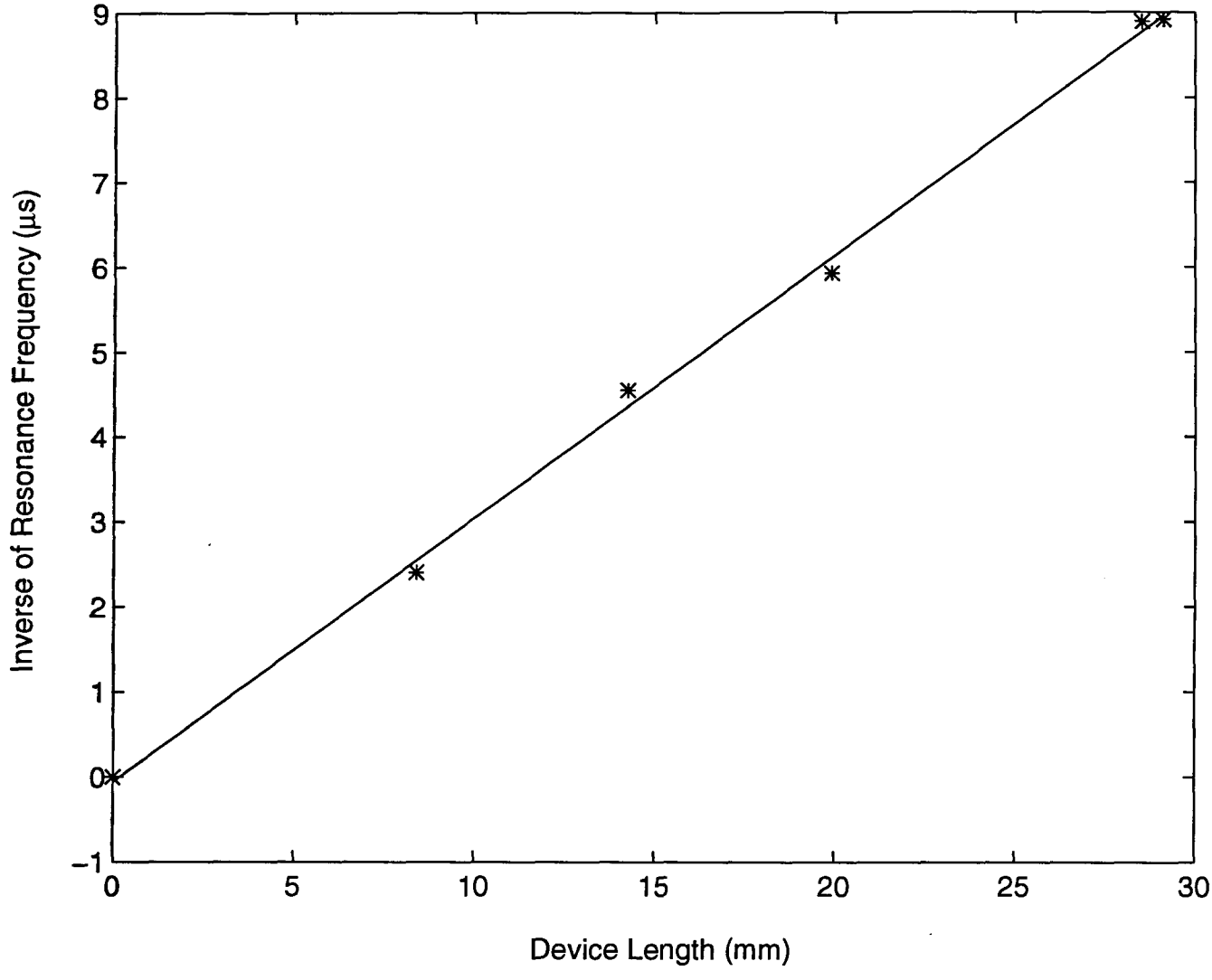

Figure 4.17. Inverse of piezoelectric resonance frequency as a function of device length.

making the device narrower and thinner, respectively. For example, for a device 0.5 mm wide the first longitudinal resonance along x happens when $f_1 = \frac{v_s}{2w} = \frac{6572}{2\times 0.5\times 10^{-3}} = 6.57$ MHz, which is at a high enough frequency to conduct the impulse measurements discussed in the next section. However, since both the bias and V_π depend on the device length, it is not possible to make the device shorter than a few millimeters; our experiments for

lightning impulse measurements show that the shear resonance in the y-z plane, which has a component along the length of the device (i.e., z direction), has a negligible effect on the optical output and, therefore has no limiting effect on the device bandwidth; it is the first longitudinal resonance along the device width that plays the major role in this regard.

§ 4.8 Impulse Measurements

Since the IOPC has the capability of measuring any arbitrary applied electric field, E_y, (i.e., not necessarily a periodic one), it may used as a sensor to measure lightning impulses or to monitor high-voltage switching.

A switching impulse is defined in the following way [52]. The front time, T_f, of the rising edge of the impulse is

$$T_f = 1.67(T_{90} - T_{30}), \tag{4.9}$$

where T_{90} and T_{30} are the instants that the rising edge of the pulse reaches 90% and 30% of the maximum value of the pulse, respectively. The tail time, T_t, is the period of time that the falling tail of pulse takes to drop from its maximum to 50% of the maximum, i.e.,

$$T_t = T_{max} - T_{max/2}. \tag{4.10}$$

Typical values for the standard front and tail times are 250 μs and 3000 μs, respectively.

The lightning impulse as defined by the IEC (International Electrotechnical Commission) has a front time of 1.2 μs with ±30% tolerance and a tail time of 50 μs (± 20%).

In order that the IOPC be able to measure the above signals successfully, the bandwidth of the sensor should be wide enough to follow the fastest rising edge accurately, and none of its

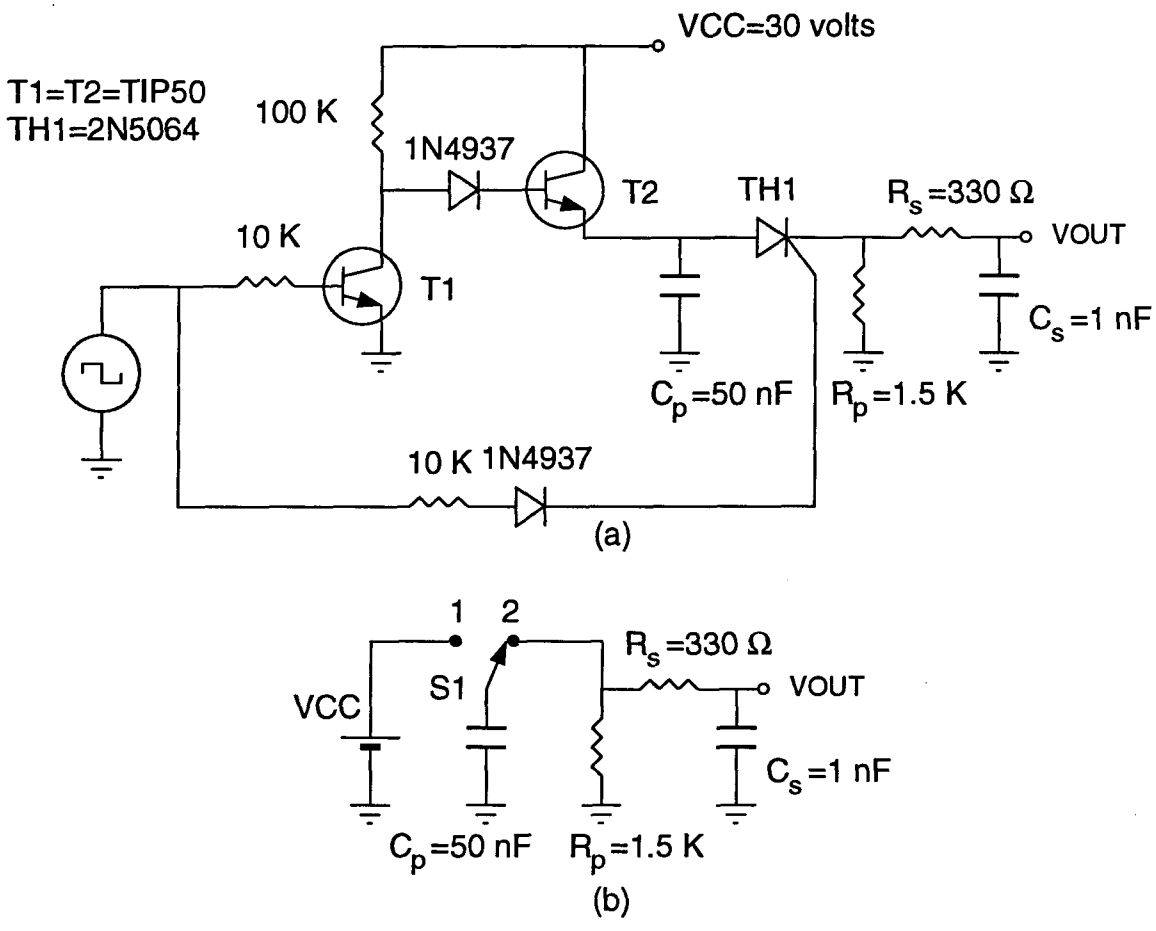

Figure 4.18. Impulse generator circuit a) electronic circuit b) simplified circuit.

piezoelectric resonances should be allowed to be excited and interfere with the measurement process.

To produce and apply the impulses described above, the electronic circuit shown in Fig. 4.18(a) was designed. The thyristor and the electronic part mainly emulate the job of the switch S1 shown in Fig. 4.18(b); during the periods that the trigger square wave is low, the thyristor TH1 is off and the capacitor C_p is charged through the transistor T2 to about V_{cc}, which is similar to the performance of switch S1 at position 1 (see Fig. 4.18(b)); when the rising edge of the square wave appears, the transistor T2 goes off and thyristor TH1 turns on and performs like the switch S1 at position 2.

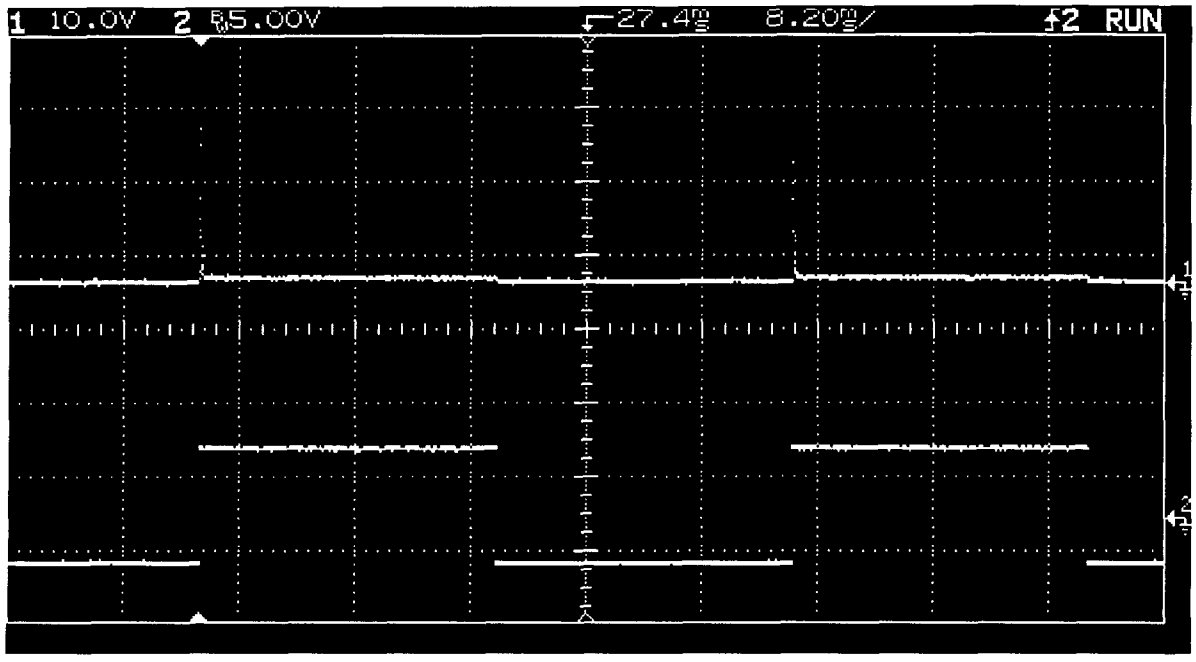

Figure 4.19. Generated impulses, upper trace, and the switching signal, lower trace.

When S1 switches to position 2 the voltage of the charged capacitor C_p appears at the output. The rise time of the output voltage is determined primarily by $\tau_s = R_s C_s$. At the same time C_p begins to discharge through R_p, which forms the falling edge of the impulse. The tail time of the impulse mainly depends upon $\tau_p = R_p C_p$. A SPICE simulation of the circuit shows that for C_p=50 nF, R_p=1.5 kΩ, R_s=330 Ω, C_s=1 nF, and a load capacitor, C_L, equal to 0.2 nF (to account for the capacitance of the sensor), the front time of the output pulse is 1.17 μs and the tail time is 53 μs (for V_{cc}=30 volts). Fig. 4.19 shows the generated impulses synchronized with the rising edges of the trigger square-wave signal.

In figures 4.20 and 4.21 the upper trace is the applied impulse and the lower trace is the response of an unclamped device which is 29.1 mm long and 18.4 mm wide. Figure 4.20 shows that, although the sensor has a bandwidth making it capable of following the rising edge of the pulse, the piezoelectric resonances interfere with the measurement and practically limit the useful bandwidth of the device. The frequency of the ripples shows that

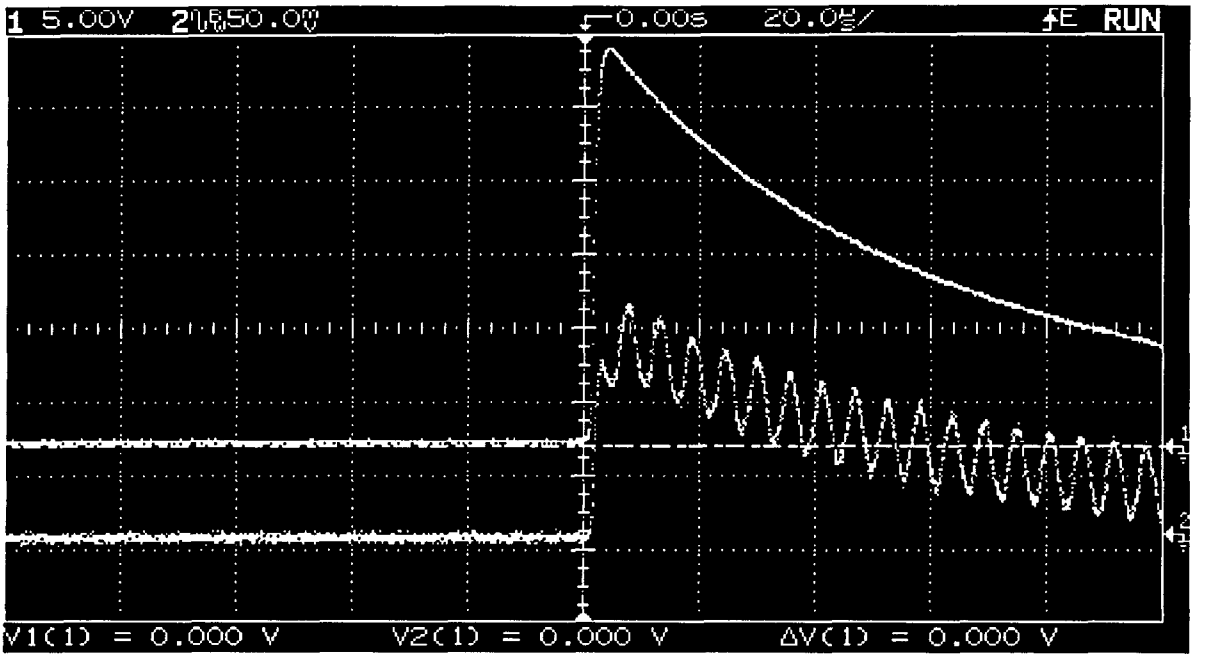

Figure 4.20. Applied impulse, upper trace, and the response of an unclamped device 18.4 mm wide, lower trace.

only the first longitudinal piezoelectric resonance along the x direction (device width) has a significant effect on the device output and the effect of shear resonances along the device length is negligible. Figure 4.21 shows the piezoelectric vibrations excited by the applied electrical impulse for an unclamped device over a period of 5 ms.

Two methods may be used to reduce the above effect. First, one can use a notch filter to suppress the piezoelectric resonance frequency which may be implemented by electronic circuitry or DSP filtering. Second, since the frequency of the ripples is inversely proportional to the crystal width, it is possible to shift the piezoelectric resonance to higher frequencies by cutting the device into narrower strips. Since the power spectrum of the applied impulse contains less power at higher frequencies, it is expected that for narrower devices the amplitude of piezoelectric oscillations will be smaller and, obviously, the frequency of the oscillations is higher.

To test the second method, the device was cut so as to be only 5.1 mm wide; figures 4.22 and 4.23 show a significant improvement in the response of the device to an applied impulse having a front time of 1.67 μs and a tail time of 45.8 μs. Since the actual width of the waveguide is on the order of 10^1 micrometers, it is possible to make the device as narrow as necessary to gain an appropriate response.

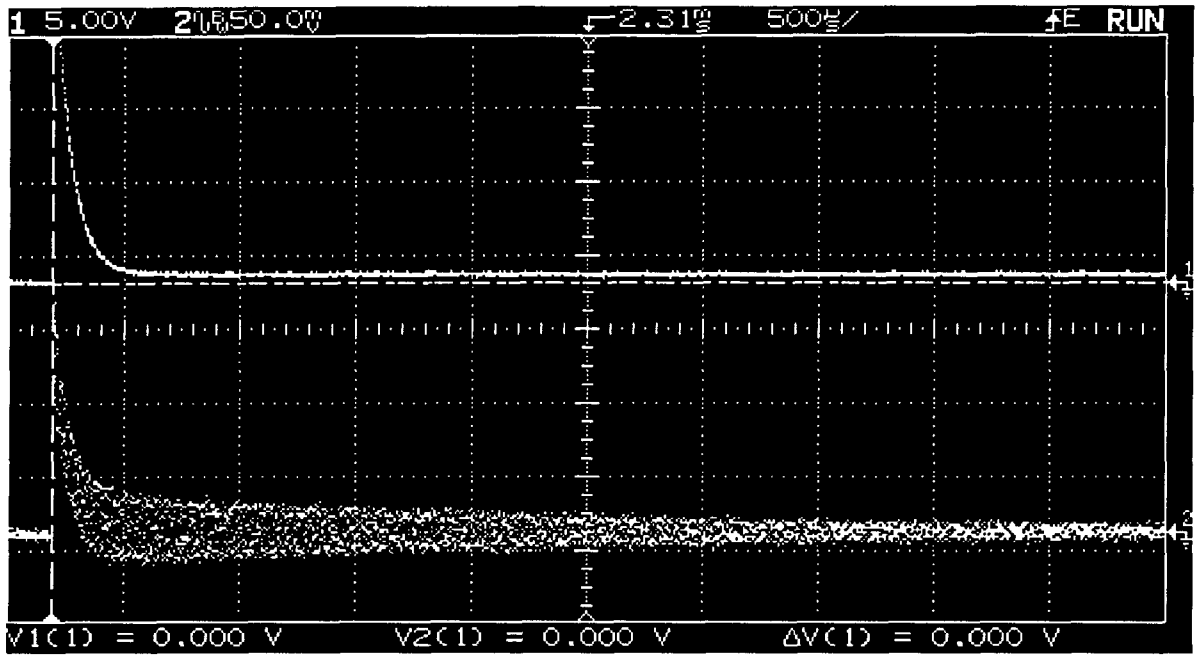

Figure 4.21. The impulse response of the device of Fig. 4.20 over a 5 ms time period (upper trace: applied impulse, lower trace: device response).

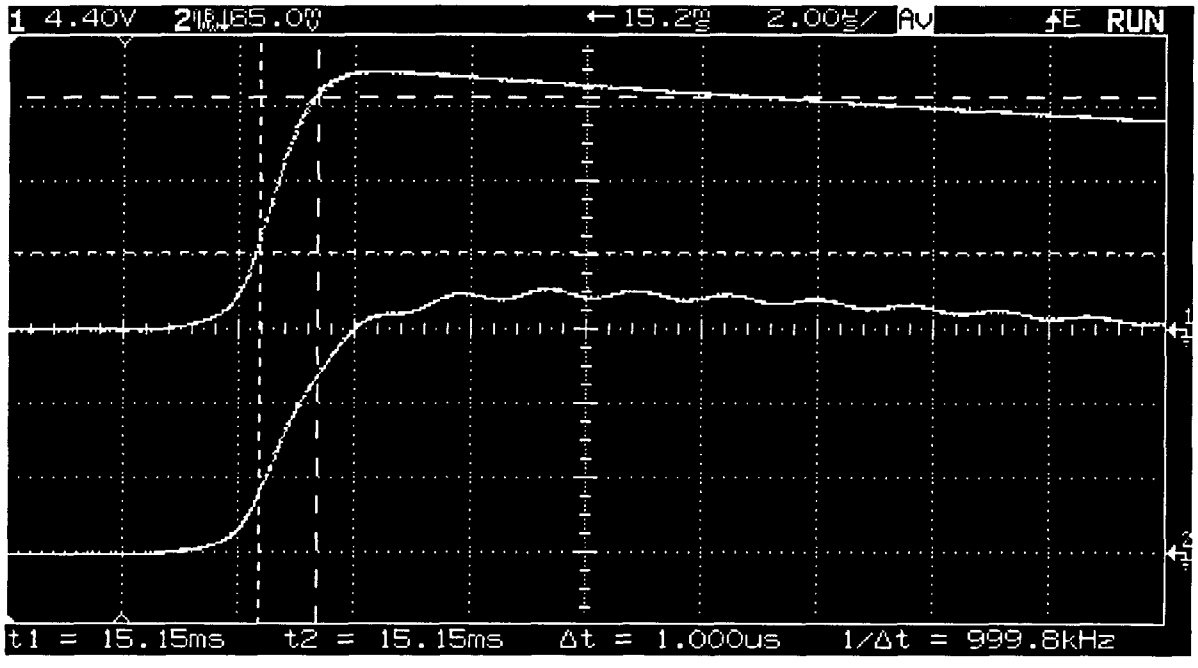

Figure 4.22. Impulse response of an unclamped device 5.1 mm wide, T_f=*1.67* μs (upper trace: applied impulse, lower trace: device response).

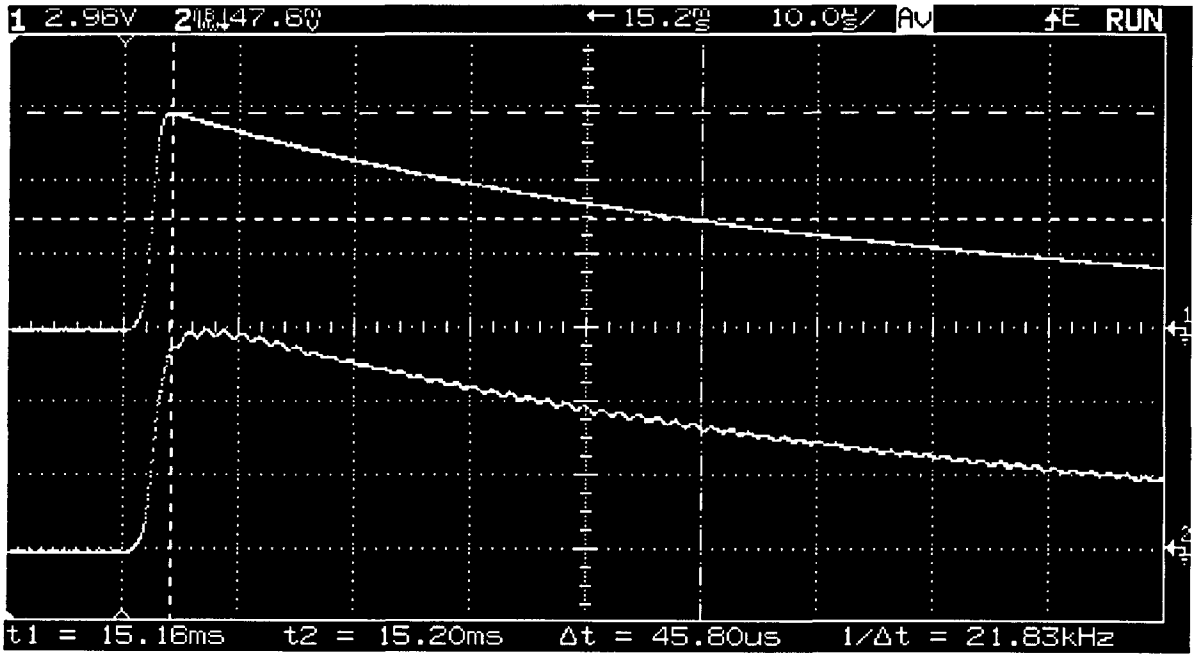

Figure 4.23. Impulse response of an unclamped device 5.1 mm wide, T_t=*45.8* μs (upper trace: applied impulse, lower trace: device response).

Chapter 5: Calculation of $\Delta\beta = \beta_{\mathrm{TE}} - \beta_{\mathrm{TM}}$ in z-propagating $\mathrm{Ti} : \mathrm{LiNbO_3}$ Channel Waveguides

§ 5.1 Introduction

As discussed previously, the intrinsic difference between the propagation constants of the fundamental TE- and TM-like modes, β_{TE} and β_{TM}, respectively, in an isotropic diffused waveguide can be used to set the polarization of the output to a particular state, or "bias". The calculation of the intrinsic difference between the propagation constants, $\Delta\beta = \beta_{TE} - \beta_{TM}$, is generally desirable for the IOPC and other polarization controllers [53,54] using z-propagating $Ti : LiNbO_3$ waveguides.

As has been discussed, in a z-propagating $Ti : LiNbO_3$ waveguide, in an x- or y-cut substrate, β_{TE} and β_{TM} are very nearly the same; the slight difference between them coming about, primarily, from the different boundary conditions that prevail at substrate-superstrate interface. Our measurements show that in an isotropic channel waveguide, the difference between β_{TE} and β_{TM} is usually in the 5th or 6th significant figure. Therefore, to calculate $\Delta\beta$, β_{TE} and β_{TM} have to be calculated with 6 or 7 significant figures. Since computational errors and other approximations make this accuracy very hard to achieve, an analytical method for directly calculating $\Delta\beta$ is desired.

Experiments show that the optical field distributions for typical diffused waveguides in lithium niobate are well approximated by Hermite-Gaussian functions [55]. Therefore, these functions are used here. The integral expressions for β^2 together with the proper boundary conditions for the TE- and TM-like modes, are used to derive an approximate expression for

$\Delta\beta$. To test the accuracy of this expression, it is applied to slab waveguides with various film thicknesses, and the results are compared with the $\Delta\beta$'s that are calculated exactly for these structures. Also, to test the appropriateness of using the derived equation for the z-propagating $Ti : LiNbO_3$ channel waveguides, a number of waveguides with various prediffusion strip widths were fabricated, the analytical expression for $\Delta\beta$ was rearranged to give the fundamental mode sizes in the depth direction as functions of $\Delta\beta$, the experimentally measured $\Delta\beta$'s for the fabricated waveguides were substituted into the expression to find the fundamental mode sizes, and the mode sizes thus obtained are compared with the values obtained using the variational method [26].

§ 5.2 Method of Analysis

The scalar-wave equation for the transverse electric field in a loss-less, length-invariant, weakly guiding waveguide can be written as

$$\nabla_t^2 E(x,y) + \left[n^2(x,y)k_0^2 - \beta^2\right] E(x,y) = 0, \tag{5.1}$$

which, in turn, can be written in the integral form

$$\int_{-\infty}^{\infty}\int_{-\infty}^{\infty} \left\{ |\nabla_t E(x,y)|^2 + \left[\beta^2 - n^2(x,y)k_0^2\right] |E(x,y)|^2 \right\} dxdy = 0. \tag{5.2}$$

The TE- and TM-like modes have different optical field distributions, here we use E_{TE} and E_{TM}, respectively. However, given the nature of z-propagating $Ti : LiNbO_3$ waveguides, we make the following simplifying assumptions:

i) the optical field distribution in the transverse plane, for each mode, may be treated as a separable function [48], i.e., $E(x,y) \simeq A\psi(x)\phi(y)$, where $\psi(x)$ and $\phi(y)$ are normalized

functions and A is a constant, and

ii) because the substrate-superstrate interface lies in a plane normal to the x axis, it is reasonable to assume that the different boundary conditions for the TE- and TM-like modes at the interface, $x = 0$, only affect the field distribution in the x direction and, therefore, the field profiles in the y direction for both the TE- and TM-like modes are nearly identical and can be approximated by $\phi(y)$, i.e., $\phi_{TM}(y) \simeq \phi_{TE}(y) \triangleq \phi(y)$, giving

$$E_{TE} = A\psi_{TE}(x)\phi(y) \quad \text{and} \quad E_{TM} = B\psi_{TM}(x)\phi(y). \tag{5.3}$$

Equation 5.2 for each mode reduces to

$$\int_{-\infty}^{\infty} \left\{ \left| \frac{\partial \psi_{TE,TM}(x)}{\partial x} \right|^2 + \left[\beta_{TE,TM}^2 - n_{eff}^2(x) k_0^2 \right] \left| \psi_{TE,TM}(x) \right|^2 \right\} dx = 0, \tag{5.4}$$

where

$$n_{eff}^2(x) = \frac{\int_{-\infty}^{\infty} \left\{ n^2(x,y)|\phi(y)|^2 - |\partial\phi(y)/\partial y|^2 / k_0^2 \right\} dy}{\int_{-\infty}^{\infty} |\phi(y)|^2 dy}. \tag{5.5}$$

Rearranging 5.4, one obtains

$$\beta_{TE,TM}^2 = \frac{k_0^2 \int_{-\infty}^{\infty} n_{eff}^2(x) \left| \psi_{TE,TM} \right|^2 dx - \int_{-\infty}^{\infty} \left| \frac{\partial \psi_{TE,TM}}{\partial x} \right|^2 dx}{\int_{-\infty}^{\infty} \left| \psi_{TE,TM} \right|^2 dx} \tag{5.6}$$

or, by substituting $\int_{-\infty}^{\infty} \left| \psi_{TE,TM} \right|^2 dx = 1$ and $\beta_{TM}^2 - \beta_{TE}^2 \simeq 2\beta\Delta\beta$ into equ. 5.6,

$$2\beta\Delta\beta = k_0^2 \int_{-\infty}^{\infty} n_{eff}^2(x) \left(|\psi_{TM}|^2 - |\psi_{TE}|^2 \right) dx - \int_{-\infty}^{\infty} \left(\left| \frac{\partial \psi_{TM}}{\partial x} \right|^2 - \left| \frac{\partial \psi_{TE}}{\partial x} \right|^2 \right) dx, \tag{5.7}$$

where $\beta \triangleq n_b \frac{2\pi}{\lambda_0}$.

The optical field distributions of the fundamental modes of diffused strip waveguides can be approximated by a Gaussian function in the width and a Hermite-Gaussian function in the

depth directions [48]. In the superstrate, or cladding layer, the optical field distribution in the x direction decays exponentially with a decay constant of $\gamma_{TE,TM} = \sqrt{\beta^2_{TE,TM} - k_0^2 n_c^2}$, where n_c is the cladding refractive index and $k_0 = \frac{2\pi}{\lambda_0}$. For cases of practical interest to us, e.g., $Ti : LiNbO_3$ waveguides with air or silicon dioxide cladding layers, n_c is significantly smaller than the bulk refractive index, n_b; also, β_{TE} and β_{TM} are very close to each other and can both be approximated by β; therefore, we can approximate γ_{TE} and γ_{TM} with a γ: $\gamma \triangleq \sqrt{\beta^2 - k_0^2 n_c^2} = k_0\sqrt{n_b^2 - n_c^2}$.

For the optical fields of the TE- and the TM-like modes we use the following

$$\psi_{TE}(x) \triangleq \begin{cases} A_1\left(\frac{x+x_1}{W_x}\right)e^{-\frac{1}{2}\left(\frac{x+x_1}{W_x}\right)^2} & x > 0 \\ B_1 e^{\gamma x} & x < 0 \end{cases} \tag{5.8}$$

$$\psi_{TM}(x) \triangleq \begin{cases} A_2\left(\frac{x+x_2}{W_x}\right)e^{-\frac{1}{2}\left(\frac{x+x_2}{W_x}\right)^2} & x > 0 \\ B_2 e^{\gamma x} & x < 0 \end{cases} \tag{5.9}$$

where, using the boundary conditions, we obtain for the TE-like mode

$$x_1 \approx 1/\gamma \quad , \quad A_1^2 \approx \frac{4}{W_x\sqrt{\pi}} \quad , \quad B_1 \approx \frac{A_1}{W_x\gamma}, \tag{5.10.a, b, c}$$

and for the TM-like mode

$$x_2 \approx (n_c/n_b)^2/\gamma \quad , \quad A_2^2 \approx A_1^2 - \frac{4}{3}\frac{A_1^2}{W_x^3\gamma^3\sqrt{\pi}}\left(1 - \left(\frac{n_c}{n_b}\right)^6\right) \text{ and } B_2 \approx \frac{A_2}{W_x\gamma}. \tag{5.11.a, b, c}$$

Equation 5.7 can be rewritten in the following form

$$\begin{aligned} 2\beta\Delta\beta = k_0^2 \int_{-\infty}^{0} n_{eff}^2(x)\left(|\psi_{TE}|^2 - |\psi_{TM}|^2\right)dx - \int_{-\infty}^{0}\left(\left|\frac{\partial\psi_{TE}}{\partial x}\right|^2 - \left|\frac{\partial\psi_{TM}}{\partial x}\right|^2\right)dx \\ + k_0^2 \int_{0}^{\infty} n_{eff}^2(x)\left(|\psi_{TE}|^2 - |\psi_{TM}|^2\right)dx - \int_{0}^{\infty}\left(\left|\frac{\partial\psi_{TE}}{\partial x}\right|^2 - \left|\frac{\partial\psi_{TM}}{\partial x}\right|^2\right)dx. \end{aligned} \tag{5.12}$$

By substituting $n_{eff}(x) \approx n_c$ for $x < 0$, into the first term on the right hand side of equ. 5.12, one obtains,

$$term1 = k_0^2 \int_{-\infty}^{0} n_{eff}^2(x)\left(|\psi_{TE}|^2 - |\psi_{TM}|^2\right)dx \simeq k_0^2 n_c^2 \int_{-\infty}^{0}\left(|\psi_{TE}|^2 - |\psi_{TM}|^2\right)dx, \tag{5.13}$$

and for the third term, assuming $n_{eff}(x) \approx n_b$ for $x > 0$,

$$term3 = k_0^2 \int_0^\infty n_{eff}^2(x)\Big(|\psi_{TE}|^2 - |\psi_{TM}|^2\Big)dx \simeq k_0^2 n_b^2 \int_0^\infty \Big(|\psi_{TE}|^2 - |\psi_{TM}|^2\Big)dx. \quad (5.14)$$

Because ψ_{TE} and ψ_{TM} are normalized functions, i.e., $\int_0^\infty \psi_{TE,TM}^2 dx = 1 - \int_{-\infty}^0 \psi_{TE,TM}^2 dx$,

$$term3 \simeq -k_0^2 n_b^2 \int_{-\infty}^0 \Big(|\psi_{TE}|^2 - |\psi_{TM}|^2\Big)dx. \quad (5.15)$$

Therefore,

$$term1 + term3 \simeq -\gamma^2 \int_{-\infty}^0 \Big(|\psi_{TE}|^2 - |\psi_{TM}|^2\Big)dx. \quad (5.16)$$

By substituting the trial functions 5.8 and 5.9, i.e., $\psi_{TE,TM} = B_{1,2}e^{\gamma x}$ for $x < 0$, into the second term,

$$term2 = -\int_{-\infty}^0 \left(\left|\frac{\partial\psi_{TE}}{\partial x}\right|^2 - \left|\frac{\partial\psi_{TM}}{\partial x}\right|^2\right) = -\gamma^2 \int_{-\infty}^0 \Big(|\psi_{TE}|^2 - |\psi_{TM}|^2\Big)dx. \quad (5.17)$$

For the sum of the terms one, two, and three, S,

$$S = term1 + term2 + term3 \simeq -2\gamma^2 \int_{-\infty}^0 \Big(|\psi_{TE}|^2 - |\psi_{TM}|^2\Big)dx. \quad (5.18)$$

By substituting the exponential optical fields in the cladding layer, equations 5.8 and 5.9,

$$S \simeq -2\gamma^2 \int_{-\infty}^0 \Big(|\psi_{TE}|^2 - |\psi_{TM}|^2\Big)dx = -\gamma(B_1^2 - B_2^2), \quad (5.19)$$

and using the values obtained for the coefficients B_1 and B_2, equations 5.10 and 5.11,

$$S \simeq -\frac{4}{3}\frac{4}{\gamma^4 W_x^6 \pi}\left(1 - \left(\frac{n_c}{n_b}\right)^6\right). \quad (5.20)$$

Comparing S, to the calculated value for the fourth term,

$$term4 = -\int_0^\infty \left(\left|\frac{\partial\psi_{TE}}{\partial x}\right|^2 - \left|\frac{\partial\psi_{TM}}{\partial x}\right|^2\right)dx \simeq \frac{4}{\gamma W_x^3\sqrt{\pi}}\left(1 - \left(\frac{n_c}{n_b}\right)^2\right), \quad (5.21)$$

simply shows,

$$S \simeq -\frac{4}{3}\frac{1}{\sqrt{\pi}}\left(1+\left(\frac{n_c}{n_b}\right)^2+\left(\frac{n_c}{n_b}\right)^4\right)\left(\frac{1}{\gamma W_x}\right)^3 \times term4, \tag{5.22}$$

or

$$S \propto \left(\frac{1}{\gamma W_x}\right)^3 term4. \tag{5.23}$$

Therefore the first three terms on the right-hand-side of equ. 5.12 are about three orders of magnitude smaller than the fourth term for a typical waveguide of our interest (for example for a typical set of values such as: n_b = 2.22 for a lithium niobate substrate [22], n_c = 1.46 for a silicon dioxide buffer layer [56], λ_o = 1.3 μm, and $W_x \approx$ 2.5 μm, one obtains $\left(\frac{1}{\gamma W_x}\right)^3 \approx \frac{1}{8000}$) Hence,

$$2\beta\Delta\beta \approx -\int_0^\infty \left(\left|\frac{\partial\psi_{TE}}{\partial x}\right|^2-\left|\frac{\partial\psi_{TM}}{\partial x}\right|^2\right)dx, \tag{5.24}$$

and consequently,

$$\Delta\beta \approx \frac{2}{\beta\gamma W_x^3\sqrt{\pi}}\left(1-\left(\frac{n_c}{n_b}\right)^2\right). \tag{5.25}$$

§ 5.3 Results

Example I : The Slab Waveguide

Since, for a slab waveguide the exact value of $\Delta\beta$ can be calculated, this structure has been chosen to demonstrate the application of the derived expression. To verify that equation 5.25 gives a reasonable approximation to $\Delta\beta$, we have applied it to obtain $\Delta\beta$ for slab waveguides with various film refractive indices and thicknesses. The results are compared to the exact values of $\Delta\beta$ for the structures.

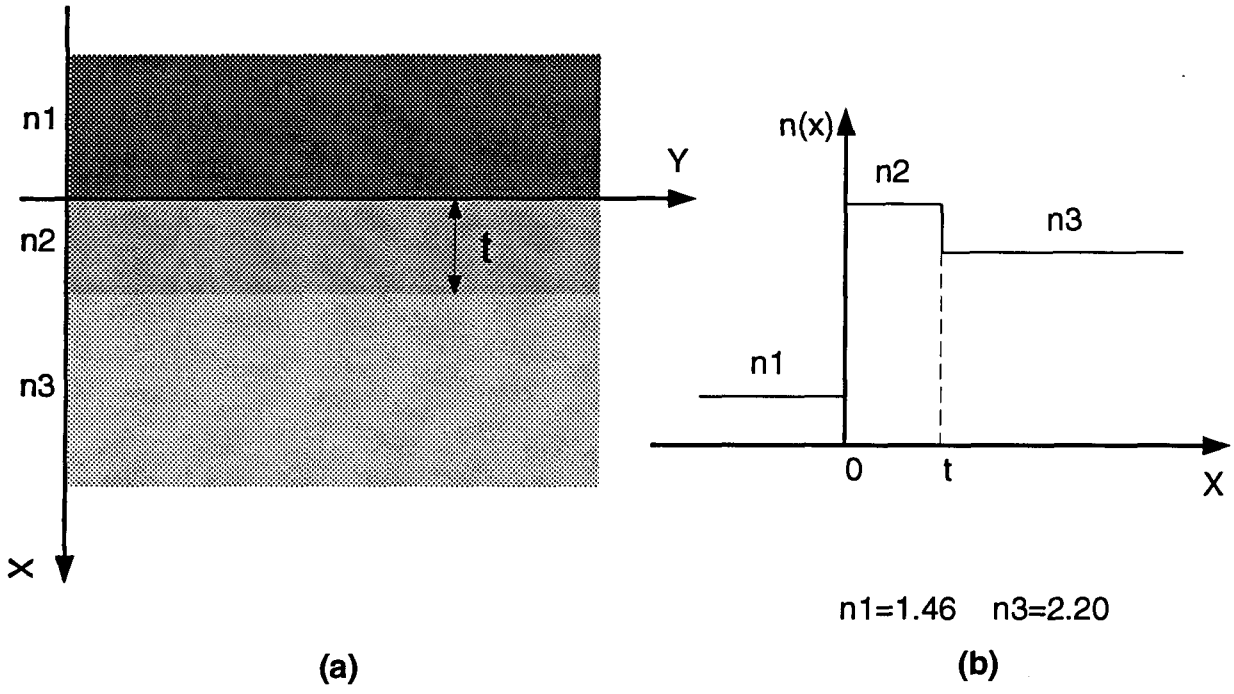

Figure 5.1. The general planar waveguide structure used in our calculations
a) the slab structure b) the corresponding refractive index profile.

Fig. 5.1 shows the refractive index profile of a typical dielectric slab waveguide. The analytical expressions for β_{TE} and β_{TM}, as well as the electric field profiles of a slab waveguide, can be found in textbooks [16,15]. The slab waveguide analyzed had a constant film thickness, t = 4.5 μm, substrate and cladding refractive indices, n_3 = 2.2, n_1 = 1.46, respectively, and film refractive indices, n_2, ranging from 2.202 to 2.210 at an optical, free-space, wavelength of λ_0 = 1.3 μm. The selected values for n_1, n_2, n_3, and t are close to the ones for a *Ti:LiNbO3* channel waveguide.

The effective refractive indices, β_{TE} and β_{TM}, for the fundamental modes supported by this structure were calculated. The solid curve in Fig. 5.2 shows the calculated values for $\Delta\beta = \beta_{TE} - \beta_{TM}$.

The width parameter, W_x, is needed in order to use equ. 5.25 to approximate $\Delta\beta$. W_x is found by fitting a Hermite-Gaussian function, *HG*, to the actual optical field distribution,

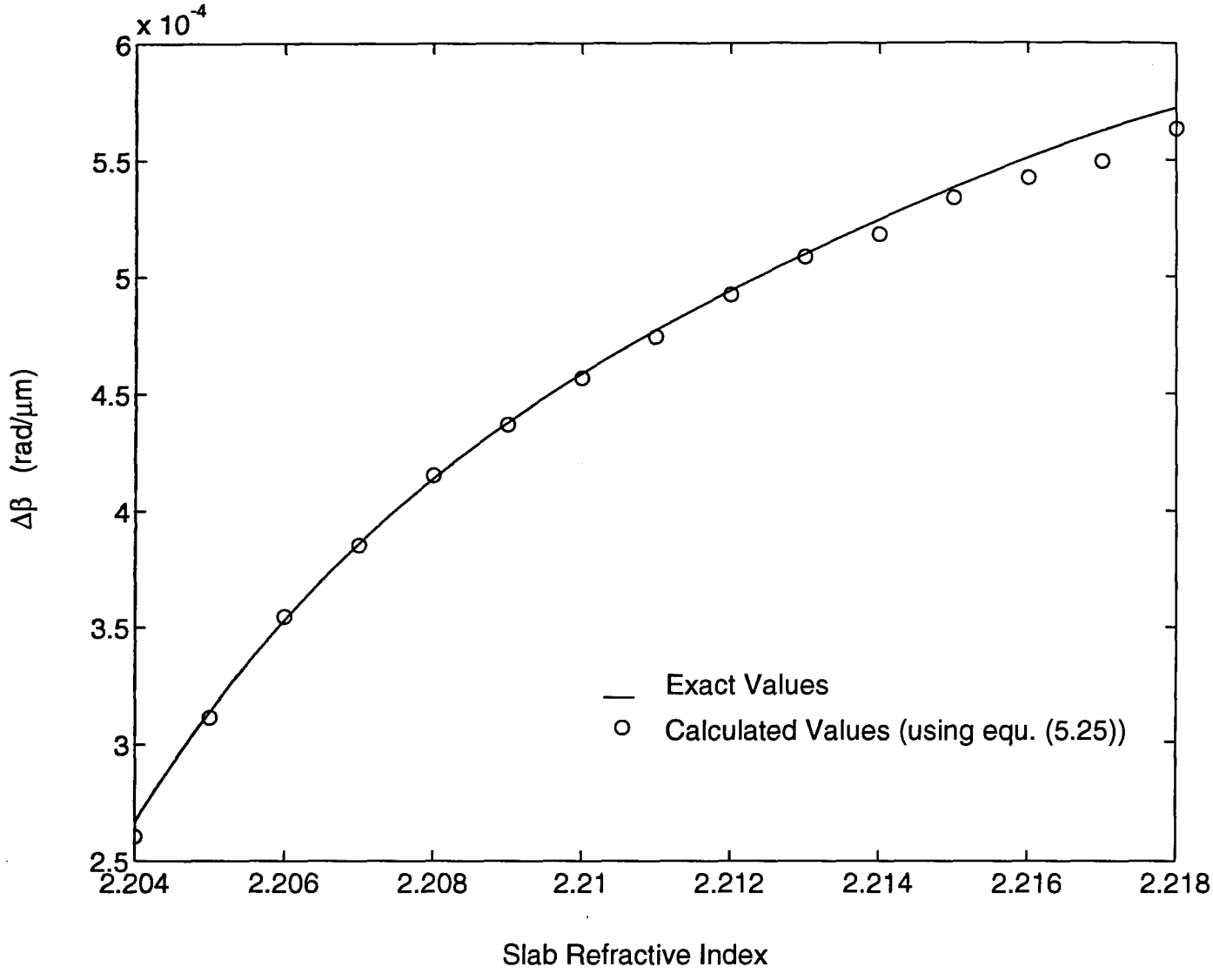

Figure 5.2. Exact and approximate values of $\Delta\beta$ for a slab waveguide for various film refractive indices, with constant film thickness, t = 4.2 μm.

ψ_{TE}, of the slab waveguides mentioned above. Equation 5.24 implies that a Hermite-Gaussian function whose derivative most closely resembles the derivative of the optical field distribution for the slab waveguide, will give best results. Therefore, a Hermite-Gaussian function that minimizes the expression

$$D(x) = \left|\frac{\partial HG}{\partial x}\right|^2 - \left|\frac{\partial \psi_{TE}}{\partial x}\right|^2, \tag{5.26}$$

was used to approximate the field profile and to find W_x.

The extracted W_x was used to calculate $\Delta\beta$. In Fig. 5.2, the open circles represent the results. These values match the exact values of $\Delta\beta$ quite well and the maximum error is 2.3%. Fig. 5.3 shows the results of similar calculations for slab waveguides with constant refractive indices in each of the regions where n_1 = 1.46, n_2 = 2.204, and n_3 = 2.20, but having different film thicknesses, t = 4–7μm.

The good agreement, both in trend and value, between the $\Delta\beta$s obtained from 5.25 and the exact values, lends strong support with regard to the merit of approximations made to derive 5.25.

Example II : Z-propagating Ti : $LiNbO_3$ Waveguides

Recently there has been a considerable interest in z-propagating guided wave devices in $LiNbO_3$ [54,57,58]. The main reasons for this emerging interest are the symmetry in refractive index for TE and TM polarizations [57,53], resistance to optical damage [59], and absence of surface waveguiding.

To demonstrate that equ. 5.25 gives a reasonable estimate of the small modal birefringence in a z-propagating $Ti : LiNbO_3$ waveguide, a number of z-propagating waveguides with different channel widths were fabricated. A 700 °A thick layer of titanium was deposited onto a y-cut $LiNbO_3$ substrate by thermal evaporation. The deposited layer was patterned to the desired configuration by plasma etching. The subsequent indiffusion of the titanium was carried out at a temperature of 1050 °C for 6.5 hours in an oxygen atmosphere. $\Delta\beta$ was measured at a wavelength of 1.3 μm through the method explained in detail in the preceding sections. Measurements were done for waveguides with different prediffusion strip widths, w, ranging from 6 to 9.5 μm. The measured $\Delta\beta$s were substituted into equ.

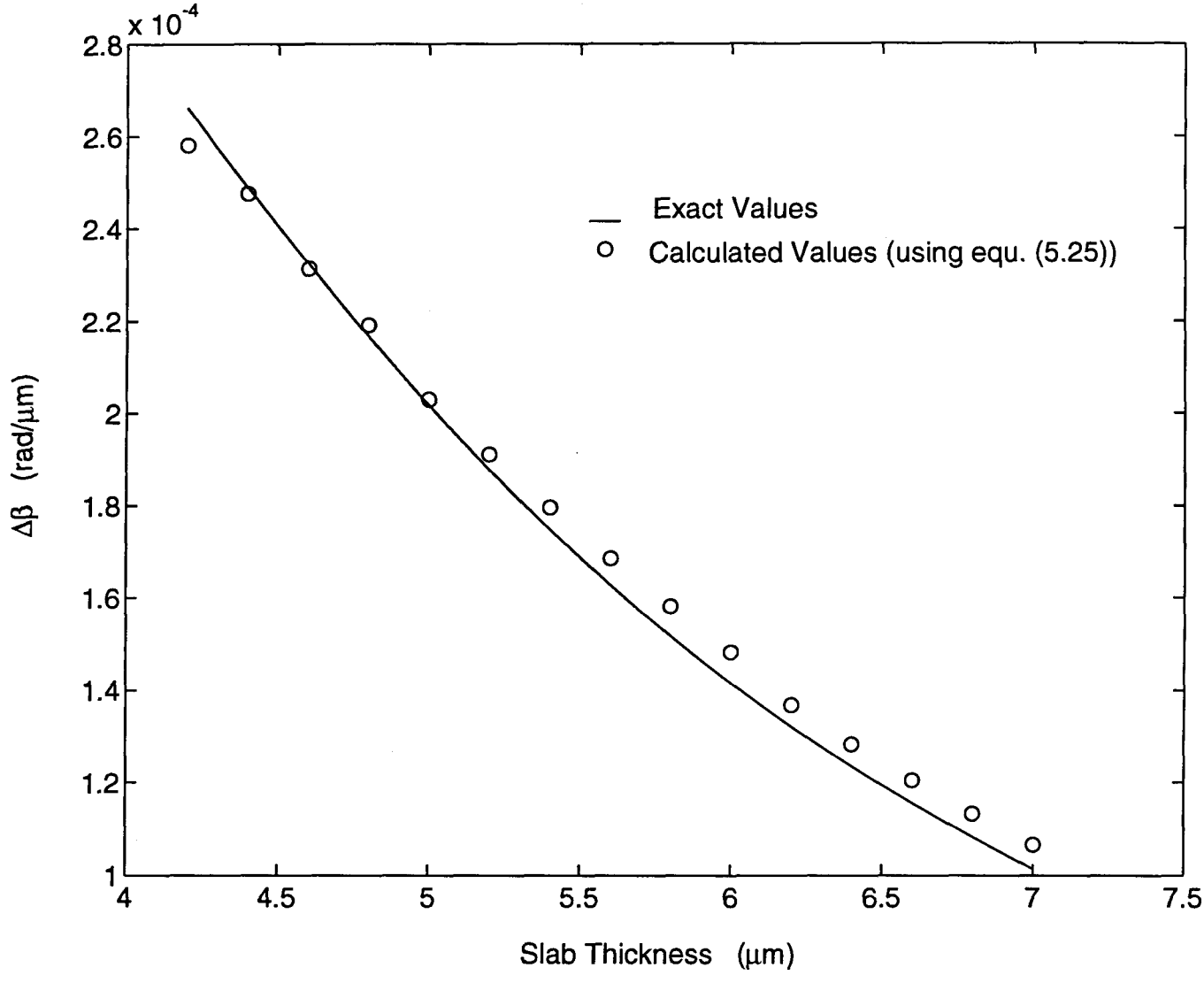

Figure 5.3. Exact and approximate values of $\Delta\beta$ for a slab waveguide for various film thicknesses with constant refractive index, n = 2.204.

5.25 and the modal depth size, W_y, was obtained for different values of, w. The open circles in Fig. 5.4 represent the results.

Also, the modal depth size, W_y, was calculated directly from the fabrication parameters using the variational method given in [26]. As was discussed previously, the commonly used expression for the diffused Ti concentration in $LiNbO_3$ is [20],

$$C(x,y) = \frac{\tau}{2\sqrt{\pi D_y t}} e^{-\frac{y^2}{4D_y t}} \left[erf\left(\frac{w/2+x}{2\sqrt{D_x t}}\right) + erf\left(\frac{w/2-x}{2\sqrt{D_x t}}\right)\right], \qquad (5.27)$$

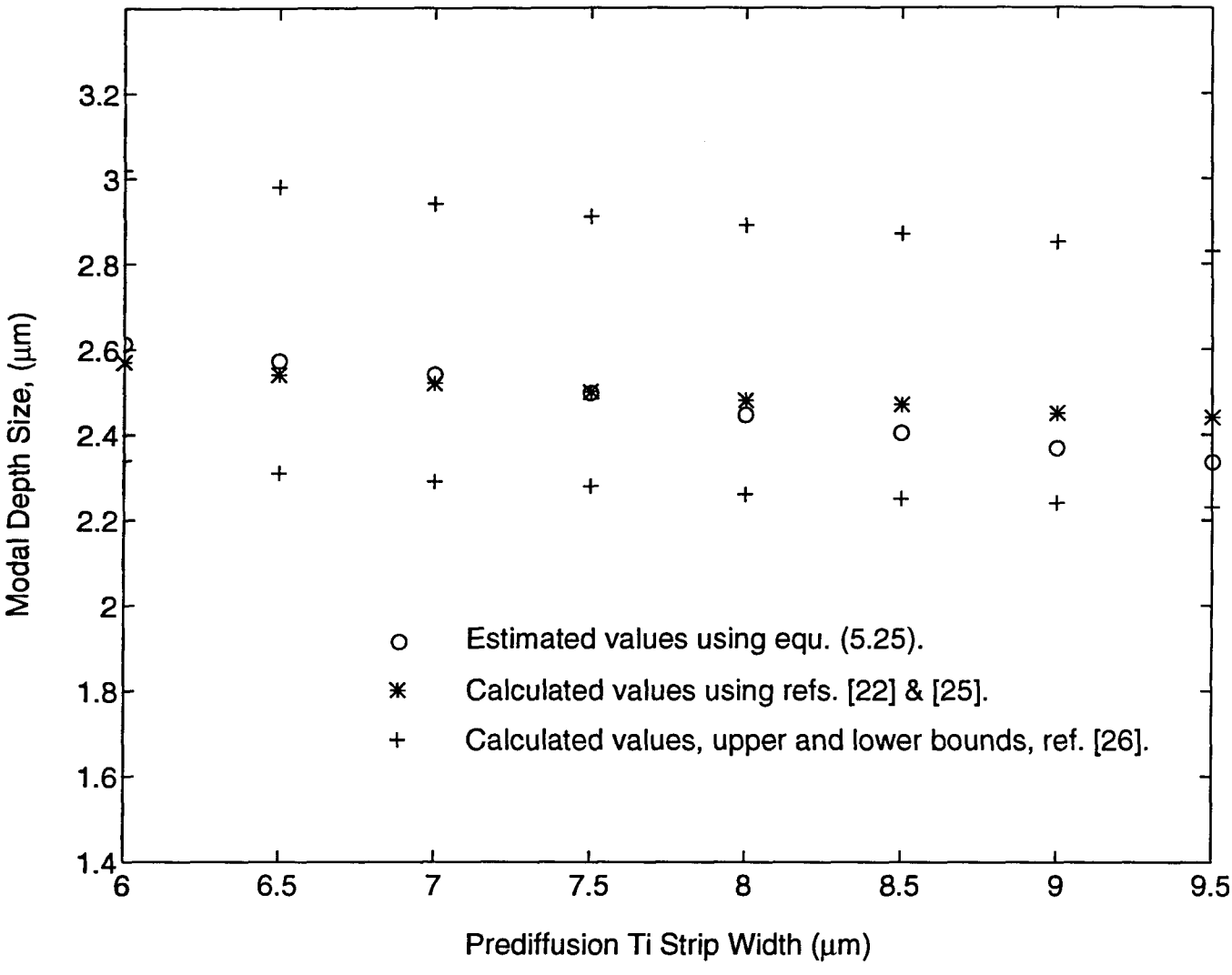

Figure 5.4. Comparison of modal depth sizes calculated by numerical simulation and using equ. 5.25, for a Ti-diffused channel waveguide.

where D_x and D_y are the diffusion constants in the x and y directions, respectively. Since the z crystallographic axis is the propagation direction, we can assume that the bulk and lateral diffusion constants are the same [27,60], i.e., in the x-y plane $D_x = D_y$.

There are several values reported for the diffusion constants [60–63] and for the dependence of the refractive-index change on the titanium concentration [23–25,64]. The diffusion

constants and index change have a significant effect on the waveguide mode profiles. Since values reported in the literature show that considerable differences are obtained by different groups, we adopted the approach of finding upper and lower bounds for mode sizes, as was done in [26]. Using ref. [26] and its proposed data sets, upper and lower bounds for W_y were calculated for different values of w. These results are shown by plus signs in Fig. 5.4. Using the values given in ref. [25] to find the index change as a function of the titanium concentration and the values given in ref. [22] for the diffusion constants, we obtain a set of values for W_y, represented by asterisks in Fig. 5.4. The fact that the values obtained from the combination of measured $\Delta\beta$s and equ. 5.25 lies between the upper and lower bounds shows that equ. 5.25 is valid for this practical structure. This validity is preserved as long as the light profile in the guiding region in the depth direction resembles a Hermite-Gaussian function. It also implies that this approach can be used as an easy, indirect method for measuring the modal depth size for this category of waveguides.

Chapter 6: Conclusions

A thorough study was made of the modeling, fabrication, and characterization of infrared Integrated Optics Pockels Cell (IOPC). Attention was particularly focussed on the following specific areas:

- Theory of operation of IOPC: derivation of normalized optical-intensity-out/electric-field-in transfer function, modeling of *Ti:LiNbO$_3$* channel waveguides, and calculation of certain characteristics like $\Delta\beta=\beta_{TE}-\beta_{TM}$; mainly aimed at increasing the predictability of the device performance (chapters 2 and 5).
- Fabrication of a completely integrated IOPC: including fabrication of *Ti:LiNbO$_3$* channel waveguides and integration of a fully connectorized IOPC; with a look at the reproducibility of the fabrication process for possible industrial production (chapter 3).
- Device characterization: measurement of certain characteristics of the fabricated device under various conditions and application of necessary modifications in order to meet industrial requirements and standards (chapter 4).

The theory of operation of the IOPC was studied and a practical normalized optical-intensity-out/electric-field-in transfer function was derived. The *Ti:LiNbO$_3$* channel waveguide was modeled and certain characteristics such as the optical field distribution, the propagation constants, and optical mode sizes were calculated. Two different computational methods, namely, the effective index method (EIM) and the finite difference method (FDM), were implemented and the results were compared to the ones obtained from variational method (VM). The above comparison showed that for weakly guiding structures, like *Ti:LiNbO$_3$*

channel waveguides where the maximum index change in guiding region was less than 0.01, EIM needed a high-resolution grid to produce comparably accurate results and consequently needed a considerable amount of time on the order of a few hours, while the same task was carried out by FDM on a simpler grid in a few minutes. The main purpose of the modeling section was to build up a link between fabrication parameters and the optical characteristics of the devices produced.

The concept of bias was introduced in chapter 2 ($\phi_i = L\times\Delta\beta = L\times(\beta_{TE}-\beta_{TM})$) and in chapter 5 a variational method was used to derive an approximate analytical expression for $\Delta\beta$. Applying this expression to slab structures for which exact analytical solutions were possible, a check on our approximations could be made. Excellent agreement was found (figures 5.2 and 5.3). This suggests that equation 5.25 can be used to accurately estimate$\Delta\beta$'s for z-propagating *Ti:LiNbO$_3$* channel waveguides.

In brief, chapters 2 and 5 were dedicated to developing the theory and to modeling the devices to the degree necessary to predict the device performance and characteristics from physical specifications and fabrication parameters.

Fabrication of IOPCs consisted of fabricating the sensor-head and performing the system integration. For the fabrication of *Ti:LiNbO$_3$* channel waveguides, reported values in literature were used as the initial guess, then the appropriateness of these values was verified using our numerical models. The fabrication process was carried out in the solid state laboratory, and then fabricated devices were tested in the laser laboratory. After choosing an appropriate waveguide in terms of bias , on/off ratio, and optical throughput, a fully connectorized infrared IOPC was successfully constructed.

The fabricated IOPCs were tested under various conditions. It was shown that the

normalization process, explained theoretically in chapter 2, is capable of cancelling very large optical power fluctuations (1000:1). The assumption of linear dependence of bias on the device length was tested and verified; also, $\Delta\beta$ and $L_{2\pi}$ were experimentally measured.

It was shown that the device performance is linear and accurate enough to measure the applied AC electric field with less than 0.3% error and, therefore, these devices are able to meet Erickson's standards [49] for high-voltage metering.

The sensor's thermal stability was tested over the temperature range 20 – 70°C. Since the observed thermal drift of bias for z-propagating *Ti:LiNbO$_3$* channel waveguides was less than 0.2°/°C the error introduced was insignificant and could be accounted for by post-processing.

It was shown that the limiting effect of piezoelectric resonance frequencies on the device bandwidth can be evaded since the resonance frequencies can be pushed to higher and higher frequencies by making the device narrower and thinner. Also, the device indicated that it would easily be capable of following the fastest rising edge (t_f = 1.2 μs) suggested by the IEC for impulse measurements.

As a suggestion for future work a real-time post-processing unit is recommended. As mentioned previously, such a unit brings several enhancements to the device performance: implementation of a digital, narrow bandpass filter allows the reduction of noise effects on the device accuracy; implementation of digital notch filters at piezoelectric resonance frequencies allows broadening of the device bandwidth; the working range of the device can be extended to nonlinear regions thereby increasing the device dynamic range; and also, through a calibration process, the temperature dependence of V_π can be measured and stored in the computer memory, and duly accounted for.

Finally, the results of our studies and experiments show that: the IOPC has a well-

predictable performance; its fabrication process is reproducible in larger scales; and it is capable of meeting the suggested standards of AC voltage metering and impulse measurement. Therefore, in terms of both performance and cost, the IOPC may be considered as a plausible alternative to the conventional potential transformers currently used in the power industry.

Appendix A: Justification of the Scalar Approximation

Until now, in our calculations, we have used the scalar wave equation, 2.22, in place of the vector wave equations, 2.20 and 2.21. We have been assuming that the terms involving the derivatives of refractive index profile were negligible. To test the validity of this approximation, we have calculated the contributions of the extra terms in the vector wave equations, to β^2 and $\Delta\beta$, using the variational method [65].

In the variational approach, through a prior knowledge of the optical field distributions, one tries to maximize the integral expression (or as it is called in some references "the variational expression") for β^2 by optimizing the parameters of the trial function. The commonly used trial function for Ti:$LiNbO_3$ channel waveguides is [48,66]

$$E(x,y) = \begin{cases} A\left(\frac{y}{W_y}\right) exp\left[-\frac{1}{2}\left(\frac{x^2}{W_x^2} + \frac{y^2}{W_y^2}\right)\right] & y \geq 0 \\ 0 & y < 0. \end{cases} \tag{A.1}$$

For the above trial function the variational expressions for the β_{TE}^2 and β_{TM}^2 derived from equs. 2.20 and 2.21, respectively, reduces to [66]

$$\beta_{TE,TM}^2 = \beta^2 + d_{TE,TM} \tag{A.2}$$

where β^2 is the scalar variational expression,

$$\beta^2 = -\frac{0.5}{W_x^2} - \frac{1.5}{W_y^2} + \frac{k_o \int_0^\infty \int_{-\infty}^\infty n^2(x,y) \frac{y^2}{W_y^2} exp\left[-\left(\frac{x^2}{W_x^2} - \frac{y^2}{W_y^2}\right)\right] dxdy}{(\pi/4) W_x W_y}, \tag{A.3}$$

and,

$$d_{TE} = \frac{k_o \int_0^\infty \int_{-\infty}^\infty F(x,y) \frac{y^2}{W_y^2} exp\left[-\left(\frac{x^2}{W_x^2} - \frac{y^2}{W_y^2}\right)\right] dxdy}{(\pi/4) W_x W_y}, \tag{A.4}$$

Table A.1 Calculated values of d_{TE} and d_{TM} for various waveguide prediffusion widths.

Waveguide Width (μm)	β^2 (rad^2/μm^2)	d_{TE} (rad^2/μm^2)	d_{TM} (rad^2/μm^2)	$\lvert d_{TE} - d_{TM} \rvert / 2\beta$ (rad/μm)
6	1.1326e+2	-7.33e-5	-8.05e-6	3.07e-6
7	1.1329e+2	-7.14e-5	-1.81e-5	2.50e-6
8	1.1332e+2	-6.64e-5	-2.48e-5	1.95e-6
9	1.1334e+2	-5.99e-5	-2.98e-5	1.41e-6

where

$$F(x,y) = \frac{\partial^2 ln\, n^2(x,y)}{\partial x^2} - \frac{x}{W_x^2}\frac{\partial ln\, n^2(x,y)}{\partial x},$$

and

$$d_{TM} = \frac{k_o \int_0^{\infty}\int_{-\infty}^{\infty} \left\{ G_1(x,y)\frac{y^2}{W_y^2} exp\left[-\left(\frac{x^2}{W_x^2} - \frac{y^2}{W_y^2}\right)\right] + G_2(x,y) exp\left[-\left(\frac{x^2}{W_x^2} - \frac{y^2}{W_y^2}\right)\right]\right\} dxdy}{(\pi/4) W_x W_y}, \tag{A.5}$$

where

$$G_1(x,y) = \frac{\partial^2 ln\, n^2(x,y)}{\partial y} - \frac{y}{W_y^2}\frac{\partial ln\, n^2(x,y)}{\partial y},$$

and

$$G_2(x,y) = \frac{y}{W_y^2}\frac{\partial ln\, n^2(x,y)}{\partial y}.$$

At first, through using the program written by Mr. Benny Tsou, see reference [26], the parameters of the trial function A.1, i.e., W_x and W_y, were determined by maximizing the scalar variational expression A.3. As the second order effects, the values obtained for W_x and W_y were used to calculate d_{TE} and d_{TM}. Table A.1 shows the calculated values of d_{TE} and d_{TM} for various waveguides having different prediffusion widths ranging from 6 μm to 9 μm, fabricated under the same conditions as those given in section 2.3. The results listed in table A.1 show that the values of d_{TE} and d_{TM} are not only negligible compared to β^2, their contributions to $\Delta\beta$, i.e., $\frac{|d_{TE}-d_{TM}|}{2\beta}$, are also on the order of 10^{-2} smaller than typical

values of $\Delta\beta$. Hence, approximating the vector wave equations 2.20 and 2.21 by the scalar one would not produce a notable error in the calculated values of either β^2 or $\Delta\beta$.

Refrences

[1] I. P. Kaminow, *An Introduction to Electrooptic Devices*. New York: Academic Press, 1974.

[2] T. H. Maiman, "Optical and microwave-optical experiments in ruby," *Phys. Rev. Lett.*, vol. 4, p. 564, 1960.

[3] A. J. Rogers, "Optical technique for measurement of current at high voltage," *Proc. IEE*, vol. 120, pp. 261–267, 1973.

[4] M. Waters and E. L. White, "Current measurement in high voltage conductors," *ERA report QT162*, 1962.

[5] S. Saito, J. Hamosaki, Y. Fujii, K. Yokoyama, and Y. Ohno, "Development of the laser current transformer for extra-high-voltage power transmission lines," *IEEE J. Quantum Electron.*, vol. QE-3, pp.589–597, 1967.

[6] T. Sawa, K. Kurosawa, T. Kaminishi, and T. Yokota, "Development of optical instrument transformers," *IEEE Trans. Power Delivery*, vol. 5, pp. 884–891, 1990.

[7] T. Mitsui, K. Hosoe, H. Usami, and S. Miyamoto, "Development of fiber-optic voltage sensors and magnetic-field sensor," *IEEE Trans. Power Delivery*, vol. 2, pp. 87–93, 1987.

[8] Y. Kuroda, Y. Abe, H. Kuwahara, and K. Yoshinaga, "Field test of fiber-optics voltage and current sensors," *SPIE, Fiber Optic Sensors*, vol. 586, p. 30, 1985.

[9] M. Kanoi, G. Takahashi, T. Sato, M. Higaki, E. Mori, and K. Okumura, "Optical voltage and current measuring system for electric power systems," *IEEE Trans. Power Delivery*, vol. pwrd-1, pp. 91–97, 1986.

[10]G. A. Massey, D. C. Erickson, and R. A. Kaldec, "Electromagnetic field components: their measurement using linear electro-optic and magneto-optic effects," *Appl. Opt.*, vol. 14, pp. 2712–2719, 1975.

[11]A. J. Rogers, "Method for simultaneous measurement of current and voltage on high-voltage lines using optical techniques," *Proc. IEE*, vol. 123, pp. 957–960, 1976.

[12]S. Kobayashi, A. Horide, I. Takagi, M. Higaki, G. Takahashi, E. Mori, and T. Yamagiwa, "Development and field test evaluation of optical current and voltage transformers for gas insulated switchgear," *IEEE Trans. Power Delivery*, vol. 7, pp. 815–821, 1992.

[13]N. A. F. Jaeger, "Integrated optics pockels cell voltage sensor," *U.S. Patent # 5,029,273*, July 2, 1991.

[14]A. Yariv, *Optical Electronics*. New York: Holt, Rinehart, and Winston, Inc., 1991.

[15]S. Ramo, J. R. Whinnery, and T. V. Duzer, *Fields and Waves in Communication Electronics*. New York: Wiley, 1984.

[16]A. Yariv and P. Yeh, *Optical Waves in Crystals*. New York: Wiley, 1984.

[17]R. C. Alferness, V. R. Ramaswamy, S. K. Korotky, M. D. Divino, and L. L. Buhl, "Efficient single-mode-fiber to titanium diffused lithium niobate waveguide coupling for λ=1.32," *IEEE J. Quantum Electron.*, vol. QE-18, pp. 1807–1813, 1982.

[18]T. Tamir, *Guided-wave Optoelectronics*. Berlin: Springer-Verlag, 1990.

[19]J. Crank, *The Mathematics of diffusion*. New York: Oxford University Press, 1975.

[20]M. D. Feit, J. A. Fleck, and L. McCaughan, "Comparison of calculated and measured performance of diffused channel waveguide couplers," *J. Opt. Soc. Am.*, vol. 73, pp. 1296–1304, 1983.

[21]M. Fukuma, J. Noda, and H. Iwasaki, "Optical properties in titanium diffused $LiNbO_3$ strip waveguides," *J. Appl. Phys.*, vol. 49, pp. 3693–3698, 1978.

[22]*Properties of Lithium Niobate. EMIS Datareviews Series No. 5.*

[23]M. Minakata, S. Saito, M. Shibata, and S. Miyazawa, "Precise determination of refractive-index change in titanium-diffused $LiNbO_3$ optical waveguides," *J. Appl. Phys.*, vol. 49, pp. 4677–4682, 1978.

[24]J. Ctyroky, M. Hofman, J. Janata, and J. Schrofel, "3–d analysis of $LiNbO_3$:Ti channel waveguides and directional couplers," *IEEE J. Quantum Electron.*, vol. QE-20, pp. 400–409, 1984.

[25]K. Koai and P. Liu, "Modeling of Ti:$LiNbO_3$ waveguide devices: Part i —directional couplers," *J. Lightwave Technol.*, vol. LT-7, pp. 533–539, 1989.

[26]N. Jaeger and B. Tsou, "Calculation of the fundamental mode sizes in optical waveguides using gaussian quadrature," *IEEE Trans. on Microwave Theory Tech.*, vol. MTT-41, pp. 1907–1912, 1993.

[27]E. Wooten and W. Chang, "Test structures for characterization of electrooptic waveguide modulators in lithium niobate," *IEEE J. Quantum Electron.*, vol. QE–29, pp. 161–170, 1993.

[28]A. Snyder and J. D. Love, *Optical Waveguide Theory*. New York: Chapman and Hall, 1983.

[29]C. M. Kim and R. V. Ramaswamy, "Modelling of graded-index channel waveguides using nonuniform finite difference method," *J. Lightwave Technol.*, vol. 7, pp. 1581–1589, 1989.

[30]J. H. Marsh and R. M. D. L. Rue, *Waveguide Optoelectronics*. The Netherlands: Kluwer Academic Publishers, 1992.

[31]W. Streifer and E. Karpon, "Application of the equivalent-index method to DH diode lasers," *Appl. Opt.*, vol. 18, pp. 3724–3725, 1979.

[32]L. G. Fereira and M. A. A. Pudensi, "Waveguiding in a dielectric medium varying slowly in one transverse direction," *J. Opt. Soc. Amer.*, vol. 71, pp. 1377–1380, 1981.

[33]K. S. Chang, "Dual effective-index method for the analysis of rectangular dielectric waveguides," *Appl. Opt.*, vol. 25, pp. 2169–2174, 1986.

[34]L. M. Walpita, "Calculation of approximate propagation characteristics of any given two-dimensional optical waveguide," *Electron. Lett.*, vol. 21, pp. 1075–1076, 1985.

[35]K. S. Chang, "Analysis of optical fibers by the effective-index method," *Appl. opt.*, vol. 25, pp. 348–354, 1986.

[36]S. V. Burke, "Spectral index method applied to rib and strip-loaded directional couplers," *IEE Proceedings, Pt J*, vol. 137, pp. 7–10, 1990.

[37]S. M. Stern, P. C. Kendall, and P. McIlroy, "Analysis of the spectral index method for vector modes of rib waveguides," *IEE Proceedings, Pt J*, vol. 137, pp.21–26, 1990.

[38]D. Lee, *Electromagnetic principles of integrated optics*. New York: Wiley, 1986.

[39]F. Elewaut, *Wave propagation in monomode optical fibers and integrated optical structures*. PhD thesis, Laboratory of Electromagnetism and Acoustics, University of Gent, 1987.

[40]K. Nassau, H. J. Levinstein, and G. M. Loiacono, "Ferroelectric lithium niobate 1: growth, domain structure, dislocation, and etching," *J. Chem. Phys. Solids*, vol. 27, 983–988, 1966.

[41]K. Nassau, H. J. Levinstein, and G. M. Loiacono, "Ferroelectric lithium niobate 2: preparation of single domain crystal," *J. Chem. Phys. Solids*, vol. 27, 989–996, 1966.

[42]S. C. Abrahams, J. M. Reddy, and J. L. Bernstein, "Ferroelectric lithium niobate 3: single crystal x-ray diffraction study at 24°C," *J. Chem. Phys. Solids*, vol. 27, 997–1012, 1966.

[43]S. C. Abrahams, W. C. Hamilton, and J. M. Reddy, "Ferroelectric lithium niobate 4: single crystal neutron diffraction study at 24°C," *J. Chem. Phys. Solids*, vol. 27, 1013–1018, 1966.

[44]S. C. Abrahams, W. C. Hamilton, and J. L. Bernstein, "Ferroelectric lithium niobate 5: polycrystal x-ray diffraction study at 24°C and 24°C," *J. Chem. Phys. Solids*, vol. 27, 1019-1026, 1966.

[45]I. P. Kaminow and J. R. Carruthers, "Optical waveguide layers in $LiNbO_3$ $LiTaO_3$," *Appl. Phys. Lett.*, vol. 22, p. 326, 1973.

[46]J. L. Jackel, "Proton exchanged for high-index waveguide in $LiNbO_3$," *Appl. Phys. Lett.*, vol. 41, p. 607, 1982.

[47]R. V. Schmidt and I. P. Kaminow, "Metal-diffused optical waveguides in $LiNbO_3$," *Appl. Phys. Lett.*, vol. 25, pp. 458–460, 1974.

[48]S. K. Korotky, W. J. Minford, L. L. Buhl, M. D. Divino, and R. C. Alferness, "Mode size and method for estimating the propagation constant of single-mode Ti:$LiNbO_3$ strip waveguides," *IEEE J. of Quantum Electron.*, Oct. 1982.

[49]D. C. Erickson, "A primer on optical current and voltage sensors and an update on activity," Engineering Symposium, Bonneville Power Administration, Mar. 31–Apr. 1, 1992.

[50]V. Gercke, P. Hertel, E. Kratzig, J. P. Nisius, and R. Sommerfeld, "Light-induced refractive index changes in $LiNbO_3$:Ti waveguides," *Appl. Phys. B*, vol. 44, pp. 155–162,1987.

[51]A. Neyer, "Integrated-optic devices in lithium niobate: technology and applications," *SPIE, Electro-Optic and Magneto-Optic Materials II*, vol. 1274, pp. 2–17, 1990.

[52]F. C. Creed and M. M. C. Collins, "Shaping circuits for high voltage impulses," *IEEE Winter Power Meeting, NY*, pp. 2239–2242, Jan. 31–Feb. 5, 1971.

[53]T. Kawazoe, K. Satoh, I. Hayashi, and H. Mori, "Fabrication of integrated-optic polarization controller using z-propagating Ti-$LiNbO_3$ waveguides," *J. Lightwave Technol.*, vol. LT-10, pp. 51–56, 1992.

[54]N. A. Sanford, J. M. Connors, and W. A. Dyes, "Simplified z-propagating dc bias stable TE-TM mode converter fabricated in a y-cut lithium niobate," *J. Lightwave Technol.*, vol. 6, pp. 898–902, 1988.

[55]R. Keil and F. Auracher, "Coupling of single-mode Ti-diffused $LiNbO_3$ waveguides to single-mode fibers," *Optics Communications*, July 1979.

[56]M. Masuda and J. Koyama, "Effects of a buffer layer on TM modes in a metal-clad optical waveguide using Ti-diffused $LiNbO_3$ C-plate," *Appl. Opt.*, vol. 16, pp. 2994–3000, 1977.

[57]S. Thaniyavarn, "Wavelength independent, optical-damage-immune $LiNbO_3$ TE-TM mode converter," *Opt. lett., vol. 11, pp. 39–41*, 1986.

[58]M. Haruna, J. Shimada, and H. Nishihara, "Optical wavelength-independent and damage-free polarization controller in $LiNbO_3$ waveguides," *Tech. Dig. OEC'86*, 1986, A2–4.

[59]R. Holman, J. Busch, and C. Verber, "Z-axis propagation and the avoidance of optical damage in lithium niobate waveguides," *in Tech. Dig. IGWO'84*, 1984, WC2–01.

[60]R. Holmes and D. Smyth, "Titanium diffusion into $LiNbO_3$ as a function of stoichiometry," *J. Appl. Phys.*, vol. 55, pp. 3531–3535, 1984.

[61]K. Sugii, M. Fukuma, and H. Iwasaki, "A study on titanium diffusion into $LiNbO_3$ waveguides by electron probe analysis and x-ray diffraction methods," *J. Materials Sci.*, vol. 13, pp. 523–533, 1978.

[62]M. Fukuma and J. Noda, "Optical properties of titanium-diffused $LiNbO_3$ strip waveguides and their coupling-to-a-fiber characteristics," *Appl. Opt.*, vol. 19, pp. 591–597, 1980.

[63]S. Fouchet, A. Carenco, C. Daguet, R. Guglielmi, and L. Riviere, "Wavelength dispersion of titanium induced refractive index change in $LiNbO_3$ as a function of diffusion parameters," *J. Lightwave Technol.*, vol. LT-5, pp. 700– 708, 1987.

[64]K. Ziling, L. Pokrovskiy, V. Shashkin, and D. Shipilova, "The relation between refractive indexes and kinetics of titanium diffusion in planar $LiNbO_3$ waveguides," *Avtometriya*, pp. 103–108, 1978 (in Russian).

[65]M. J. Adams, *An introduction to optical waveguides*. New York: Wiley, 1981.

[66]N. Jaeger and L. Young, "Voltage-induced optical waveguide modulator in lithium niobate," *IEEE J. Quantum Electron.*, vol. QE-25, pp. 720–728, 1989.